creative commons

Namensnennung-Keine kommerzielle Nutzung-Keine Bearbeitung 2.5 Schweiz

Sie dürfen:

das Werk vervielfältigen, verbreiten und öffentlich zugänglich machen

Zu den folgenden Bedingungen:

Namensnennung. Sie müssen den Namen des Autors/Rechteinhabers in der von ihm festgelegten Weise nennen (wodurch aber nicht der Eindruck entstehen darf, Sie oder die Nutzung des Werkes durch Sie würden entlohnt).

Keine kommerzielle Nutzung. Dieses Werk darf nicht für kommerzielle Zwecke verwendet werden.

Keine Bearbeitung. Dieses Werk darf nicht bearbeitet oder in anderer Weise verändert werden.

- Im Falle einer Verbreitung müssen Sie anderen die Lizenzbedingungen, unter welche dieses Werk fällt, mitteilen. Am Einfachsten ist es, einen Link auf diese Seite einzubinden.

- Jede der vorgenannten Bedingungen kann aufgehoben werden, sofern Sie die Einwilligung des Rechteinhabers dazu erhalten.

- Diese Lizenz lässt die Urheberpersönlichkeitsrechte unberührt.

Quelle: http://creativecommons.org/licenses/by-nc-nd/2.5/ch/   Datum: 3.4.2009

Carbon Nanotube Spin-Valve with Optimized Ferromagnetic Contacts

Inauguraldissertation

zur
Erlangung der Würde eines Doktors der Philosophie
vorgelegt der
Philosophisch-Naturwissenschaftlichen Fakultät
der Universität Basel

von

Hagen Matthias Aurich
aus Deutschland

UNI
BASEL

Basel, 2012

Genehmigt von der Philosophisch-Naturwissenschaftlichen Fakultät
auf Antrag von
Prof. Dr. C. Schönenberger
Prof. Dr. B. Hickey
Dr. A. Baumgartner

Basel, 18. Oktober 2011

<div align="right">

Prof. Dr. Martin Spiess
Dekan

</div>

Contents

Introduction

Technological progress leads to a continuous miniaturization of electronic components, permanently on the search for alternatives to increase the information density of storage devices, to make electronic devices faster and to reduce dissipation in electronic circuits [1]. Unlike conventional electronic devices, based on charge transport, spin electronic or spintronic devices also use the electron spin degree of freedom to control electron transport [2, 3]. This offers interesting possibilities of new types of electronic devices[1] as e.g. the spin-valve, a hybride structure of ferromagnetic and non-magnetic materials.

In 1988 Peter Grünberg [5] and Albert Fert [6] discovered independently that the electrical resistance of a ferromagnetic metal - normal metal multi layer structure strongly depends on the magnetic configuration of the different layers controlled by an external magnetic field. This discovery was the basis for huge progress in computer hard disk technology [7] and both authors received the Nobel prize in physics in 2007 [8]. Later it was found that replacing the metallic interlayer by a non-magnetic insulator can further increase this magnetoresistance effect due to spin conserving tunnelling of the electrons as proposed by Jullière [9].

However, spin-valves are not only interesting in the computer industry but also offer new possibilities in basic nanoscience research. A spin polarized current can be injected from a ferromagnetic material into a nanoscale structure allowing the investigation of spin transport and spin dynamics in a solid state environment [10] and offers an additional degree of freedom for transport spectroscopy [11].

In this thesis we investigate spin-transport in carbon nanotube (CNT) spin-valve devices. CNTs can be imagined as a small sheet of hexagonal arranged carbon atoms, called graphene, rolled up into a seamless cylinder

---

[1]Spintronics is a wide research field, also including the fields of spin-based quantum computation and communication [4]. In this thesis we focus on magnetoresistance devices.

with typical diameters of a few nanometers [12]. They were discovered by S. Iijima in 1991 [13] and are the subject of theoretical and experimental studies ever since [14, 15]. CNTs are interesting for spin-transport because the spin-dephasing during transport is low due to the absence of nuclear spin in the main carbon isotope ^{12}C and the weak spin-orbit interaction [12]. In addition, CNTs allow to fabricate quantum dots coupled to ferromagnetic leads. Charging interaction effects on the magnetoresistance can be very important in transport measurements [16] and it can even be possible to combine spintronics with single electron electronics [17]. Early experiments with CNT devices already showed that spin-dependent transport is possible [18], before Sahoo *et al.* reported on the first CNT sample with 'electric field control of spin transport' [19].

Fabricating spin transport devices with CNTs is still problematic and the yield of good devices is low. On the one hand, the ferromagnetic material used for contacting should provide reliable magnetic properties. On the other hand, the electrical contact properties to CNTs should be good and reproducible. Therefore, a main goal of this thesis is to find a ferromagnetic material that fulfils those requirements and to study spin transport in CNT devices with ferromagnetic contacts.

The thesis is structured as follows:

- *Chapter 1*
  The theoretical background for this thesis including ferromagnetism, magnetoresistance devices and carbon nanotube quantum dots is provided.

- *Chapter 2*
  We present the sample fabrication methods including carbon nanotube growth, lithographic structuring and metal deposition and give a short overview of the experimental set-ups.

- *Chapter 3*
  Different ferromagnetic materials are investigated for their suitability as contact materials for carbon nanotubes.

- *Chapter 4*
  A Permalloy-based carbon nanotube device is studied and local and non-local magnetoresistance signals are presented.

- *Chapter 5*
  We summarize the results of this thesis and give an outlook to further experiments.

Chapter 1

Theoretical Background

This chapter provides a description of the basic building blocks of a carbon nanotube spin-valve. For the ferromagnetic contacts an introduction in ferromagnetism is provided, before we describe magnetic anisotropies and discuss the formation of domains in ferromagnetic materials. In the magnetoresistance section, spin transport effects are introduced and several devices making use of magnetoresistance effects are presented. The last part of the chapter deals with the electronic structure of carbon nanotubes and the formation of quantum dots at low temperatures.

1.1 Ferromagnetism

In a solid, the collective ordering of the electron spins can give rise to permanent magnetism. A *ferromagnet* (FM) shows a specific ordering where all the magnetic moments are aligned in parallel. This phenomenon is caused by the exchange interaction between different magnetic moments. The exchange interaction is a consequence of the Coulomb interaction between electrons and the symmetrization postulate (Pauli principle) as shown below.

1.1.1 Exchange interaction

To give a qualitative explanation of the *exchange interaction*, we first consider the simple two-electron system of the H_2 molecule. The coordinates of the two electrons and the two nuclei are $\boldsymbol{r}_i$ and $\boldsymbol{R}_i$ with $i = 1, 2$, respectively, as illustrated in fig. 1.1. The Hamiltonian of the system can be written as the sum of two central field Hamiltonians $\mathcal{H}^1_{atom}$ and $\mathcal{H}^2_{atom}$ describing the
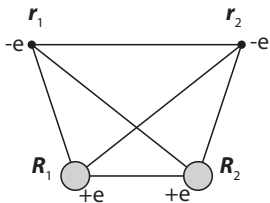
Figure 1.1: Schematic representation of the assumed two-electron system. The electrons and the nuclei have the coordinates r_i and R_i with $i = 1, 2$, respectively.

interaction of electron 1 (2) with nucleus 1 (2) and an interaction Hamiltonian $\mathcal{H}'$ including the interactions of the electrons with the other nucleus, nucleus-nucleus interaction and electron-electron interaction [20]

$$\mathcal{H}(r_1, r_2) = \mathcal{H}_{atom}^1 + \mathcal{H}_{atom}^2 + \mathcal{H}'. \tag{1.1}$$

For two undistinguishable electrons the spatial wavefunctions ϕ can be written in terms of a symmetrized and an antisymmetrized product state under particle exchange. Due to the fermion character of the electrons, the Pauli principle requires that the total wave function (including the spin part) must be antisymmetric. By first neglecting the electron-electron interaction term in $\mathcal{H}'$, in the so-called *Heitler-London approximation*, the total wave functions are found[1]

$$\psi^S = \frac{1}{\sqrt{2(1+O)}} \left[\phi_1(r_1)\phi_2(r_2) + \phi_1(r_2)\phi_2(r_1) \right] \cdot \chi_S$$

$$\psi^T = \frac{1}{\sqrt{2(1-O)}} \left[\phi_1(r_1)\phi_2(r_2) - \phi_1(r_2)\phi_2(r_1) \right] \cdot \chi_T \tag{1.2}$$

In the first equation the spatial part of the wavefunction is symmetric and the spin part of the wavefunction χ is in an antisymmetric singlet state (S). In the second equation the spatial wavefunction is antisymmetric and the spin part is in a symmetric tripet state (T).

$$\frac{1}{\sqrt{2}}(|\uparrow\downarrow\rangle - |\downarrow\uparrow\rangle) \quad \text{singlet state } \chi_S$$

$$\begin{array}{l} |\uparrow\uparrow\rangle \\ \frac{1}{\sqrt{2}}(|\uparrow\downarrow\rangle + |\downarrow\uparrow\rangle) \\ |\downarrow\downarrow\rangle \end{array} \quad \text{triplet state } \chi_T$$

$O = \langle \phi_1(r_1)\phi_2(r_2) | \phi_1(r_2)\phi_2(r_1) \rangle$ describes the double overlap integral of the two individual wave functions. The total energies in the singlet and the

---

[1] In this independent electron approximation the ionic terms of the wave function are omitted [20].

triplet states are

$$E^S = \frac{\langle \psi^S | \mathcal{H} | \psi^S \rangle}{\langle \psi^S | \psi^S \rangle} = 2E_0 + \frac{C + X}{1 + O} \qquad (1.3)$$

and

$$E^T = \frac{\langle \psi^T | \mathcal{H} | \psi^T \rangle}{\langle \psi^T | \psi^T \rangle} = 2E_0 + \frac{C - X}{1 - O} \qquad (1.4)$$

with $E_0 = \langle \phi_1(\boldsymbol{r}_1) | \mathcal{H}_{atom}^1 | \phi_1(\boldsymbol{r}_1) \rangle = \langle \phi_2(\boldsymbol{r}_2) | \mathcal{H}_{atom}^2 | \phi_2(\boldsymbol{r}_2) \rangle$ the atomic energy, $C = \langle \phi_1(\boldsymbol{r}_1)\phi_2(\boldsymbol{r}_2) | \mathcal{H}' | \phi_1(\boldsymbol{r}_1)\phi_2(\boldsymbol{r}_2) \rangle$ the Coulomb integral and $X = \langle \phi_1(\boldsymbol{r}_1)\phi_2(\boldsymbol{r}_2) | \mathcal{H}' | \phi_1(\boldsymbol{r}_2)\phi_2(\boldsymbol{r}_1) \rangle$ the exchange integral. The energy difference for the singlet and the triplet state is calculated to

$$E^S - E^T = 2\frac{X - OC}{1 - O^2} \equiv 2J \qquad (1.5)$$

J is called the *exchange constant*. Depending on J either the singlet state with antiparallel aligned spins or the triplet state with parallel aligned spins is favored in energy. For the H_2 molecule discussed here the singlet state is lower in energy, therefore $J < 0$.

An important property of this model is that it does *not* include the electron spin in the Hamiltonian. The electron spin only comes into play by prescribing the asymmetry of the total wave functions. The *Heisenberg model* describes this exchange interaction by explicitely introducing the spin $\boldsymbol{s}$. In this model an effective Hamiltonian modelling the spin-spin interaction for two or more localized electrons

$$\mathcal{H}_{eff} = -2\sum_{i<j} J_{i,j}\boldsymbol{s}_i\boldsymbol{s}_j \qquad (1.6)$$

is introduced [20], with the exchange integral

$$J_{i,j} = \int\int \psi_i(\boldsymbol{r}_1)\psi_j(\boldsymbol{r}_2)\frac{e^2}{4\pi\epsilon_0 r_{12}}\psi_i^*(\boldsymbol{r}_2)\psi_j^*(\boldsymbol{r}_1)d\boldsymbol{r}_1 d\boldsymbol{r}_2. \qquad (1.7)$$

1.1.2 Stoner model of ferromagnetism

In the previous section it was shown that it can be energetically favorable for localized electron systems to align their spins. However, the model presented above is not directly applicable to metallic ferromagnets. In metallic ferromagnetic systems the *itinerant*[2] electrons are responsible for the ferromagnetic ordering. The Stoner model assumes the band structure of the

---

[2]i.e. they are able to move freely through the solid
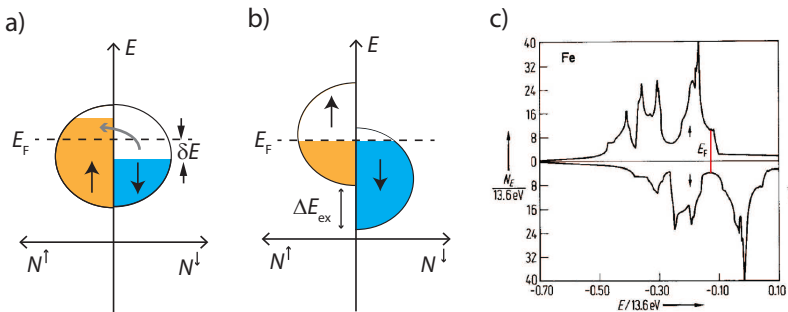
Figure 1.2: a) Schematic of the DOS for spin-up and spin-down electrons. The gray arrow indicates spin-flip processes from the spin-down band to the spin-up band. **b)** The spin-up and the spin-down band are shifted due to exchange splitting by an amount of ΔE_{ex}. This splitting leads to a different DOS for the two spin states. **c)** Calculated DOS for Fe. The figure is taken from [21]

ferromagnet to be separated in a spin-up and a spin-down band. The ferromagnetic ordering goes along with an energy minimization by a spontaneous spin splitting of the valence bands.

A possible implementation are spin-flip processes where electrons from the spin-down band change to the spin-up band[3]. Spin-down electrons with energies between E_{F} and $E_{\mathrm{F}} - \delta E$ flip into spin-up energy states between E_{F} and $E_{\mathrm{F}} + \delta E$ as shown schematically in fig. 1.2a, leading to a rise in kinetic energy

$$\Delta E_{kin} = \frac{1}{2} N(E_{\mathrm{F}})(\delta E)^2 \tag{1.8}$$

where $N(E_{\mathrm{F}})$ is the density of states (DOS) at the Fermi level. At first sight we just created a situation with an increased kinetic energy. However, this energy increase can be balanced or even exceeded by the exchange interaction of the electrons. The molecular field theory (MFT) assumes the electron spins to be affected by a mean field λM induced by the other electrons[4]. Assuming each electron has a magnetic moment $1\mu_{\mathrm{B}}$ (the Bohr magneton[5]), the magnetization of the system can be written as $M = \mu_{\mathrm{B}}(n_\uparrow - n_\downarrow)$, with $n_{\uparrow(\downarrow)} = \frac{1}{2}n \pm \frac{1}{2}N(E_F)\delta E$ the number of spin-up and spin-down electrons

---

[3]The theoretical description of the Stoner criterion and the Stoner enhancement in this section follows chapter 3.3 in ref. [22] and chapter 7.3 in [23].

[4]λ is a factor determining the strength of the molecular field for a given magnetization M.

[5]$\mu_{\mathrm{B}} = \frac{e\hbar}{2m_{\mathrm{e}}} \approx 5.788 \cdot 10^{-5}$ eV/T, with e and m_{e} the electron charge and mass.

after the spin-flip process. The change in the potential energy (molecular field energy) can be calculated from the magnetization

$$\Delta E_{pot} = -\frac{1}{2}\mu_0 M \cdot \lambda M = -\frac{1}{2}\mu_0 \mu_{\mathrm{B}}^2 \lambda (n_\uparrow - n_\downarrow)^2. \tag{1.9}$$

When we write $\mathcal{U} = \mu_0 \mu_{\mathrm{B}}^2 \lambda$ as a measure for the exchange energy, the potential energy simplifies to

$$\Delta E_{pot} = -\frac{1}{2}\mathcal{U} \cdot (N(E_{\mathrm{F}})\delta E)^2. \tag{1.10}$$

The sum of the two competing energies gains the total change in energy of the situation described above

$$\Delta E_{tot} = \Delta E_{\mathrm{kin}} + \Delta E_{\mathrm{pot}} = \frac{1}{2}N(E_{\mathrm{F}})(\delta E)^2(1 - \mathcal{U} \cdot N(E_{\mathrm{F}})). \tag{1.11}$$

Spontaneous ferromagnetic behavior is obtained for $\Delta E_{\mathrm{tot}} \leq 0$. This leads to the condition

$$\mathcal{U} \cdot N(E_{\mathrm{F}}) \geq 1 \tag{1.12}$$

known as the *Stoner criterion* for ferromagnetism. To fulfill this criterion, strong Coulomb (exchange) interaction and a large DOS at the Fermi level are needed. These conditions are met for the 3d transition metals Fe, Co and Ni. For these metals the spin-up and spin-down bands will split by the *exchange splitting* ΔE_{ex} without the need of an external magnetic field as illustrated in fig. 1.2b. The schematic shown before uses simple semicircles to describe the DOS. As an example of a more substantial DOS a calculation for Fe is shown in fig. 1.2c (taken from [21]).

If the Stoner criterion is not fulfilled, spontaneous ferromagnetic behavior is not possible. However, a modification of the magnetic susceptibility of the metals can occur. When an external magnetic field is applied, it introduces in combination with the electronic interactions an energy shift, leading to a magnetization in the material. The magnetic susceptibility can be calculated from this energy shift

$$\chi = \frac{\chi^{\mathrm{P}}}{1 - \mathcal{U} \cdot N(E_{\mathrm{F}})}. \tag{1.13}$$

This *Stoner enhancement* leads to an enhancement of the paramagnetic (Pauli) susceptibility χ^{P} [23]. Pd and Pt are for this reason 'nearly' ferromagnetic.

It has been shown above that the *magnetization* in a ferromagnetic material can be defined as the difference between spin-up and spin-down electrons.

Another important property is the *spin polarization* of the conduction electrons at the Fermi level. This spin polarization is given by the difference in the DOS of the *majority spin* electrons (+) and the *minority spin* electrons (-), where majority and minority refer to an alignment of the spin parallel and antiparallel to the magnetization:

$$P = \frac{N^+(E_{\mathrm{F}}) - N^-(E_{\mathrm{F}})}{N^+(E_{\mathrm{F}}) + N^-(E_{\mathrm{F}})}. \tag{1.14}$$

$|P|$ takes values between 0 (unpolarized) and 1 (half-metal). It has to be noted that in electronic spin transport experiments it is sometimes not possible to express the spin polarization in terms of the density of states of the contacts but transport and interface effects have to be considered. It is then more common to express the polarization in terms of the currents I^+ and I^- of the majority and minority spin electrons, respectively [24]

$$P_{\mathrm{I}} = \frac{I^+ - I^-}{I^+ + I^-}. \tag{1.15}$$

1.1.3 Magnetic anisotropy and domains

The *magnetization* $\boldsymbol{M}$ in a ferromagnetic material is not isotropic but aligns with preferred *easy axis* when no external magnetic field is applied. Energy has to be invested by an external magnetic field to rotate $\boldsymbol{M}$ into a certain direction different from these axis. The most important magnetic anisotropies for us are the magneto crystalline anisotropy and the shape anisotropy. In addition, magnetic anisotropy effects can also be induced by mechanical stress, surfaces or external fields [22].

The origin of the *magneto crystalline anisotropy* is the spin-orbit interaction. In a solid, the electron orbitals are connected to the crystallographic stucture. The interaction with the electron spins leads to an alignment of the magnetization axis along the preferred crystalline axis of minimal energy. The magnetization is an axial vector, leading to a constant anisotropy energy density E_{A} when the magnetization is inverted. Therefore, E_{A} can be written in a series expansion neglecting the odd terms [20]

$$E_{\mathrm{A}} = K_1 \sin^2(\theta) + K_2 \sin^4(\theta) + K_3 \sin^6(\theta) + ... \tag{1.16}$$

with K_i ($i = 1, 2, ...$) the magneto crystalline anisotropy constants. The angle θ is measured between $\boldsymbol{M}$ and the easy magnetization axis as shown in fig. 1.3a. For magnetic particles with uniaxial anisotropy, as assumed in the Stoner-Wohlfarth model below, we only consider the first summand of the equation.
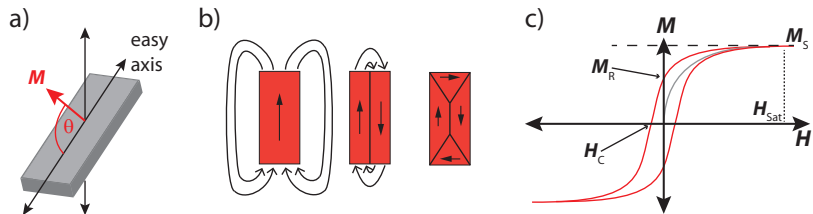
Figure 1.3: a) Schematic of a magnetic solid: the magnetization M includes an angle θ with the easy axis in a magnetic solid. **b)** From left to right: A single domain FM material has a large stray field. The stray field can be reduced by forming multiple domains. An enclosure domain has no stray field outside the material. **c)** Magnetization hysteresis loop of an FM material.

If a crystalline sample is highly isotropic, no magnetization axis will be preferred due to the magneto crystalline anisotropy. However, only for a spherical shape the direction of magnetization will be arbitrary. Magnetic dipole-dipole interactions lead to a *shape anisotropy*. At the surface of an arbitrary shaped magnetic sample magnetic poles are forming, causing a *stray field* outside the sample and a *demagnetizing field* inside the sample. This leads to a reduction of the total magnetic moment. The demagnetizing field H_d can be linked to the magnetization with the help of the geometry dependent *demagnetization tensor* $\mathcal{N}$

$$H_\mathrm{d} = -\mathcal{N}M. \tag{1.17}$$

An easy representation for the demagnetization tensor can only be found for simple geometries like spheres $\mathcal{N} = \begin{pmatrix} 1/3 & 0 & 0 \\ 0 & 1/3 & 0 \\ 0 & 0 & 1/3 \end{pmatrix}$, infinitely long cylinders $\mathcal{N} = \begin{pmatrix} 1/2 & 0 & 0 \\ 0 & 1/2 & 0 \\ 0 & 0 & 0 \end{pmatrix}$ or thin layers $\mathcal{N} = \begin{pmatrix} 0 & 0 & 0 \\ 0 & 0 & 0 \\ 0 & 0 & 1 \end{pmatrix}$.

The last identification important for experiments with magnetic thin films. The minimization of the stray field energy leads to a favored magnetization parallel to the film surface (in-plane) [22].

Stray fields are minimized by the separation of a big uniformly magnetized region into different areas with parallel orientation of the magnetic moments, called *magnetic domains*. The domains are separated by *domain walls*, a gradual reorientation of individual moments across a distance of a few tens of nm. The domain formation process costs energy, but it is mostly favored due to the released stray field energy. Single domain objects will have a

large stray field as depicted in the left schematic of fig. 1.3b. The lowest
stray field is given by a *closure domain* when the field lines are closed inside
the magnet as depicted in the right schematic. Small magnetic particles ($<$
a few hundreds of nm [25]) will not exhibit domain formation. The energy
gain by reducing the stray field cannot compensate the domain formation
energy anymore. Therefore, it is favorable for small samples to remove the
domain walls

The response of the magnetization in a magnetic material to an external
magnetic field can be depicted in a *magnetization curve*. A basic magneti-
zation hysteresis loop for a multi-domain FM is shown in fig. 1.3c. Starting
from zero magnetic field the magnetization will follow the initial magneti-
zation curve (gray). Domain walls will move with increasing external field,
and the total magnetization is aligned in one direction. At the saturation
field $\boldsymbol{H}_{\mathrm{Sat}}$ the magnetization $\boldsymbol{M}_{\mathrm{S}}$ is saturated. When the applied magnetic
field is ramped back to zero, the system remains in the state of remanent
magnetization $\boldsymbol{M}_{\mathrm{R}}$. In order to demagnetize the system the coercive field
$\boldsymbol{H}_{\mathrm{C}}$ has to be applied. This process can be continued leading to a hysteretic
behavior.

1.1.4 Stoner-Wohlfarth model

The magnetization of single domain magnets in external magnetic fields
has been studied by L. Néel in 1947 [26], and E.C. Stoner and E.P. Wohl-
farth in 1948 [27]. The *Stoner-Wohlfarth model* assumes elliptical magnetic
nanoparticles with an uniaxial anisotropy constant K favouring a direction
that includes the shape and the crystalline anisotropy, and a magnetiza-
tion $\boldsymbol{M}$ with constant magnitude [25]. Effects due to magnetic domains
and inhomogeneities in the structure are neglected. The direction of the
magnetization depends on two competing effects and can only move in a
two-dimensional plane. One effect is caused by the uniaxial anisotropy and
the other one by the external magnetic field $\boldsymbol{H}$. The total energy per unit
volume is the sum of the first term of the anisotropy energy density E_{A} (eq.
1.16) and the Zeeman energy per unit volume $E_{\mathrm{Z}} = -\mu_0 \boldsymbol{H} \cdot \boldsymbol{M}$ [25]

$$E_{\mathrm{SW}} = E_{\mathrm{A}} + E_{\mathrm{Z}} = K \sin^2(\theta) - M_{\mathrm{S}} \mu_0 H \cos(\alpha - \theta). \qquad (1.18)$$

θ and α are the angles enclosed by $\boldsymbol{M}$ and $\boldsymbol{H}$ with the easy axis of anisotropy
as shown in fig. 1.4. $\boldsymbol{M}$ will align with an axis of minimal total energy by
either a smooth rotation or a sudden switching.

If a magnetic field is applied parallel to the anisotropy axis, the energy
function E_{SW} has two minima. The first minimum is found for $\theta = 0°$ and
$-\frac{2K}{\mu_0 M_{\mathrm{S}}} < H$, for the second minimum at $\theta = 180°$ the condition $H < \frac{2K}{\mu_0 M_{\mathrm{S}}}$
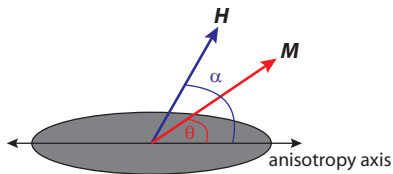
Figure 1.4: In the Stoner-Wohlfarth model a single domain FM particle with magnetization M in an external applied field M is assumed. The corresponding angles to the anisotropy axis θ and α are shown in the schematic.

has to be fulfilled [28]. Therefore, the intrinsic switching field, the field where the magnetization jumps from one energy minimum to another (in this model the coercive field) can be defined as

$$H_{\mathrm{S}} \equiv \frac{2K}{\mu_0 M_{\mathrm{S}}}. \tag{1.19}$$

The Stoner-Wohlfarth model will be used later to model the magnetization reversal of our ferromagnetic contacts.

1.2 Magnetoresistance effects in standard structures

Spintronic devices use the electron spin degree of freedom to control electron transport (see e.g.[2, 29]). In general, spin polarized currents are injected by ferromagnetic materials. After an introduction to spin injection, transport and detection some magnetoresistance effects and generic spintronics devices are presented.

1.2.1 Spin injection, accumulation and detection

A ferromagnetic material shows a spin polarization due to exchange splitting. By applying an electric field, it is possible to drive a spin-polarized current across the interface from an FM into a non-magnetic material. This is not trivial, because it was not clear from the beginning if a coupling exists between electronic charge and the spin at an interface between a ferromagnetic and a non-magnetic metal [30]. Spin injection has been successfully demonstrated into normal metals [30], superconductors [31], and semiconductors (SC) [32].

Spin injection in metals is described theoretically by P.C. van Son *et al.* [33], and T. Valet and A. Fert [34]. An FM material shows a spin polarization due to the different DOS at the Fermi level for $\uparrow$ and $\downarrow$ electrons. When an electrical voltage V is applied across an interface to a non-magnetic metal a spin polarized current is driven into the material (fig. 1.5a). This induces a non-equilibrium asymmetry in the spin-band population of the

metal (fig. 1.5b). The induced difference in the electrochemical potential for up- and down-spins is called *spin accumulation*. The spin accumulation decays with increasing distance from the interface due to spin relaxation processes [35].

Schmidt *et al.* [36] depicted a fundamental obstacle for spin injection over an FM/SC interface: the *conductivity mismatch*. The spin injection is found to be proportional to σ_{SC}/σ_{FM} beeing negligible for a SC with low σ_{SC} (σ_{SC} and σ_{FM} are the conductivities of the FM and SC, respectively). This mismatch leads to a depolarization of the current in the FM before it reaches the interface [37]. A possible solution to overcome this problem is to use half-metallic ferromagnets with a spin polarization of $100\,\%$ as injection material [38]. Another possibility is to have a large interface resistance due to a tunneling barrier [39]. Common barrier materials are Al_2O_3 and MgO [40, 41]. Even better results can be obtained for spin-dependent interface layers between the FM and the SC [42]. A spin-filter effect can also be obtained for atomically ordered and oriented interfaces [43]. For the injection of a spin polarized current in carbon nanotubes the main scattering source will be the interface between the FM and the CNT leading to a tunneling barrier [12]. An additional interface layer is not necessary.

The *spin transport* in a ferromagnetic material can be described by a two-current model proposed by Mott [45]. It assumes that the current channels for the spin-up and the spin-down electrons show different resistances due to different scattering rates for the two spin species. The spin-dependent
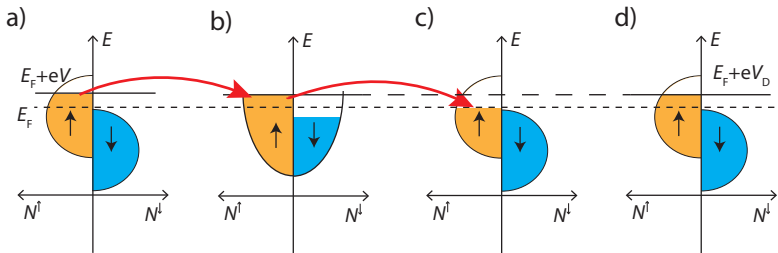
Figure 1.5: a) DOS of an ideal ferromagnet. An electrical voltage V is applied across the interface to drive a spin polarized current in the non-magnetic material. The DOS at E_F in an FM is different for spin-up and spin-down electrons. **b)** When a spin polarized current is injected into the non-magnetic material a non-equilibrium magnetization is induced. **c)** Detection of a spin-polarized current with a second ferromagnet. **d)** If a FM is coupled with a high impedance, its Fermi level will align with the non-equilibrium spins in the non-magnetic material. This figure has been adapted from [44].

conductivities in a ferromagnet are given by[6]

$$\sigma_{\uparrow(\downarrow)} = N^{\uparrow(\downarrow)}e^2 D_{\uparrow(\downarrow)} \quad \text{with} \quad D_{\uparrow(\downarrow)} = \frac{1}{3}v_{\text{F}\uparrow(\downarrow)}l_{\text{e}\uparrow(\downarrow)}. \tag{1.20}$$

$D_{\uparrow(\downarrow)}$ are the spin-dependent diffusion constants, $v_{F\uparrow(\downarrow)}$ the Fermi velocities and $l_{e\uparrow(\downarrow)}$ the mean free paths [46]. With these spin-dependent conductivities the current in the FM can be described separately for the two spin channels

$$j_{\uparrow(\downarrow)} = \frac{\sigma_{\uparrow(\downarrow)}}{e}\frac{\delta\mu_{\uparrow(\downarrow)}}{\delta x} \tag{1.21}$$

with $\mu_{\uparrow(\downarrow)}$ the electrochemical potential. The total charge and spin currents are given by $j_\uparrow + j_\downarrow$ and $j_\uparrow - j_\downarrow$, respectively. Introducing spin-flip processes leads to a diffusion equation for the electrochemical potentials

$$D\frac{\delta^2(\mu_\uparrow - \mu_\downarrow)}{\delta x^2} = \frac{(\mu_\uparrow - \mu_\downarrow)}{\tau_{sf}}. \tag{1.22}$$

Spin-flip processes from one band into the other are in balance, therefore no net spin scattering occurs. D is a diffusion constant, now averaged over both spin species and the spin relaxation time τ_{sf} describes the decay of the spin accumulation. These equations lead to a description of the behavior of the electrochemical potentials in the FM or the non-magnetic material

$$\mu_{\uparrow(\downarrow)} \propto ax \pm \frac{b}{\sigma_{\uparrow(\downarrow)}}exp\left(\frac{-x}{\lambda_{sf}}\right) \pm \frac{c}{\sigma_{\uparrow(\downarrow)}}exp\left(\frac{x}{\lambda_{sf}}\right) \tag{1.23}$$

with the spin relaxation length $\lambda_{sf} = \sqrt{D\tau_{sf}}$. a, b and c can be identified from the boundary conditions. They are given by the continuity of the electrochemical potentials and the conservation of the spin currents at the interfaces [46].

In the absence of magnetic impurities in the conductor the main scattering mechanisms leading to spin equilibration are provided by spin-orbit interactions (SOI) and hyperfine interactions [2]. The most important spin-orbit interactions are the D'yakonov-Perel mechanism where a lack of inversion symmetry leads to internal magnetic fields and the Elliot-Yaffet mechanism describing lattice ion induced interaction mixing spin-up and spin-down states [47]. The hyperfine interaction leads to a dephasing of the spin because of interactions with the nuclei.

Spin detection is achieved with an additional ferromagnet. When the FM is coupled with a low impedance to the non-magnetic metal, a current proportional to the induced magnetization can flow. This is schematically

---

[6]This theoretical description follows ref. [46]

shown in fig. 1.5c. The Fermi level of an FM coupled with a high impedance allligns with the non-equilibrium spins in the non-magnetic metal and leads to measurable voltage V_D as indicated in fig. 1.5d [44].

1.2.2 Anisotropic magnetoresistance

In an FM material a change in resistance depending on the relative orientation of the magnetization $\boldsymbol{M}$ and the direction of the electrical current $\boldsymbol{I}$ is observed. This effect was discovered by W. Thomson (Lord Kelvin) in 1856 and is called *anisotropic magnetoresistance* (AMR) [20]. AMR can be explained by a spin-orbit coupling on the $3d$ orbitals. It goes along with anisotropic intra-band $s - d$ spin-flip scattering processes.

In *Mott's picture* [45] the current in a ferromagnet is carried by the s electrons and the electrical resistance is caused by scattering processes with the d band. Majority s band electrons can be scattered into empty minority d states. The scattering scales with the number of available d states. Due to an orbital anisotropy of the d states, the scattering depends on the relative orientation between the magnetization and the current directions. The magnetoresistance can be calculated by splitting the current in a part parallel and a part perpendicular to the magnetization [48]. With θ beeing the angle between $\boldsymbol{M}$ and $\boldsymbol{I}$, the resistance is

$$R(\theta) = R_\parallel \cdot \cos^2(\theta) + R_\perp \cdot \sin^2(\theta) = R_\perp + (R_\parallel - R_\perp) \cdot \cos^2(\theta). \quad (1.24)$$

$R_\parallel$ and $R_\perp$ are the resistance values for $\boldsymbol{M}\|\boldsymbol{I}$ and $\boldsymbol{M}\perp\boldsymbol{I}$, respectively.

The AMR leads to changes in resistance of a few percent. With this effect the magnetic properties of FM materials can be studied by transport experiments. In particular, information can be gained for structures that are to small for other magnetization detection methods (see Chapter 3).

1.2.3 Spin-valve structures

A fundamental spintronics device is a *spin-valve*, a hybrid structure of ferromagnetic (FM) metals and a non-magnetic (NM) medium. Fig. 1.6a shows a schematic of a *vertical* spin-valve where two FM layers are separated by an NM layer. The resistance of the device depends on the magnetization configuration of the two FM metals, and can be controlled by an external magnetic field. Giant magnetoresistance devices [6], magnetic tunnel junctions [49] and nanopillars [50] are a few examples of a large variety of vertical spin-valves.

More interesting for nanoelectronics are *lateral* spin-valves, where a medium is generally contacted with FM metals from above and perpendicular to the current direction as schematically depicted in fig. 1.6b. An advantage of
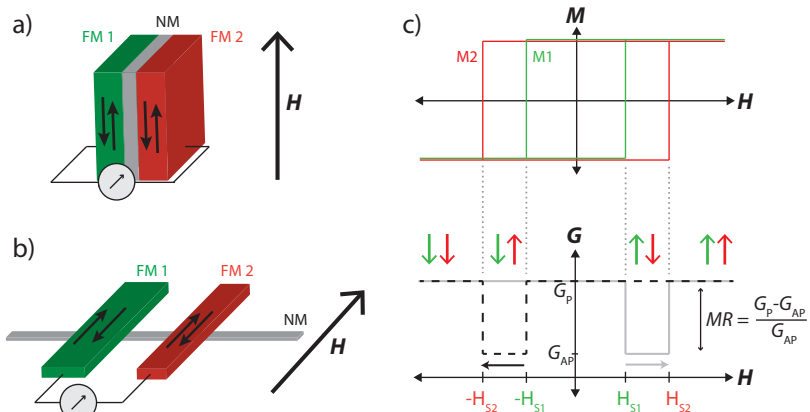
Figure 1.6: a) Schematic of a vertical spin-valve. Two FM layers are separated by a non magnetic interlayer. **b)** In the lateral geometry a non-magnetic medium is contacted from above by FM electrodes. **c)** Assuming that both FM are switching their magnetization at different switching fields H_S, a reduction in the device conductance can be seen when both FM are magnetized antiparallel.

this geometry is the possibility of contacting low-dimensional materials like metallic strips [51], semiconducting nanowires [52], graphene [53] or CNTs [18, 19], and it is possible to create multiple terminals [51, 54].

The expected behavior for the spin-valve conductance in an external magnetic field is illustrated in the lower part of fig. 1.6c. For simplicity, a sharp magnetization reversal of the two FM contacts at the switching fields H_{S1} and H_{S2} is assumed as shown in the rectangular magnetization curves in the upper graph. The conductance shows a hysteretic reduction when the contacts switch from a parallel to an antiparallel configuration. The magnetoresistance of the device is defined as[7]

$$MR = \frac{R_{AP} - R_P}{R_P} = \frac{G_P - G_{AP}}{G_{AP}}. \tag{1.25}$$

1.2.4 Tunnel magnetoresistance

In general, a tunnel magnetoresistance (TMR) device consists of two FM contacts separated by an insulator. The electron transport from one contact

---

[7]The term magnetoresistance is generally used in literature, also when measuring conductances [55]. Other definitions in use for the magnetoresistance are $MR' = \frac{G_{AP} - G_P}{G_P}$ and $MR'' = \frac{G_P - G_{AP}}{G_P + G_{AP}}$.

to the other is dominated by tunneling through a barrier and the MR can amount to a few hundered percent at room temperature [56]. In the *Jullière model* [9] the transmission through the insulating interlayer is assumed independent of the electron energy but proportional to the DOS at the Fermi level E_F of both contacts. Spin-flip processes at the interfaces and in the interlayer are neglected.

The situation for parallel alignment of the FM layers is depicted in fig. 1.7a and is described in Mott's two-current model [45]. A large amount of spin-up electrons (high DOS at E_F) from one contact can tunnel into empty spin-up states with a high $DOS(E_F)$ in the other contact, resulting in a high tunnelling current. For the spin-down electrons, the low DOS at the Fermi level in both ferromagnets leads to a low tunnel current and therefore a higher resistance. For antiparallel alignment of the magnetizations the tunneling current for the spin-up electrons is decreased due to a smaller amount of empty up-spin states in the second FM, wheareas the current for the spin-down states is increased as shown in fig. 1.7b. The total tunnelling current is smaller in the antiparallel case where the low spin-up resistance is dominating (see resistor schematic in fig. 1.7).

Using Fermi's golden rule, the tunnelling current is proportional to the product of the density states $N_i(E_F)$ at the Fermi level for both electrodes ($i = 1, 2$) and the square of the tunnel matrix element $\mathcal{M}$ [57]. The tunnel matrix element is assumed to be independent of energy for a small variation in the energy window between E_F and $E_F - eV$. The first order tunneling current then reads

$$I = \frac{2e}{h}|\mathcal{M}|^2 \int_{-\infty}^{\infty} N_1(E - eV)N_2(E)[f(E - eV) - f(E)]dE \qquad (1.26)$$

with $f(E)$ the Fermi function.

Assuming low temperatures and the DOS not varying much for small applied voltages V, the conductance in the parallel (P) and the antiparallel (AP) configuration is given by

$$G_P = G_{P,\uparrow} + G_{P,\downarrow} \sim N_1^+ N_2^+ + N_1^- N_2^- \qquad (1.27)$$

$$G_{AP} = G_{AP,\uparrow} + G_{AP,\downarrow} \sim N_1^+ N_2^- + N_1^- N_2^+ \qquad (1.28)$$

with $G_{\uparrow(\downarrow)}$ the conductance of the spin-up (spin-down) channel and $N_i^{+(-)}$ the DOS for electrode $i = 1, 2$ for majority (+) and minority (-) spin electrons. By inserting these expressions into the definition of the magnetoresistance (eq. 1.25), a *tunneling magnetoresistance* in terms of the contact
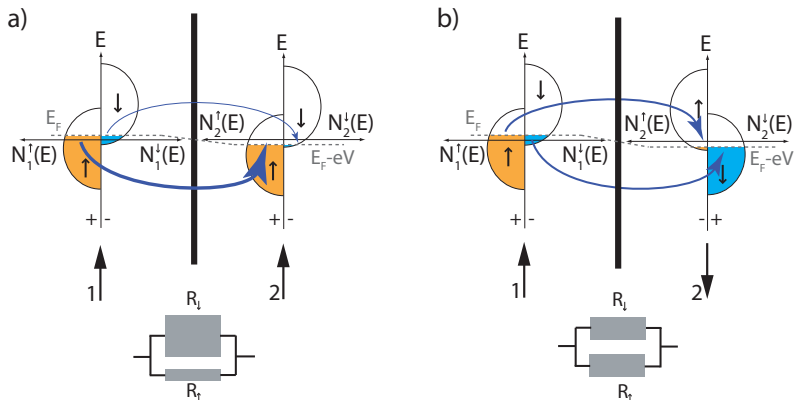
Figure 1.7: Schematic of the electron tunneling between two FM layers following the Jullière model. In a Stoner ferromagnet, the DOS of the 3d bands is spin-split at the Fermi level which leads to a finite polarization of the charge carriers. The current through the device is assumed to be independent of the electron energy but proportional to the DOS. This leads to a smaller resistance of the device in **a)** the parallel than in **b)** the antiparallel configuration.

polarization P_1 and P_2 (eq. 1.14) is found

$$TMR = \frac{G_{\mathrm{P}} - G_{\mathrm{AP}}}{G_{\mathrm{AP}}} = \frac{2P_1P_2}{1 - P_1P_2}. \tag{1.29}$$

Jullière's model is a basic model that can help to understand basic features of TMR devices. However, in experiments TMR values are found that cannot be explained by this model (see Chapter 4). This is due to the fact that the model does not include spin-flip effects in the barrier and at the interfaces.

1.2.5 Spin field-effect transistor

An example of a more complex spintronic device that allows modifications of the magnetoresistance by control of the spin currents between two FM materials, the *spin field-effect transistor* (spin FET) has been envisioned by S. Datta and B. Das [58] in 1990 (see fig. 1.8). The spin polarized current is injected from an FM electrode into a low-dimensional channel, for example provided by a two-dimensional electron gas (2DEG). The injected electrons move ballistically to the FM detector. In the moving frame of the electrons the electric field of the gate is transformed partially to a magnetic field perpendicular to their moving direction. The moving electron spins will

precess about this magnetic field and are projected on the detector electrode. The underlaying spin-orbit interaction is called Rashba spin-orbit coupling [2] and has the largest effect in materials with large spin-orbit coupling [59]. Modification of the gate voltage V_G leads to different precession and different currents detected in the FM detector.
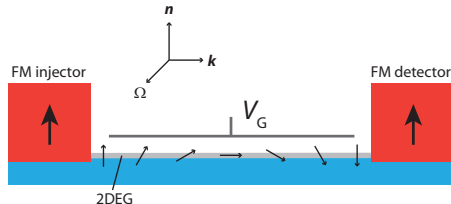

Figure 1.8: Schematic of the Datta-Das spin FET. A spin-polarized ballistic current is injected and detected by two FM electrodes. The spin precession of the electrons about an effective magnetic field by the Rashba effect can be controlled by a gate voltage V_G.

1.3 Carbon nanotube quantum dots

In this thesis we use *carbon nanotubes* (CNTs) as spin transport medium. One can imagine a CNT as a 2D hexagonal network of carbon atoms, a single graphene sheet, that has been rolled up into a cylinder. These so-called single wall CNTs (SWCNTs) have a diameter on the order of a few nanometers and a typical length in the micrometer range. SWCNTs can be either metallic or semiconducting with varying band gap. The discovery of SWCNTs was made by Sumio Iijima in 1993 [60], two years after its first observation of multi walled CNTs [13] (many concentric CNTs).

SWCNTs are often considered as prime examples of one-dimensional systems [12]. The electron mean free path in CNTs is several μm long [61], up to $10\,\mu$m [15]. When the mean free path exceeds the tube length, the transport is ballistic. The carbon isotope ^{12}C, making up $99\,\%$ of the carbon in CNTs, has no nuclear spin, making hyperfine interaction negligible. In addition, due to the low atomic number of carbon, spin-orbit interaction is weak. The length scale over which coherent spin transport is possible can be $1\,\mu$m [62]. This makes CNTs ideal media for spintronic devices.

1.3.1 Electronic properties of a graphene sheet

In a graphene sheet, every carbon atom has three nearest neighbors with a C-C bond length of $a_0 = 1.42$ Å. The unit cell, defined by the lattice vectors

$\boldsymbol{a}_1$ and $\boldsymbol{a}_2$, contains two carbon atoms and is shown in fig. 1.9a (shaded in orange). Graphene is sp^2 hybridized. The (s, p_x, p_y) orbitals form strong covalent σ bonds. These bonds determine the binding energy and the elastic properties of the sheet. The p_z orbitals form delocalized π (bonding) and π^* (antibonding) orbitals by overlap with their neighboring orbitals [14].

The dispersion relation can be calculated using a tight binding model [14, 63] taking only nearest neighbors into account and yields

$$E(\boldsymbol{k}) = \pm\gamma\sqrt{3 + 2\cos(\boldsymbol{k}\boldsymbol{a}_1) + 2\cos(\boldsymbol{k}\boldsymbol{a}_2) + 2\cos(\boldsymbol{k}(\boldsymbol{a}_2 - \boldsymbol{a}_1))} \qquad (1.30)$$

with γ the overlap integral.

The positive and negative solutions describe the π^* and the π band, respectively. A three dimensional plot of the energy dispersion relation is shown in fig. 1.9b. The two bands meet at six distinct points corresponding to the corners of the first Brillouin zone. Due to the symmetry of the hexagonal lattice, three out of the six points are equivalent. The two non-equivalent points are called K and K$'$. The energy dispersion is linear close to the K-points. This is in contrast with the dispersion of more conventional electron systems (with parabolic bands).

The low energy properties can be described by a linear expansion of the

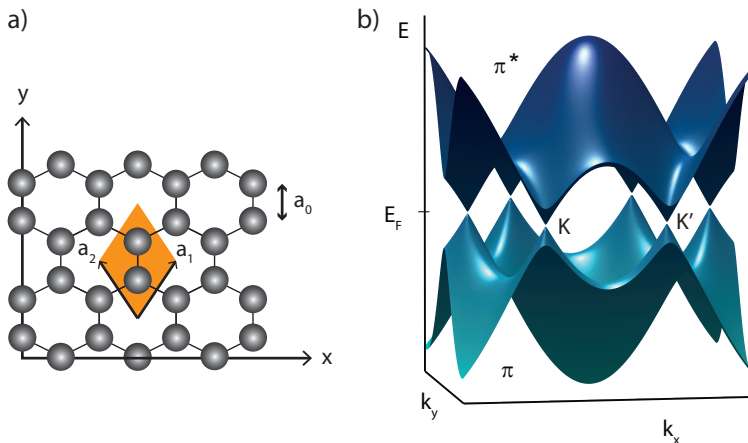**Figure 1.9: a)** Schematic of the hexagonal structure of graphene. The unit cell defined by the lattice vectors $\boldsymbol{a}_1$ and $\boldsymbol{a}_2$ contains two carbon atoms. **b)** Three dimensional plot of the energy dispersion relation of graphene. The antibonding (π^*) and bonding (π) band form six valleys and meet at the six K-points corresponding to the corners of the first Brillouin zone.

wave functions around a K-point. With $\boldsymbol{\kappa} = \boldsymbol{k} - \boldsymbol{K}$, the low energy dispersion relation can be written as [63]

$$E(\boldsymbol{\kappa}) = \pm \hbar v_{\mathrm{F}} |\boldsymbol{\kappa}| \tag{1.31}$$

with the Fermi velocity $v_{\mathrm{F}} = 3\gamma a_0 / 2\hbar \approx 10^6 \, \mathrm{m/s}$ for $\gamma = 3 \, \mathrm{eV}$ [64].

1.3.2 Rolling up graphene into a nanotube

One can imagine a CNT as a slice of a graphene sheet rolled up into a cylinder to form a seamless tube. Regarding its electronic properties, the CNT can behave either metallic or semiconducting. The geometrical structure of the tube depends on its circumferential or *wrapping vector* $\boldsymbol{W} = n\boldsymbol{a_1} + m\boldsymbol{a_2}$ with $n, m \in \mathbb{N}$ as illustrated in fig. 1.10a. The orange shaded area in the figure depicts the tube surface area. The translation vector $\boldsymbol{T}$ points parallel to the long axis of the nanotube.
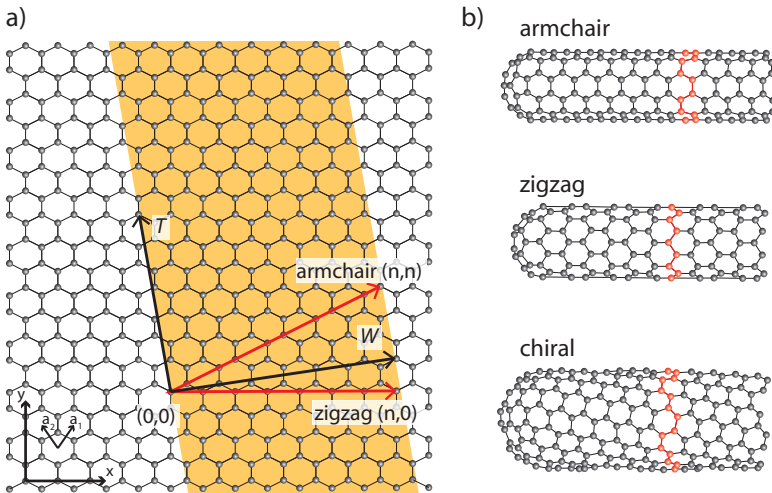
Figure 1.10: a) Schematic of the graphene honeycomb structure. The orange region defines an area that can be rolled up into a CNT. The wrapping vector $\boldsymbol{W}$ defines the circumference of the tube. The vector $\boldsymbol{T}$ points along the tubes long axis. **b)** Different CNT structures result, depending on the wrapping vector. The illustration shows armchair, zigzag and chiral type CNTs. The carbon atoms along the wrapping vector are highlighted red. (adapted from ref. [12, 65])

The tube diameter is found as

$$d = \frac{W}{\pi} = \frac{a}{\pi}\sqrt{n^2 + m^2 + nm} \tag{1.32}$$

with $a = \sqrt{3}a_0$ [12].

Depending on the indices (n, m) one can classify the CNTs into different groups. CNTs with wrapping indices (n, n) are called *armchair tubes*. *Zigzag tubes* are characterized by indices $(n, 0)$. Tubes with arbitrary indices are *chiral* (see fig. 1.10b for illustration).

The wave functions in CNTs have to obey periodic boundary conditions around the circumference. The wave vector $\boldsymbol{\kappa}$ can be separated into one component parallel ($\boldsymbol{\kappa}_\parallel$) and one perpendicular to the nanotube axis ($\boldsymbol{k}_\perp$). Because of the tube length of several micrometers (compared to a diameter of around one nanometer), $\boldsymbol{\kappa}_\parallel$ can be assumed continuous [65], whereas the allowed values of $\boldsymbol{\kappa}_\perp$ are restricted by

$$\boldsymbol{W} \cdot \boldsymbol{\kappa} = \pi d \, \kappa_\perp = 2\pi \left(\frac{m - n}{3} + p\right) \tag{1.33}$$

with $p \in \mathbb{Z}$ [63]. This quantization corresponds to cross sections in the graphene band structure. If such a cross section contains K or K', the tube is metallic, i.e. has a finite DOS, while it has a band gap when it does not. The two situations are schematically shown in the plot of the energy cones
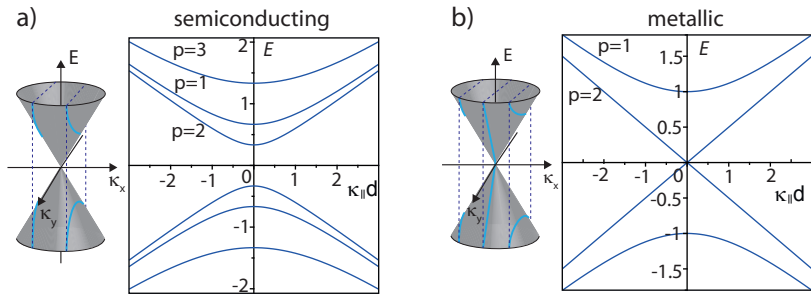
Figure 1.11: Low energy approximation of the graphene band structure (gray cones). Rolling up graphene: the quantization of the perpendicular component of the wave vector leads to subbands in the graphene band structure (light blue lines). **a)** When the subbands do not include the origin (K-point) the tube is semiconducting. The graph shows a bandstructure plot of the first few bands closest to the K-point of a semiconducting $(5, 0)$ nanotube. **b)** When the K-point is included, the CNT is metallic. In the graph the first bands of a metallic $(6, 0)$ nanotube are plotted. The subbands are indicated with their index p

in fig. 1.11. Inserting eq. 1.33 into eq. 1.31 leads to the energy dispersion relation [63]

$$E(\kappa_\parallel) = \pm \frac{2\hbar v_\mathrm{F}}{d} \sqrt{\left(\frac{m-n}{3} + p\right)^2 + \left(\frac{\kappa_\parallel d}{2}\right)^2}. \qquad (1.34)$$

The energy dispersion only reaches zero for $\kappa_\parallel = 0$ for the subband with the number p, if $(m-n)/3 = -p$. Hence, all tubes with wrapping indices (n, m) obeying $(m-n)/3 \in \mathbb{Z}$ are metallic, the others are semiconducting. Two examples of dispersion relations of a semiconducting $(5,0)$ and a metallic $(6,0)$ tube are shown in figure 1.11. In addition, small band gaps can also be induced in metallic tubes with small diameter or by radial deformation [66].

1.3.3 Quantized transport in CNT quantum dots

In a *quantum dot* (QD) the electron wave functions are confined in three spatial directions to a size on the order of the Fermi wavelength. The energy states of this quasi zero-dimensional (0D) object take on only discrete values. With this respect, QDs are comparable to atoms but have much larger dimensions and the charge carrier number can be tuned externally [67, 68]. Electrical characterization of QDs is often done at cryogenic temperatures, where the single electron levels can be resolved. QD behavior can be found for example in metallic nanoparticles [69], molecules trapped between electrodes [70], self-assembled, lateral or vertical semiconductor nanostructures [71, 72], semiconducting nanowires [73], graphene [74] or CNTs [19].

A CNT can be considered as a one-dimensional conductor. By attaching a source (S) and a drain (D) contact, tunnel barriers form at the interfaces. This leads to the formation of a QD in the CNT (see fig. 1.12a). A highly doped Si wafer, insulated from the CNT by a SiO_2 layer can be used to tune the energy levels of the dot. The coupling of the source (drain) contact is characterized by the capacitance $C_\mathrm{S(D)}$ and the coupling strength $\Gamma_\mathrm{S(D)}$. The backgate has the capacitance C_G. This is depicted schematically in fig. 1.12b.

The *constant interaction (CI) model* is a simplified model to describe this system [72, 75]. The first assumption made in the CI model is that the Coulomb interactions between the electrons on the dot and between the electrons on dot and leads can be described by a single, constant capacitance $C_\Sigma = C_\mathrm{S} + C_\mathrm{D} + C_\mathrm{G}$. Furthermore, the single-particle energy spectrum is assumed independent of the number of electrons n on the dot. The energy spacing between the levels, also called *orbital energy*, is denoted as δE. To add an electron to the QD, the *charging energy* $U_\mathrm{C} = \frac{e^2}{C_\Sigma}$ has to be overcome.
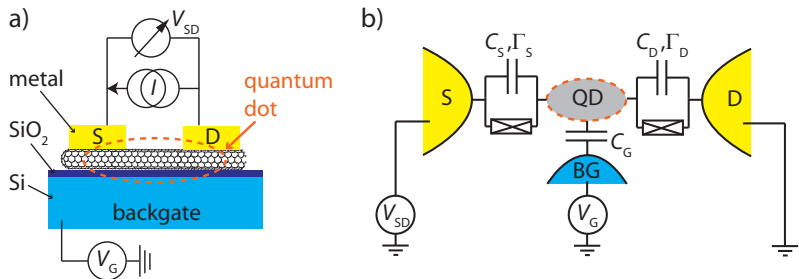
Figure 1.12: a) Side view of a CNT device: a quantum dot (QD) forms in the CNT between two metal contacts. The backgate can be used to tune the levels of the dot. The highly doped Si wafer used as a backgate is insulated from the CNT by a SiO_2 layer. **b)** Schematic of the quantum dot capacitively coupled to a source (S) and a drain (D) contact. The coupling of the source (drain) to the dot is characterized by the coupling strength $\Gamma_{S(D)}$ and the capacitance $C_{S(D)}$. The backgate is coupled with a capacitance C_G.

Typical charging energies for CNTs lie in the range $5 - 20\,\text{meV/L}$ [15] where L is the CNT dot length in μm.

Defect-free CNTs should show a *four-fold degeneracy* of the single-particle levels. This four-fold degeneracy originates from the two-fold spin degeneracy and a two-fold subband degeneracy. Due to Coulomb interaction it costs the charging energy U_C to add electrons in the same level. When a level is filled the next electron has to overcome the charging energy and the orbital energy, $U_C + \delta E$. Four-fold patterns in the conductance are mostly visible in clean CNTs with no perturbations or structural imperfections [76].

A schematic to explain electron transport in a QD in a simplified picture can be seen in fig. 1.13. We assume that the electronic occupation of the leads is described by a Fermi function. At low temperatures, the Fermi function changes to a step function where all electronic states up to the electrochemical potential μ are filled, states above are empty. If the electrochemical potential μ_{QD} of the QD is aligned with the electrochemical potentials of the source μ_S and the drain μ_D (fig. 1.13a) electron transport is possible. Otherwise transport is blocked (fig. 1.13b). The electrochemical potential of the QD can be tuned by an electrical gate. Another possibility of tuning the quantum dot levels by the magneto Coulomb effect, introduced by ferromagnetic leads coupled to the QD, is discussed in chapter 4. Tuning the electrochemical potential of the QD leads to an oscillating conductance of the device, also called *Coulomb oscillations*.

In addition to the temperature broadening $\propto k_B T$, the energy levels of the

QD are broadenend due to life time broadening (Γ-broadening), described by Lorentzian curves. The life time broadening is a consequence of the energy-time uncertainty principle $\Delta E \cdot \Delta t \geq \hbar/2$. The width of the energy level is inversely proportional to the time the electron stays on the dot. The full width at half maximum (FWHM) of a lifetime broadened Coulomb peak is $\Gamma = \Gamma_{\mathrm{S}} + \Gamma_{\mathrm{D}}$ [77].

Another possibility to overcome the Coulomb blockade is to apply a *finite bias voltage* V_{SD} between S and D. This will lift the electrochemical potential of the source to $\mu_{\mathrm{S}} = \mu_{\mathrm{D}} - eV_{\mathrm{SD}}$ as shown in fig. 1.13c. Everytime a level of the dot enters the energy window between μ_{D} and μ_{S} an additional conductance channel opens. To simplify the illustration of the measurements one usually plots the *differential conductance $G = dI/dV$*. The differential conductance shows a peak when a new level enters the energy window.

The lower graph in figure 1.13d is an example of a *charge stability diagram* of a CNT quantum dot. The red lines enclose the *Coulomb diamonds*, the regions where the transport is blocked and the number of electrons on the dot is constant. In the area around these Coulomb diamonds single-electron tunneling can occur. The Coulomb blockade peaks shown in the upper graph in figure 1.13d are the cross section of the Coulomb diamonds at $V_{\mathrm{SD}} = 0\,\mathrm{V}$. The stability diagram provides information about the charging energy and the orbital energy of the dot. The charging energy U_{C} can be read out directly from the height of a typical diamond and the height of every fourth diamond displays the energy $U_{\mathrm{C}} + \delta E$. The diamonds can also be used to calculate the lever arm $\eta = e\frac{C_{\mathrm{G}}}{C_{\Sigma}} = \frac{\Delta V_{\mathrm{SD}}}{\Delta V_{\mathrm{G}}}$ (see fig. 1.13d) of the gate voltage. For asymmetric capacitive coupling of the contacts the slopes $\beta_{+} = |e|\frac{C_{\mathrm{G}}}{C_{\mathrm{S}}}$ on the left and $\beta_{-} = -|e|\frac{C_{\mathrm{G}}}{C_{\Sigma} - C_{\mathrm{S}}}$ on the right side of the diamond will be different and directly yield the source and drain capacitances [75]. The lever arm can then be written as $\eta = \frac{\beta_{+}|\beta_{-}|}{\beta_{+} + |\beta_{-}|}$.
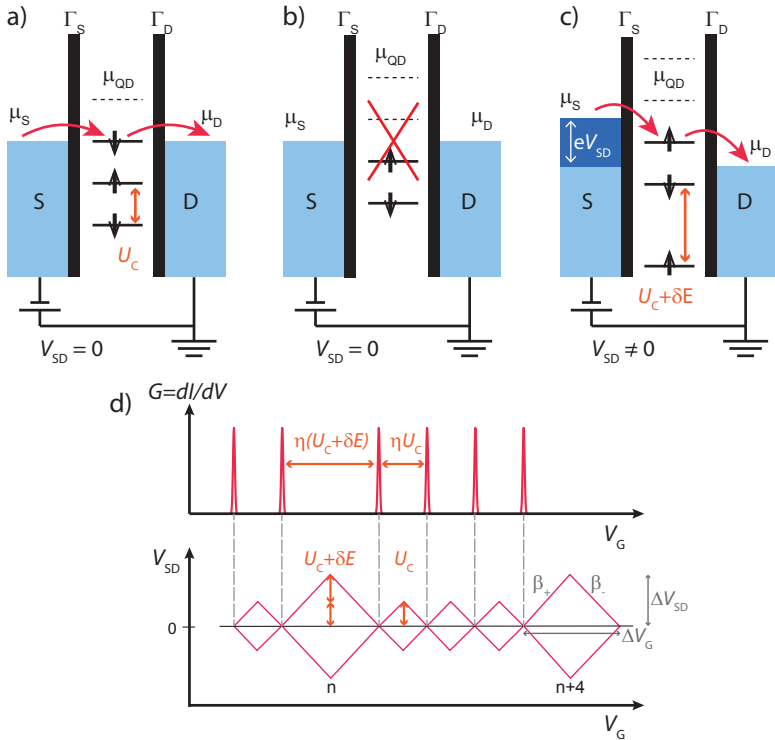
Figure 1.13: a),b) Simplified schematic of the tunneling process through a quantum dot. When the electrochemical potential μ_{QD} of the QD is aligned with the electrochemical potentials μ_S and μ_D of the source and drain contacts, tunneling can take place. The electrochemical potential of the QD can be tuned with a gate voltage. **c)** Applying a finite source-drain voltage opens an energy window between μ_S and μ_D. The dot will conduct when a dot level enters the energy window. **d)** Schematic representation of the differential conductance $G = dI/dV$ (Coulomb blockade oscillations) and the corresponding stability diagram. The edges of the diamonds represent states of high differential conductance. In the situation of symmetric capacitive coupling, the lever arm of the backgate can be determined by $\eta = e\frac{C_G}{C_\Sigma} = \frac{\Delta V_{SD}}{\Delta V_G}$. In general, it is calculated as $\eta = \frac{\beta_+|\beta_-|}{\beta_+ + |\beta_-|}$ with $\beta_{+(-)}$ the left (right) slope of the diamonds.

Chapter 2

Sample Fabrication and Measurements at Cryogenic Temperatures

In this chapter we describe the carbon nanotube (CNT) growth by chemical vapor deposition and the device fabrication process. We discuss the electrical contact to CNTs and introduce briefly the cryostats used for low-temperature measurements and the measurement set-up.

2.1 Wafer preparation

We use a highly boron doped Si wafer with a polished ~ 400 nm thermally grown SiO_2 layer on top. The p-doped substrate has a resistivity of $10\,\mu\Omega$cm and is used as a backgate. The oxide layer insulates the substrate from the device. Pieces of 1 x 1 cm^2 are cut out of the wafer and cleaned in a bath-type sonicator in *acetone* for about one hour to remove dust from cutting and organic residues on the surface. Then the substrate is sonificated for 30 minutes in $2-propanol$ (IPA) to remove residues from the acetone and air blow dried. A 30 seconds *reactive ion etch* (RIE) is used to remove small but persistent organic substances from the wafer surface. In the RIE high-energy ions from a chemically reactive oxygen plasma react with the residues on the wafer surface [78]. The parameters of the process can be found in Appendix A. Alternatively, a 30 minutes UV ozone cleaning, a decomposition of the residues by UV light accompanied by an oxidation by free oxygen radicals [79], is done.

2.2 Carbon nanotube growth

The CNTs used in the experiments are grown in-house in a *chemical vapor deposition* (CVD) system. A catalyst solution composed of iron nitrite seed particles ($Fe(NO_3)_3 \cdot 9H_2O$), aluminum oxide (Al_2O_3) and MoO_2Cl_2 is spun on the substrate and heated up to $950°C$ in a quartz tube in an argon atmosphere [80]. The exact composition of the catalyst solution is crucial for the growth process [81, 82] and can be found together with the gas flow rates in appendix A. When the growth temperature is reached, the Ar gas is replaced by methane (CH_4) and hydrogen (H_2) for 10 minutes. The methane serves as feedstock gas and contains the carbon necessary for the nanotube growth. The carbon deposits on the catalyst particles and tube growth takes place [12]. The hydrogen is needed to react with the excess carbon. After the growth process the wafer is cooled down to room temperature in a Ar/H_2 atmosphere. The growth process we use generates mainly individual single wall CNTs with a typical length of 2-10 μm [81, 82].
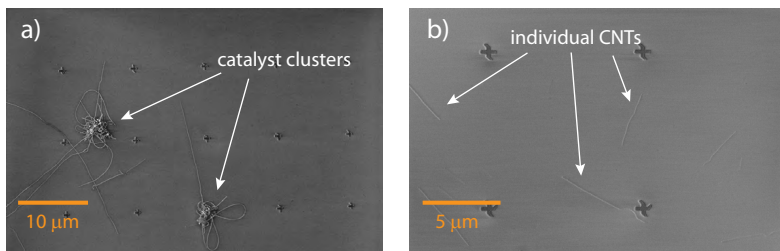
Figure 2.1: SEM images of a wafer with alignment markers and nanotubes after CVD growth. **a)** The catalyst solution has been sonicated in a bath-type sonicator for 3 hours. Catalyst clusters on the surface are clearly visible. **b)** Sonicating the solution in a high-power sonicater prevents clusters on the wafer, leading to a better distribution of the CNTs on the surface.

It should be noted that the catalyst solution has to be treated with ultrasonic to break-up catalyst nanoparticle clusters before it is spun on the wafer. Usually, this is done by placing a small glass container with the catalyst solution in a bath-type sonicator for $\sim$3 hours [81]. However, strong catalyst clusters are often visible after the CNT growth, indicating that bath-sonication is not sufficient to break-up all the clusters (fig. 2.1a). Good results were achieved by sonication of a small amount of catalyst solution in a high-power sonicater[1] (see appendix A). An ideal distribution of individual

---

[1]Branson Digital Sonifier 450

CNTs between four alignment markers can be seen in fig. 2.1b.

2.3 Device fabrication

A grid of alignment markers and the contact pads for bonding are fabricated by electron beam (e-beam) lithography and metal deposition techniques *after* the CNT growth[2]. After the localization of the CNTs, two more fabrication steps for the ferromagnetic and non-magnetic contact materials are done.

General fabrication process

The detailed fabrication process is shown schematically in fig. 2.2. The cleaned wafer piece (fig. 2.2a) ist covered with an e-beam resist double layer (fig. 2.2b). For the double layer a 100 nm thick *polymethyl methacrylat-methacrylic* (PMMA/MA)[3] layer is spin-coated on the wafer (4000 rpm, 40 seconds) and baked on a hot plate at $200°$C for 3 minutes to evaporate the solvents and harden the resist. In a second spin-coating process a 200 nm thick *polymethyl methacrylat* (PMMA)[4] layer is placed on top of the first layer and also hardened on the hot plate ($200°$C, 3 minutes). The lithographic patterning is done with a *Zeiss SUPRA 40* scanning electron microscope (fig. 2.2c). The electron beam cuts the polymer chains of the resist in smaller pieces so that they can be removed in a developer bath consisting of 1 part *methyl isobutyl ketone* (MIBK) and 3 parts IPA. Narrow lines can be structured in the PMMA layer using an acceleration voltage of 20 kV with a 10 μm aperture (details about e-beam lithography parameters can be found in appendix A). After the developing process, a metal is deposited in a *Bestec* evaporation system in ultra high vacuum (UHV) at a pressure $< 5 \cdot 10^{-10}$ mbar by thermal or electron beam evaporation (fig. 2.2d). During metal evaporation the sample holder is cooled to -50$°$C. This helps to reduce the heat load due to the deposited metal atoms and leads to a better lift-off. The walls of the UHV chamber are at -180$°$C. After the metal deposition the unexposed PMMA layer and the metal layer on top are removed in a lift-off process in $\sim$50$°$C warm acetone (fig. 2.2e). The fabricated sample (fig. 2.2f) is then rinsed with IPA and air blow dried.

---

[2]This is in contrast to ultra-clean fabrication methods where the CNTs are grown across pre-formed contacts in the last fabrication step [83]
[3]AR-P 617 33 %, Allresist
[4]AR-P 671.09 950 K, Allresist, diluted in chlorobenzene

a) SiO$_2$ Si

b) PMMA PMMA/MA

c) e-beam

d) metal

e) acetone

f)
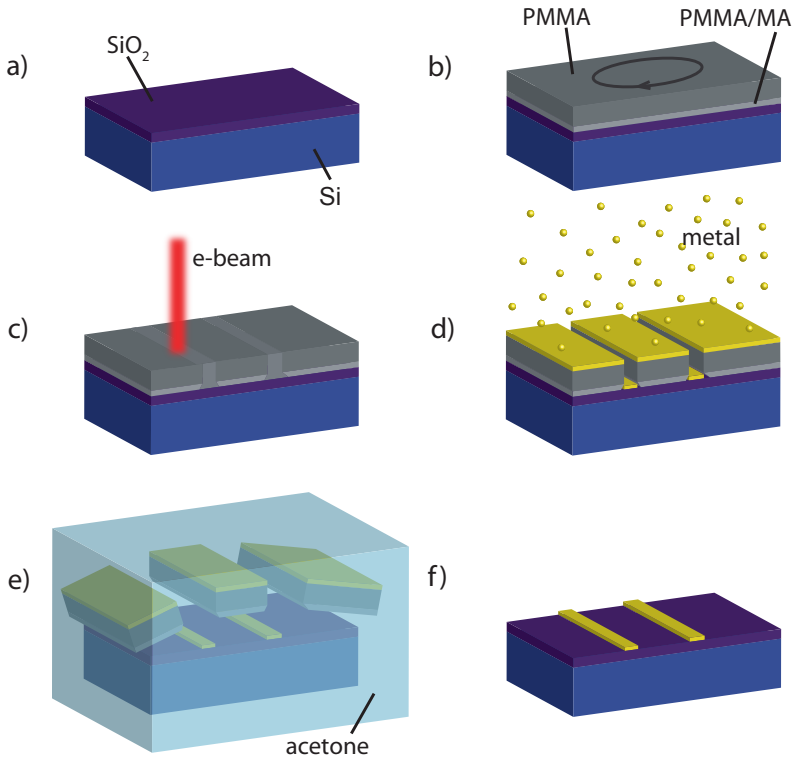
Figure 2.2: Schematic of the wafer processing. **a)** We start with a p-doped Si wafer with 400 nm SiO$_2$. **b)+c)** A PMMA/MA - PMMA double layer is spun on the wafer and then the polymer layer is structured with a scanning electron microscope. **d)** After the development process, a metal layer is evaporated on the whole surface in a ultra high vacuum evaporation system. **e)** In a lift-off process in acetone the unexposed PMMA layer is finally removed. **f)** The desired structure stays on the surface.

Contacting a CNT

This process is repeated several times: After CNT growth the alignment markers and bond pads are structured and metallized with 40 nm Au on top of 5 nm Ti. The Ti provides a good adhesion of the Au on the surface.

The wafer surface is then imaged with an SEM, using a low acceleration voltage of 1 kV and a 30 μm aperture, to locate suitable nanotubes. SEM imaging provides a fast and simple possibility for CNT localization but it

should be noted that the SEM is not imaging the geometrical contrast of the CNTs but the voltage contrast due to a different backscattering of the electrons in the area where the CNT is located [84]. The CNTs appear much larger than their actual geometrical size. To obtain information about the tube radius we are using an atomic force microscope (AFM). A disadvantage of the SEM is that observations can damage the nanotubes or generate carbonaceous coating [85]. To reduce SEM induced defects, we keep the exposure time of the CNTs as short as possible.

After localization the sample is covered with the polymer double layer again for further structuring. The alignment grid allows us to contact a CNT with an accuracy of < 10 nm. Before the ferromagnetic contacts are deposited, the sample is heated in the load-lock of the evaporation system with a heat lamp ($< 200°$C, 60 min.) to remove water in the contact area. Surface-bound water molecules close to the CNT can lead to contacting problems and charge traps responsible for instabilities found in electronic transport measurements [86].

After the deposition of 25 nm Permalloy, our material of choice for the FM contacts (see chapter 3), a third SEM structuring step is done for the leads connecting the FM contacts with the bond pads. To remove the oxidized layer on top of the FM contacts, we sputter the contact areas for 2
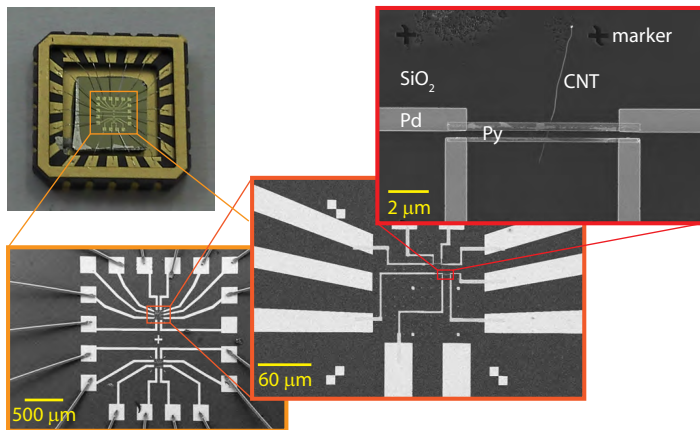

Figure 2.3: The image on the upper left shows a device glued in a chip carrier with an edge length of 8 mm. The Au pads on the device are bonded to the contact pads of the carrier by Al wires. In the zoom-ins shown in the lower SEM images one can see how a CNT is contacted with Py strips.

minutes with an Ar sputter gun (in the load-lock of the evaporation system, details can be found in appendix A). Then 50 nm Pd is deposited connecting the Permalloy strips with the bonding pads. (In some devices the Pd is evaporated in the second step and the FM material in the last step)

The finished device is cut to a size of 5 x 5 mm^2 and glued into a chip carrier with silver paint. The gluing with the conducting paint allows to electronically connect a cleaved edge of the Si wafer which provides a back-gate.

A complete device is depicted in fig. 2.3. The optical image in the upper left corner shows a wafer piece glued into a chip carrier. 18 Au bond pads are bonded with a 32 μm thick Al wire to the chip carrier. The zoom-ins show SEM images of the device. The bond pads provide contacts to 2 marker fields on the wafer (yellow rectangular). In the orange rectangular, one marker field is shown in detail. Inside the red rectangular a 6 μm long CNT can be seen that is contacted by two Py electrodes. Both electrodes are contacted from both sides with non-magnetic Pd to be able to measure a magnetoresistance signal through the FM strip (see chapter 3).

Double layer e-beam resist

The above introduced resist double layer is used to obtain good metal lift-off. When only PMMA is used as a resist it is sometimes problematic to remove the metal layer completely from the wafer surface and, especially in small structures, the edges are sometimes not well defined.

In fig. 2.4a two alignment markers written with the same parameters are compared. The marker in the upper SEM image is fabricated using a single PMMA layer, whereas a PMMA/MA-PMMA double layer is used for the marker in the lower image. The edges of the marker fabricated with the double polymer layer are much better resolved.

The PMMA/MA layer below gives a deeper undercut with the same writing parameters due to the shorter polymer chain length and can easier be desolved in the developing step. In fig. 2.4b we show a cross section of a wafer covered with the PMMA/MA-PMMA double layer. A 500 nm wide line has been written with an electron beam and metalized with Permalloy (Py) after development. The wafer has then been dipped into liquid nitrogen and was cleaved subsequent with the polymer layer on top. This allows to obtain a sharp breaking edge without a deformation of the polymer during the cleavage. The white dotted line marks the threshold between the two polymer layers. In the zoom-in in the right image an undercut of ∼100 nm on each side of the 500 nm wide strip is visible in the PMMA/MA layer.
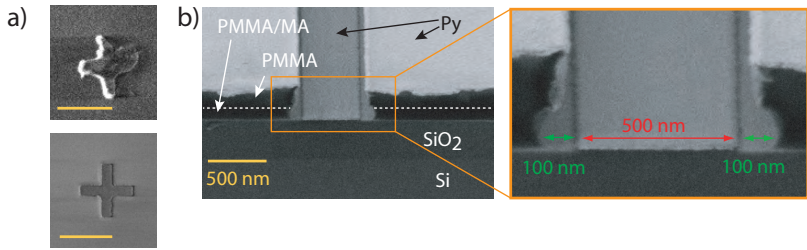
Figure 2.4: a) SEM images of an alignment marker structured with a PMMA layer (upper image) and a PMMA/MA-PMMA double layer (lower image). The edges of the marker structured with the polymer double layer are better defined. The scale bars have a length of 1 μm. **b)** SEM image of a 500 nm wide line written in a PMMA/MA-PMMA double layer after developing and metal deposition. The right image shows a zoom-in of the image on the left. A clear undercut of around 100 nm on each side of the metal strip can be seen in the PMMA/MA layer.

2.4 Improving the electrical contact to CNTs

Contacting carbon nanotubes with metallic contacts is a rather complex subject. It is theoretically predicted that the charge transport in a CNT can be controlled by Schottky barriers forming at the interfaces between the CNT and the metallic contacts and the device characteristics are strongly influenced by the work function of the metal contact [87]. It was also shown on basis of calculations that the numbers of chemical bonds (the wetting of the material) and the height of the Schottky barrier are related [88]. The models show that Pd provides chemical bonds to the delocalized π-like system of the CNT and therefore shows a good wetting of the CNT. Furthermore, the work function of Pd matches very well the work function of the CNT [89]. The good electrical contacts of Pd to CNTs has also been demonstated experimentally [90]. However, the states of these two models do not apply to all metals.

Residuing polymer layers

Great effort has already been undertaken by different research groups to experimentally investigate the electrical contact to CNTs of both non-magnetic [90] and ferromagnetic metals [91]. In chapter 3 we study the contact characteristics of several metals to CNTs. It was found that the ferromagnetic Permalloy (with a work function comparable to Pd [92]) made low ohmic electrical contact to CNTs in the first two batches of samples. However, the low contact resistances could not be reproduced in later devices.
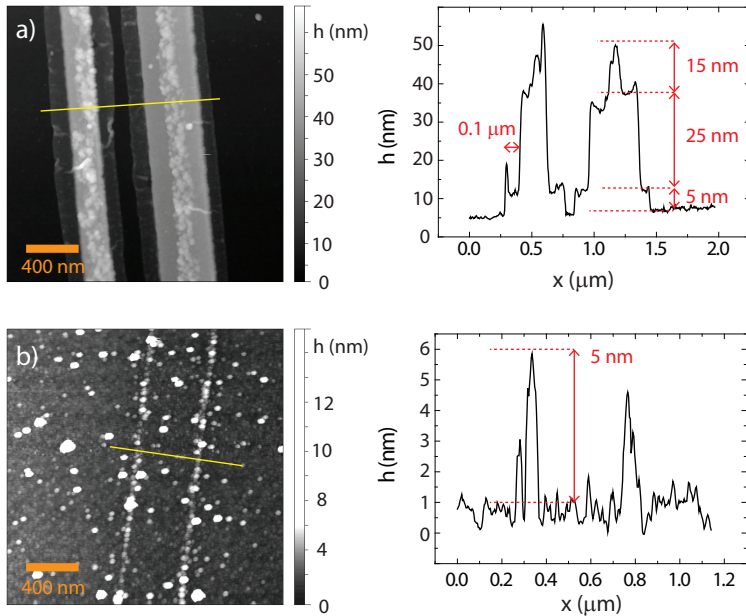
Figure 2.5: a) AFM image of two 25 nm high Py strip showing residues on both sides close to the contacts. These residues are not conducting and cannot be removed in standard RIE processes. On the right side the corresponding line graph is shown. Close to the contacts steps of ~ 5 nm are visible. On top ~ 15 nm high steps are found. **b)** Also in areas where the PMMA has been structured and developed but not metalized before the lift-off process polymer residues with a typical height of 5 nm are found.

By investigating our Permalloy contacts with AFM and SEM we found large scale residues close to the contact. In fig. 2.5a an AFM image of two 200 nm and 400 nm wide Permalloy strips is shown. The thickness of the deposited material is 25 nm. Residues on both sides of and most likely below the metal strips can clearly be seen. A line cut, indicated by the yellow line, is shown on the right. Steps of ~ 5 nm height close to the contacts are visible. It seems that the 25 nm thick metal strips are positioned on plateaus. On top, 15 nm high steps are visible. We found that the residues close to the contacts are not conducting and cannot be removed in the standard RIE process used for wafer cleaning. The residuing layers close to the contacts are also visible by SEM imaging with a good contrast (see appendix B). We find that the residues are independent of the used area exposure dose,

still visible for very high and very low doses. The AFM image in fig. 2.5b shows an e-beam structured and developed region where no metal has been deposited before the lift-off process was done. PMMA residues of $\sim 5\,\text{nm}$ height are visible, clearly showing the outline of the proposed strip shape.

In the literature, several studies report a residual resist polymer layer of 2-5 nm that stays on the surface after the development process [93, 94, 95, 96]. We think that PMMA residues that are not removed completely in the development process, are metallized with Permalloy during the evaporation process and oxidize when exposed to air later. For other evaporated metals we do not see such features which is probably due to a higher diffusion of Permalloy on the surface. A polymer layer in between the CNT and the metallic contact will lead to very high and unreliable contact resistances. The standard procedure in literature to remove the residuing polymer layer is an oxygen plasma cleaning [94], however this process is not possible for us because it damages or removes our nanotubes.

To reduce the resist residues we studied the effect of different baking times and temperatures on the hot plate, and additional treatments of the PMMA layer like UVO or RIE treatments before metal evaporation. Details of the studies and the corresponding SEM images can be found in appendix B. The results are that neither the baking temperature nor the baking time have a significant influence on the polymer residues or the electrical contact. By changing the baking procedure it is not possible to dispose of the residuing layer. A different approach to solve the residue problem is presented below.

Electrical stability of the devices

Another problem with a probably related cause is the electrical stability of the fabricated devices. The electrical stability can be influenced by charge rearrangements in the electrical device due to trapped charges in the SiO_2 layer, at the SiO_2/Si interface [97] or in water molecules bound to the nanotube [86]. We found an indication of remaining resist when we investigated our CNTs after a structuring process that can perhaps also lead to trapped charges close to the device. Fig. 2.6a shows an SEM image of a CNT after evaporation of the alignment markers. Irregularities on the nanotube with a typical diameter of 30 nm and separated by $\sim 200\,\text{nm}$ are visible. The image on the right shows a part of the CNT imaged with a higher resolution. The residues can also be seen by AFM imaging. Fig. 2.6b provides a comparison of residues on two crossed CNTs imaged with AFM (left image) and SEM (right image). The residues are visible in both images. We think that these residues are polymer clumps sticking to the nanotubes that are not resolved in acetone.

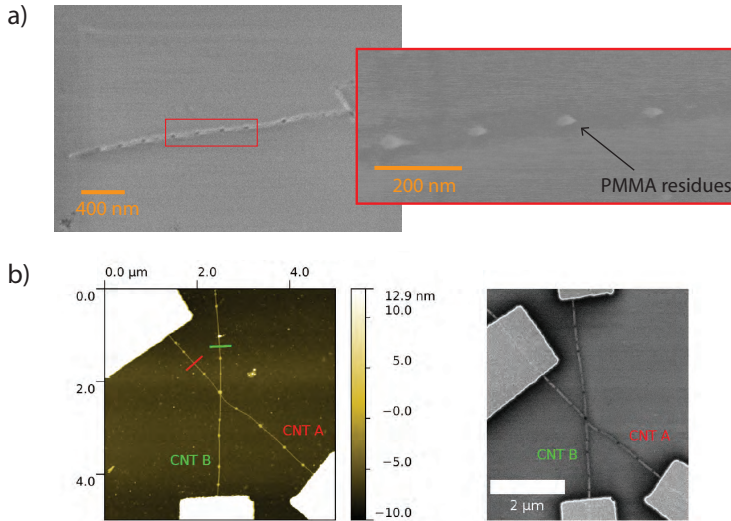The only definite way to avoid this kind of contamination is to grow the

Figure 2.6: a) SEM image of a CNT after the alignment marker processing step. It seems that polymer residues remain after metal lift-off and can contaminate the nanotube. The image on the right is an SEM image taken with a higher resolution. **b)** The residues on a crossed CNT device are visible in AFM images (left side) and SEM images (right side). The images of the crossed CNT device are kindly provided by Andreas Wepf.

CNTs in the last step on the prefabricated contacts. With this fabrication process, ultraclean nanotube devices can be obtained [83, 98]. However, for our devices we need narrow ferromagnetic contacts with well defined dimensions (see chapter 3) and melting or deformation of the metals on the wafer surface when heated to CNT growth temperatures of over $900°C$ can be problematic. Additionally, the fabrication of multiterminal structures requires considerable more effort because CNTs have to bridge several contacts by accidentally falling in the right orientation.

To solve the problem of the remaining polymer residues we started to take another approach in sample fabrication. After the CVD growth of the nanotubes we deposit $5\,nm$ Al_2O_3 on the wafer surface by atomic layer deposition (ALD) in an accurately controlled process. Thereby it is crucial that the deposited layer is homogeneous. After the deposition, the sample is covered with PMMA and alignment markes are structured and metallized. We found that CNTs can still be located below a thin layer of Al_2O_3. Before

the contacts to the CNT are metallized the sample is dipped for 30 seconds into 25 % *tetramethylammonium hydroxide* (TMAH) dissolved in water ($T = 50°C$). TMAH is a strong base generally used for Al, Al_2O_3 or Si etching [99]. The etching removes the oxide from the contact layer but does not affect the nanotube itself or the surrounding PMMA. The process is stopped in H_2O. Cleaning the sample in the UVO system before the TMAH etching helps to improve the removal of the oxide. With this additional fabrication step it is possible to deposit metallic contacts on CNTs without ever bringing them in contact with resist. Additional information to the process is provided in appendix B.

2.5 Measurement set-up

We first test the sample at room temperature with a needle prober or in a dipstick with a sample test box. An AC voltage of 1 mV is applied between the two contacts and the current through the device is measured with a lock-in amplifier[5]. This allows for a quick functionality test of the device and yields information about the contact resistances and a metallic or semi-conducting behavior of the CNT. When the CNT device is conducting it is transfered to a cryostat and cooled down.

Resolving the single electron levels of a quantum dot is not possible at room temperature. Measurements of single energy levels in a quantum dot require cryogenic temperatures and a good filtering of the electrical leads to minimize high frequency noise and heating effects. In the cryostats RLC low pass filters (tape worm filters) made of twisted Isotan (CuNi) wires wrapped in a Cu band are used for filtering (attenuation: 60 dB at 1 GHz, dc resistance 64 Ω [100]). They are built by the in-house electronics workshop of the University of Basel. At room temperature low-pass π-filters are used to filter out high frequency noise (attenuation: 40-60 dB for frequencies higher than 0.3 MHz [101]).

A schematic of the measurement set-up can be seen in fig 2.7. For conductance measurements an AC signal V_{AC} with a frequency of 77.77 Hz is generated by a lock-in amplifier. This AC signal is superimposed on a DC bias voltage V_{SD} by a transformer (transformation ratio 4:1). Often, the DC signal is generated with a DC auxiliary output of the lock-in amplifier. A voltage divider scales resulting voltage down by a factor 1000. At 230 mK, a typical voltage applied to the device is $V_{AC} = 10$ μV. This is low enough to prevent thermal broadening of the energy levels in the dot ($eV_{AC} < k_B T \approx 20 \, \mu eV$). The current in the device is converted to a voltage

---

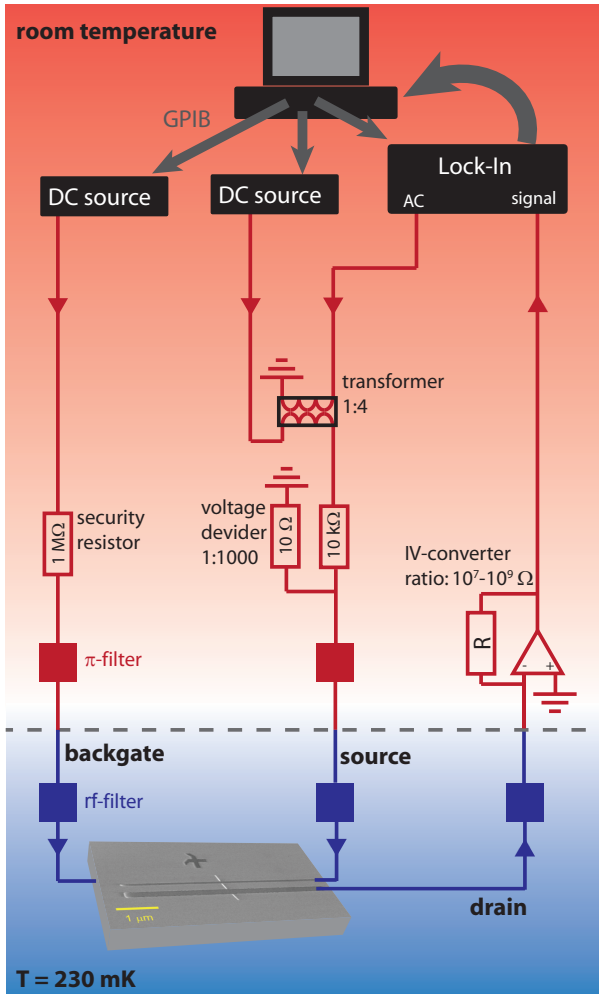[5]Stanford Research Systems SR 830 DSP

Figure 2.7: Schematic drawing of a typical measurement setup.

by an I/V converter with a conversion ratio of $10^7 - 10^9\,\Omega$. This voltage is then detected with the lock-in amplifier.

The backgate voltage V_{BG}, used to tune the energy levels of the QD, is

generated with an external voltage source[6]. A resistor in the current path is used to prevent high currents on the device in case of backgate leakage. All instruments are controlled via GPIB by LabVIEW programs[7].

2.6 Cryogenics

In this thesis mainly two cryostats are used. A schematic of a ^{4}He cryostat is shown in figure 2.8a. The variable temperature insert (VTI) allows fast device measurements and continuous runs up to 300 K. The sample in kept in a vacuum chamber dipped into liquid Helium ($T_{He} = 4.2$ K, drawn in light blue). Through a needle valve, He is sucked into the insert lowering the temperature inside further due to evaporation cooling. The lowest stable temperature we reach with this system is around 1.7 K. The He storage is shielded from the warmer environment by the inner vacuum chamber (IVC). The vacuum minimizes thermal coupling to the outer parts of the cryostat. To minimize heating by radiation a metal shield cooled by liquid

---

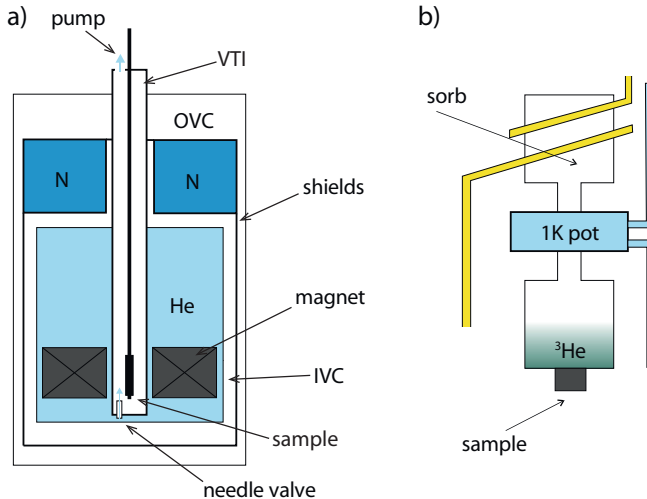[6]Yokogawa YK 7651
[7]LabVIEW 6.1 by National Instruments

Figure 2.8: a) Schematics of a ^{4}He cryostat. In the VTI ^{4}He is evaporated through a needle valve to reach temperatures of around 1.7 K. **b)** Working principle of a ^{3}He cryostat. ^{3}He is evaporated in a close circuit to reach temperatures down to 230 mK.

nitrogen (dark blue) surrounds the He storage. The nitrogen shield is thermally decoupled from the outside by an outer vacuum chamber (OVC). A superconducting magnet in the He bath allows the application of magnetic fields up to 8 T.

If temperatures below 1 K are needed a ^{3}He cryostat is used. The basic working principle is shown in figure 2.8b. ^{3}He is a helium isotope with a higher vapor pressure than ^{4}He [102]. Therefore, the cooling power of ^{3}He is higher at low temperatures. However, ^{3}He does not occur in nature in large quantities and is rather expensive. It is usually stored only in small quantities. A closed ^{3}He cycle shielded by a ^{4}He bath is used to reach temperatures around 230 mK. Liquid ^{3}He is evaporated in a chamber in thermal contact with the sample and collected in a charcoal sorbtion pump (sorb). In order to condense the ^{3}He, the sorb has to be heated to 30 K to release the ^{3}He gas (heating lines are drawn in yellow). The ^{3}He gas then condenses in the 1K pot ($T = 1.5$ K), cooled by controlled evaporation of ^{4}He and collects again in the chamber above the sample. The cooling to very low temperatures is thus limited to a few days before all ^{3}He is evaporated and the cycle has to be restarted by heating the sorb. The ^{3}He cryostat contains a superconducting magnet with a maximum field of 8 T.

Chapter 3

Ferromagnetic Materials for Carbon Nanotube Spintronic Devices

Considerable effort is dedicated to use carbon nanotubes for spintronic applications [19, 62, 103, 104]. In CNT devices a ferromagnetic metal, like NiPd [19, 104], Co [18, 54] or various others [105, 106, 107] is used to inject a spin polarized current into the CNT. However, for many materials the local magnetization at the contact area and the contact resistance to carbon nanostructures were found to be of poor reproducibility. Some also develop an out-of-plane magnetization and multidomain structures, leading to large stray fields at the devices and unreliable MR behavior. For this reason, one of the main goals of this thesis was to find an FM material that fulfills the desired requirements and to optimize the relevant properties. Ideally, the following requirements have to be met by the ferromagnetic material in a CNT spin-valve:

1. *A large spin polarization*: to obtain a large spin signal

2. *The shape anisotropy dominates the crystal anisotropy*: to allow tuning of the switching fields by the contact geometry.

3. *A single magnetic domain covering each contact area*: to avoid the compensation of the spin injection by neighboring domains. In the ideal case the whole contact consist of a single domain which allows to relate directly the MR signal with the magnetization reversal of the contact observed in AMR signals of individual strips.

4. *In-plane magnetization*: to reduce stray fields on the CNT.

5. *Reproducible electronic coupling to the medium between the contacts*:
   to allow reproducible fabrication of devices and high yields.

In this thesis, a series of materials were considered and tested. We present
in this chapter the results on different ferromagnetic materials and discuss
their properties with respect to the above points. We demonstrate that
Permalloy (Py), a widely used Ni/Fe alloy, meets the requirements for the
injection and detection of spin polarized currents in carbon nanotube spin-
tronic devices. We establish the material quality and magnetization proper-
ties of Py strips in the shape of suitable electrical contacts and find a sharp
magnetization switching tunable by geometry in the anisotropic magnetore-
sistance of a single strip at cryogenic temperatures. In addition, we show
that Py contacts couple strongly to CNTs, thereby forming quantum dots
at low temperatures[1].

The FM contacts studied in this thesis are cuboids with a typical length
of $10 - 17\,\mu$m. They are contacted with Pd leads for electrical transport
measurements. This is in contrast to structures completely fabricated of an
FM material (like e.g. [109]) and minimizes stray fields on the device. The
elongated shape allows to minimize stray field effects on the CNT due to
the end domains of the contacts.

3.1 Methods of investigation

To investigate the magnetic properties of the tested materials, different
methods were used. The *vibrating sample magnetometer* (VSM) allows for
a quick quality check of the evaporated material at room temperature. For
studies of the magnetic behavior of individual FM strips we make use of
anisotropic magnetoresistance (AMR) measurements at low temperatures.

3.1.1 Vibrating sample magnetometer

The quality of an evaporated ferromagnetic thin film can be tested with
a VSM. The wafer with the FM film is placed inside a uniform magnetic
field ($H_{\max} = 2\,$T in our system[2]) as shown in fig 3.1a. This leads to a
magnetization of the FM material. The sample is then vibrated sinusoidally
up and down, leading to a sinusoidal variation of the magnetic flux through
several nearby pickup coils. The variation of the flux induces a voltage in
the coils, proportional to the magnetic moment of the sample [110]. The

---

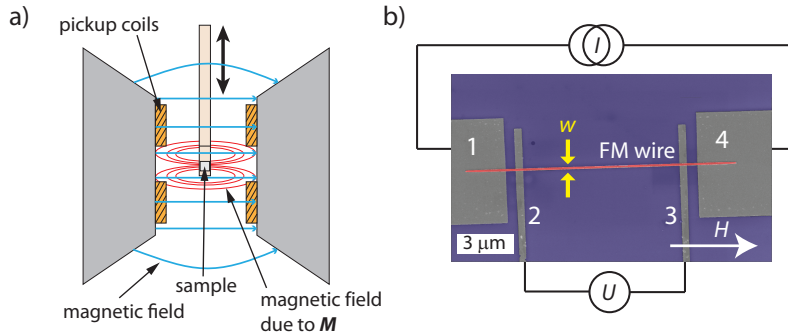[1]Parts of this work have been published in [108]
[2]LakeShore VSM 4700

Figure 3.1: a) Schematic of a VSM. The sample is vibrated sinusoidally in a uniform magnetic field. The variation in magnetic flux is detected by pickup coils. **b)** False-color SEM image of an FM strip with width w contacted in a 4-terminal geometry for AMR measurements.

comparison of the measured saturation magnetization and the coercive field of the thin film can then be compared to literature values.

We also use the VSM to gain information about the magnetization and the switching fields of fabricated contacts. However, the magnetic moment of a single 300 nm wide strip is $\sim 6 \cdot 10^{-5}\,\mu$emu, far below the sensitivity of the system (noise floor $0.1\,\mu$emu). We therefore investigate strip grids with $\sim$170,000 parallel strips with a total magnetic moments of $\sim 10\,\mu$emu. We vary the number of investigated strips in these strip grids for different width w to keep the total volume of material constant. One has to keep in mind that the signal can differ from the signal of an individual contact due to FM stray field interactions between the strips and other effect (see below).

3.1.2 Anisotropic magnetoresistance

Due to spin-orbit interactions, the electrical resistance in a ferromagnetic metal depends on the relative orientation of the magnetization and the current direction (see chapter 1). We use the AMR to investigate an individual contact strip in a four-terminal geometry at low temperatures. In this geometry, the device resistance is measured without the additional components of the cable resistances, the lead resistances and the contact resistances. A false-color SEM image of a typical device can be seen in fig. 3.1b. A 12 μm long FM strip of width w (red) is contacted with four Pd contacts (gray). A current is injected from contact 1 to 4 and the voltage drop over the contacts 2 and 3 is measured. At the same time an external magnetic field, applied

along the long axis of the strip, is swept from large negative to large positive values and back.

The magnetization of a small ellipsoidal shaped FM is well-described by the *Stoner-Wohlfarth model* for the coherent rotation of a single macroscopic magnetic moment with the anisotropy energy as a fit parameter. If we assume that our FM contacts consist only of a single magnetic domain, the model should also apply to the measured AMR signals.

As described in the chapter 1 the total energy per unit volume of a material with magnetization $\boldsymbol{M}$ in an external magnetic field $\boldsymbol{H}$ can be written as the sum of the anisotropy energy density E_A and the Zeeman energy per unit volume E_Z:

$$E = E_A + E_Z = K\sin^2(\theta) - \mu_0 H M_S \cos(\theta - \alpha) \tag{3.1}$$

where α and θ are the angles between the long axis of the strip and the external field and the magnetization, respectively (see schematic in chapter 1). From a numerical minimization of this function we obtain the angle θ with minimal energy for each H-value. The anisotropic magnetoresistance is then found as

$$R = R_\perp + \Delta R\,\cos^2(\theta). \tag{3.2}$$

$\Delta R = R_\parallel - R_\perp$ denotes the difference in resistance of the device with a magnetization parallel ($R_\parallel$) and perpendicular ($R_\perp$) to the current.

For ferromagnetic electrodes with the easy axis aligned parallel to the external field ($\alpha = 0$), the ideal magnetization dynamics is a sharp switching

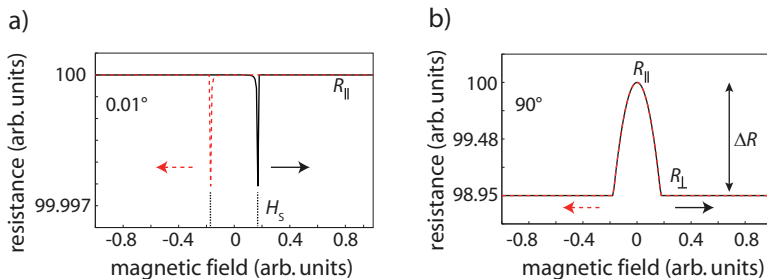**Figure 3.2:** For an ellipsoidal shaped single domain particle, the AMR can be calculated by the Stoner-Wohlfarth model. **a)** For a perfect parallel alignment of the particle with the external magnetic field, no change in resistance will be visible. A slight misalignment (here $\alpha = 0.01°$) allows one to detect the switching. **b)** The maximal change in resistance can be measured for $\alpha = 90°$.

by $180°$ at the switching field H_S without prior rotation and formation of multiple domains when the magnetic field is reversed. In this case no variation of the AMR is expected. A detectable signal can be achieved in this configuration with a slight misalignment ($\leq 2°$), as shown in the example in fig. 3.2a for $\alpha = 0.01°$. One finds a clear discontinuous change in the resistance and a very sharp switching.

The maximal change in resistance ΔR can be obtained by applying the field perpendicular to the electrode ($\alpha = 90°$). An example of the expected curve for an ellipsoidal shaped single domain particle is shown in fig. 3.2b.

The AMR studies allow to study the magnetization reversal of a contact and to draw conclusion about possible multiple domains.

3.2 Ferromagnetic Materials

We first discuss the suitability of the 3d transition metals Ni, Co and Fe as contact materials for CNTs. Then we present our results on the FM alloys PdNi, PdFe and NiFe. Extensive results are only shown on the latter material.

3.2.1 Ni

Due to its good contact properties to CNTs, the soft ferromagnet Ni is used in different groups for spin transport experiments in nanotubes [11, 111]. The crystal anisotropy is small compared to the shape anisotropy ($4 \cdot 10^{-3}$ J/cm^3 and $7 \cdot 10^{-2}$ J/cm^3, respectively [112]) and the easy magnetization axis of cylindrical wires is well aligned with their long axis up to a wire diameter of 60 nm [112]. For thicker diameters the easy axis has a component pointing out of the wire and the magnetization reversal is accompanied by a curled domains formation. The average domain size for a 45 nm thin Ni film is ~ 275 nm with domain walls between 20 and 60 nm width [113]. The values determined for thin films are smaller than for single crystal bulk materials due to the additional component of a surface magnetocrystalline anisotropy. The domain size is scaling with the square root of the film thickness.

To study the magnetic behavior of individual Ni strips in external magnetic fields, we investigated the 4-terminal AMR of several 50 nm thick strips at 1.6 K. Fig. 3.3a shows the resistance of a 1500 μm long and 100 μm wide, thermally evaporated Ni strip in an external magnetic field applied parallel to the strip axis. A gradually decrease in resistance is investigated for a decreasing magnetic field, starting at $+0.2$ T. A similar behavior is found for the up-sweep of the field. Sharp switching features are not observed. A gradually changing resistance can also be seen in fig. 3.3b for a 15 μm
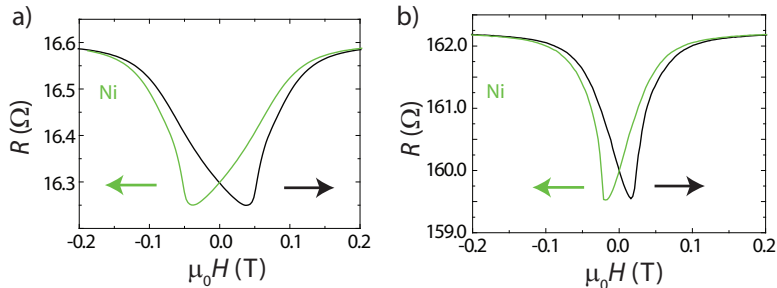
Figure 3.3: a) 4-terminal AMR signal of a 50 nm thick Ni strip with a lenght of $l = 1500\,\mu m$ and a width of $100\,\mu m$ in an external magnetic field applied along the long axis of the strip. No sharp switching features are visible, only a gradual change in resistance with the external magnetic field. **b)** The AMR of a 100 nm wide Ni strip ($d = 50\,nm$, $l = 15\,\mu m$) shows the same characteristic behavior as the bigger strip shown in a).

long and 100 nm wide electrode with the same film thickness in a parallel magnetic field. We assume that this gradual change in the AMR, that already starts before the external magnetic field reaches zero, goes back to a formation of multiple domains in the Ni strip and an easy axis not well aligned with the long axis of the strip, in agreement with results for the cylindrical geometries [112]. This not well defined switching behavior makes Ni contacts not useful for our purpose.

3.2.2 Co

In Co nanowires the magnetocrystalline anisotropy is roughly the same size as the shape anisotropy ($4.5 \cdot 10^{-1}\,\mathrm{J/cm^3}$ and $6 \cdot 10^{-1}\,\mathrm{J/cm^3}$, respectively [112]). However, for nanowires with diameters smaller than 40 nm a single domain state with an easy axis along the nanowire long axis is observed [112, 114]. The domain size in 50 nm thick films is around 100 nm, almost three times smaller than for Ni [112].

Block-shaped strips made of Co are used by different groups for spin transport experiments [18, 54, 103, 115]. The magnetization in these strips shows sharp switching features and the switching field can be tuned by the width of the strips.

AMR measurements of 35 nm thick Co strips can be seen in fig. 3.4. The geometries of the strips are comparable to the Ni strips discussed above (fig. 3.4a 1500 μm x 100 μm, fig. 3.4b 15 μm x 100 nm). The large Co strip shows a much sharper resistance change with less rotation compared to the
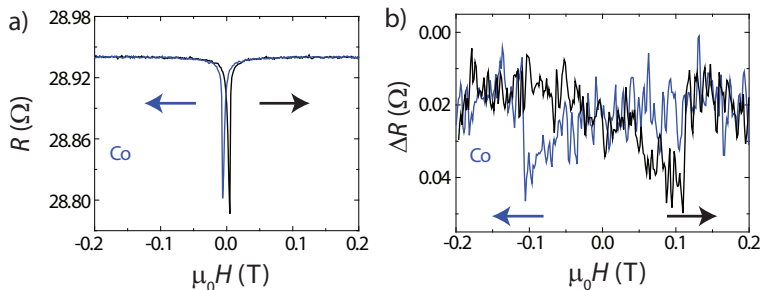
Figure 3.4: a) 4-terminal AMR signal of a 35 nm thick Co strip with a length of 1500 μm and a width of 100 μm. **b)** 2-terminal AMR signal of a 100 nm wide Ni strip with a length of 15 μm and 35 nm thickness. Sharp switching features are visible as required.

Ni strip of similar dimensions. This becomes even more pronounced for the narrow strip. The (2-terminal) AMR of the narrow strip shows the desired behavior: a slight decrease in resistance before a sharp switching feature is visible. However, the contact properties of Co to CNTs are found to be rather poor. Contacting CNTs is not very reproducible and the contacts were found to freeze out at low temperatures [116].

3.2.3 Fe

Only few magnetotransport experiments have been done with Fe contacts (e.g. [105]). Fe is believed to suffer from a high oxidation rate and was expected to give poor results. To confirm this, we first evaporated Fe films on wafers to study their oxidation behavior with X-ray photoelectron spectroscopy (XPS). 3 pieces of Si wafer were etched in hydrofluoric (HF) acid (40 %, 4 min.) to remove the silicon oxide layer on the surface. This was done to make sure that an oxygen signal measured by XPS cannot be due to the SiO_2 layer. After etching, the wafer pieces were immediately mounted in the evaporation system for metal deposition, where 40 nm Fe were deposited.

The first piece was brought directly from the evaporation system to the XPS system and mounted in the vacuum chamber. It has been exposed to air for around 2 minutes. In a first scan we found O, N and C on the surface. We also found the Fe $2p_{3/2}$ peak shifted to iron oxide position at around 711.0 eV [117]. After 5 minutes Ar sputtering of the sample (2.5 kV, $7 \cdot 10^{-5}$ mbar) we have not seen N and C anymore. Some small amount of O could still be found. However, the Fe $2p_{3/2}$ peak was now found at
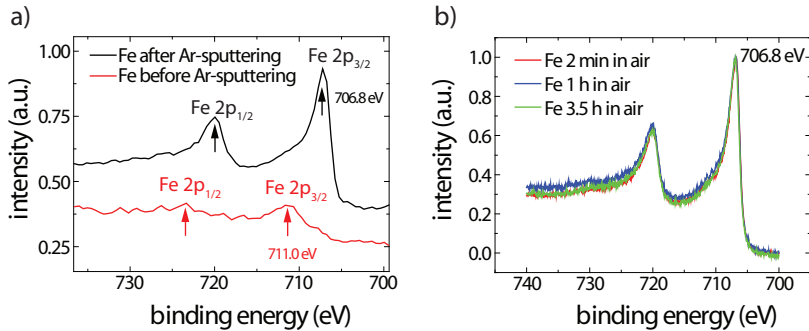
Figure 3.5: a) XPS measurement on an Fe film that has been exposed to air for around 2 minutes (red line). The peaks for pure Fe are shifted to the Fe oxide position. After Ar sputtering the pure Fe peaks are found again (black line). **b)** Photoelectron signal intensity of three Fe films oxidized for 2 min, 1 h and 3.5 h in air after 5 min of Ar sputtering. Pure Fe is found below an oxidized layer independent on the oxidation time.

its elementary position (706.8 eV) as can be seen in fig. 3.5a. The second and third sample have been oxidized in air for 1 h and 3.5 h, respectively. For both we saw an Fe oxide peak before sputtering and the elementary Fe peak after sputtering for 5 minutes. The Fe peak position for the different samples are shown in fig. 3.5b. The longer oxidation time does not lead to a change in the photoelectron signal intensity of the three samples. A longer sputtering (10 minutes) does not change the result. The sputtering rate for Fe was determined at the edge of the sample to be 1 nm per minute. We conclude from these experiments that the Fe film is not oxidized completely. It oxidizes fast on its surface when exposed to air. However, after removing of 5-10 nm of the top layer we see essentially pure iron.

For a first study of the magnetic properties of our Fe films we did a room temperature vibrating sample magnetometer (VSM) characterization at the *Institut für Physik* in Karlsruhe[3]. Several 40 nm thick Fe films have been exposed to air for around 4 h. A VSM magnetization measurement of a film is plotted in red in fig. 3.6a. The saturation magnetizations of the films was found $\sim 1750\,(\pm100)\,\text{emu/cm}^3$ when we assume that 5 nm Fe on the surface are oxidized and do not contribute to the total magnetization. This value is in good agreement with the value for bulk Fe (1714 emu/cm^3 [20]). The Fe layer shows a sharp change in magnetization at the coercive field field of 8 mT. The additional step that is visible between 8 and 30 mT can be traced to a diagonally cut edge (see schematic in the inset) that
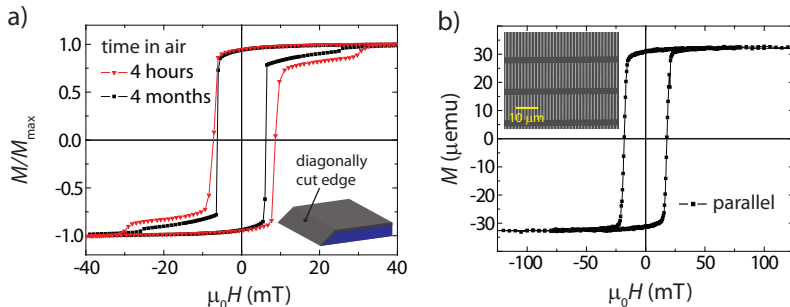
---

[3]collaboration with Dr. C. Sürgers

Figure 3.6: a) The red line shows a VSM magnetization measurement of a 40 nm thick Fe film after 4 h of oxidation in air. The black line shows the same measurement around 4 months later on a different VSM system. The step in the curves go back to a diagonally cut edge of the wafer that has also been metalized (see inset). The total magnetization was lower, but a complete oxidation on the timescale of a few months is not visible. **b)** VSM measurements of a grid of Fe strips with 500 nm width. The magnetization curve shows a well defined rectangular hysteresis. The inset shows an SEM image of a part of the grid.

has also been metalized in the evaporation process and shows a different magnetization behavior than the flat film. The clear hysteretic behavior and the expected saturation magnetization confirm the finding above that the film is not oxidized completely when exposed to air.

The same film has been measured after ~ 4 months in air on our own VSM system (black curve in fig. 3.6a). The measured magnetization was lower than what we obtained 4 months earlier. However, if we assume an unoxidized film of 27 nm, the saturation magnetization is found $\sim 1710 \, (\pm 100)$ emu/cm^3. The lower total magnetization that we measure could therefore be explained by a partial oxidation of the film. However, the coercive field of 6.5 mT is again comparable to the previous value and also the step due to the metallized edge can still be seen. These tests lead us again to the conclusion that our Fe films are oxidizing slowly in air on the surface with a rate of $\sim 3 - 4$ nm/month. Most importantly the magnetization is sufficient even after four months.

In a next step, we investigated the magnetic behavior of $\sim 100,000$ Fe strips with a width of 500 nm with the VSM (fig. 3.6b). A part of the strip grid is shown in the SEM image in the inset. We find a rectangular shaped hysteresis curve with a coercive field of 18 mT for a magnetic field applied parallel to the long axis of the strips. This indicates a well defined switching of the strips.

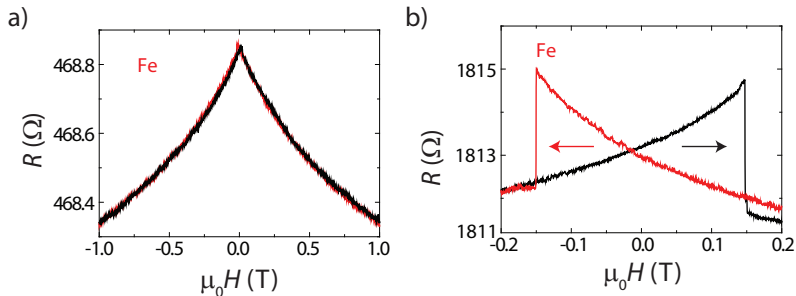For a more detailed investigation of the switching behavior, we studied

Figure 3.7: *a)* 4-terminal AMR of a 40 nm thick Fe contact ($w = 100\,\mathrm{nm}$, $l = 15\,\mu\mathrm{m}$). A large non-saturating background can be seen. **b)** 2-terminal AMR of a Pd capped 35 nm thick Fe strip with the same dimensions as in a).

the AMR signals of individual contacts at 1.6 K. Fig. 3.7a shows the four terminal resistance of a single 40 nm thick strip ($w = 100\,\mathrm{nm}$, $l = 15\,\mu\mathrm{m}$) in an external magnetic field applied parallel to the strip axis. A decreasing resistance for increasing magnetic field, starting at zero field, can be seen, not saturating even for magnetic fields larger than 1 T. For small magnetic fields a steplike change in resistance is observed. This feature is better visible in a second sample. Fig. 3.7b shows a measurement for a strip with the same dimensions but consisting of 35 nm Fe with a 5 nm Pd cap layer. The plotted graph is measured in a two-terminal measurement explaining the higher resistance. A steplike change in resistance is visible around $\pm 150\,\mathrm{mT}$. The observed large-field characteristics are not consistent with the Stoner Wohlfarth model and make an interpretation difficult. The easy axis of the strip seems not to be aligned with the long axis of the strip and is not rotated there for fields up to 1 T. Probably the system is dominated by several domains and magnetization directions. Another interpretation is that the iron forms a granular film on the surface. Spin-dependent tunneling between individual grains increases when the relative orientation between the grains become parallel [118]. This lowers the resistance for increasing magnetic field.

3.2.4 PdNi

Another possibility is to alloy the materials to get ferromagnets with different properties. Pd is known to make good and reproducible contact to CNTs [90]. A widely used material for CNT spin-valve devices are PdNi alloys [19, 104, 119]. $Pd_{30}Ni_{70}$ is a ferromagnetic alloy that has been used

by Sahoo *et al.* [19] to fabricate electrical field controlled CNT spin-valve devices. We also found good contacting properties of PdNi in several CNT test devices. However, studies of the magnetic properties of PdNi by G. Gunnarsson [116] showed that PdNi contacts form multidomain structures and the contact magnetization has a strong out-of-plane component. By magnetic force microscope (MFM) studies (fig. 3.8a), Feuillet-Palma *et al.* [104] found domains of a typical size of $1\,\mu$m in the contacts transverse to the wire axis. This domain formation was recently also confirmed by extensive studies with different magnetic imaging techniques [120]. The multiple transverse domains give rise to large stray fields perturbing spin-signals and the domain formation in the contact area can lead to an injection of opposed spin polarized currents.
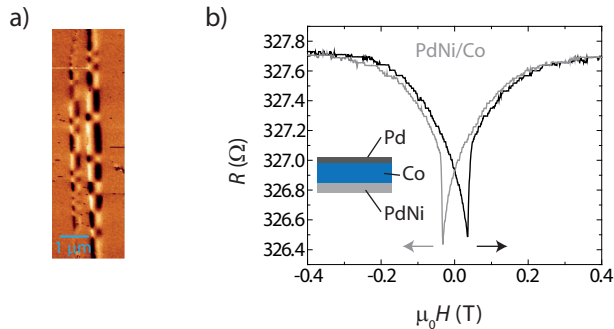
Figure 3.8: a) MFM image of two PdNi strips taken from [104]. Large transverse domains can be seen. **b)** AMR of a multilayer FM contact consisting of 40 nm Co on top of 25 nm PdNi capped with a 10 nm Pd layer. Sharp switching features can be seen, going back to a pinning of the PdNi easy axis in the strip plane by the Co.

3.2.5 PdNi/Co

We tried to pin the magnetization to the contact plane by evaporating a layer of Co on top of a $Pd_{30}Ni_{70}$ layer. An AMR signal of such a multilayer strip ($10\,\mu$m x $400\,$nm) with a magnetic field applied along the strip axis can be seen in fig. 3.8b. 40 nm Co have been evaporated on top of a 25 nm thick PdNi layer. This FM bilayer structure is capped by a 10 nm Pd layer to prevent oxidation. When the magnetic field is ramped down, starting at a high positive field, the measurement shows a gradual decrease of the strip resistance that starts before the external magnetic field reaches zero. Then,

a sharp switching feature, followed by an increase of the resistance back to the initial value, is visible.

The gradually changing resistance before the magnetic field reaches zero indicates a component of the magnetization not aligned along the long axis of the strip. It can only be rotated along the long strip axis for stronger magnetic fields. The fact that besides the sharp switching feature a gradually changing resistance is observed in the AMR makes this multi layer structure not useful for our devices. The PdNi layer, that is in contact with the CNT, seems not to follow the magnetization of the Co layer.

3.2.6 PdFe

We evaporated $Pd_{34}Fe_{66}$ thermally from two different sources in a *Bestec* evaporation system in ultra high vacuum (UHV) at a pressure $< 5 \cdot 10^{-10}$ mbar. The metal ratio was verified by X-ray photoelectron spectroscopy (XPS) and energy dispersive X-ray spectroscopy (EDX). These measurements also showed that the deposited material is an alloy and not a mixture of two metals.

The two materials are simultaneously evaporated from slightly different

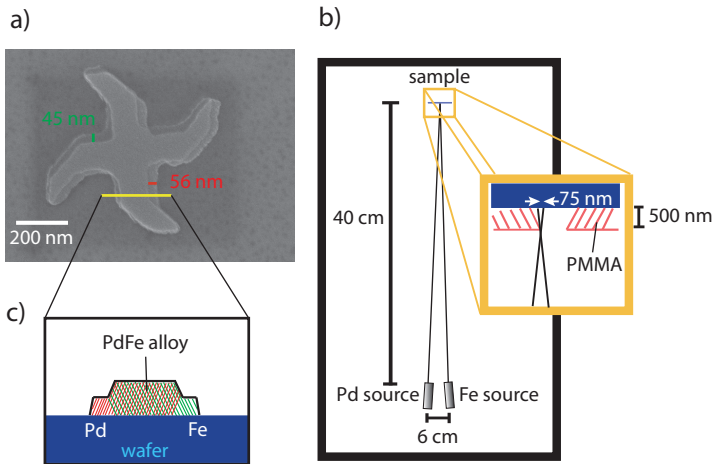**Figure 3.9: a)** SEM image of a marker made from PdFe. Double features at the edges due to the alloy evaporation from two different sources can be seen. **b)** Schematic of the evaporation chamber. A PMMA thickness of 500 nm leads to a shift in the edges of around 75 nm. **c)** The schematic of the cross section shows pure Pd and pure Fe on the edges of a structure. This can lead to instable electrical contact to CNTs.

angles and steps at the edges of the structure can be seen as indicated in the SEM image in fig. 3.9a. The red and green bar mark a shift of 56 nm and 45 nm, respectively. Fig. 3.9b shows a schematic of the two sources and the sample in the evaporation system. The evaporation of two materials from two different angles leads to regions where only one of the materials is deposited (see yellow rectangle). The maximal width of this region is estimated to be around 75 nm for a 500 nm PMMA layer. We can have on one side of the contact nearly pure Pd and on the other side pure Fe as shown in fig. 3.9c. The Pd makes good contact to the CNT whereas the Fe could oxidize and form insulating iron oxide. This might lead to a non-magnetic transport channel. Despite the good contact properties we found to CNTs, we decided to not investigate further this material.

3.2.7 NiFe (Permalloy)

The material of choice for us that fulfills all our requirements is Permalloy [108]. Permalloy (Py) is a ferromagnetic alloy containing 80 % Ni and 20 % Fe ($Ni_{80}Fe_{20}$)[4]. Py can exhibit a spin-polarization of up to 48 %[5], as large as Co or Fe [122]. In addition, it has a small crystal anisotropy and forms only few large domains in nanostructured thin films [91].

Permalloy is not a newly discovered material. It has been used for thin film storage elements over 40 years ago [123] and later also in read heads of computer hard disks [124]. The domain walls can even be controlled by current pulses potentially useful in racetrack memories [125].

We first describe a *three-step material characterization* using VSM and AMR characterization that allows a simple quality check of the material before we discuss the contact properties of Py in CNTs devices. Our Permalloy devices are evaporated by electron beam evaporation in a UHV *Bestec* evaporation system at a base pressure $p < 5 \cdot 10^{-10}$ mbar with a rate of 0.2 Å/s from a single target.

step I: material quality

The material quality is established by investigating a film of the required thickness in a VSM at room temperature. We find that Py films in the thickness range of 20 nm to 50 nm behave quantitatively like bulk material. The saturation magnetization of the films is ~ 800 emu/cm^3, in good agreement with literature [126]. A typical magnetization curve for a 25 nm thick

---

[4]These numbers are measured in atom percent. The notation for the ratio in volume percent is Ni81Fe19

[5]Measured by spin-polarized tunneling spectroscopy. Typical spin-polarizations found by point-contact Andreev reflection experiments are $34 - 45$ % [121].
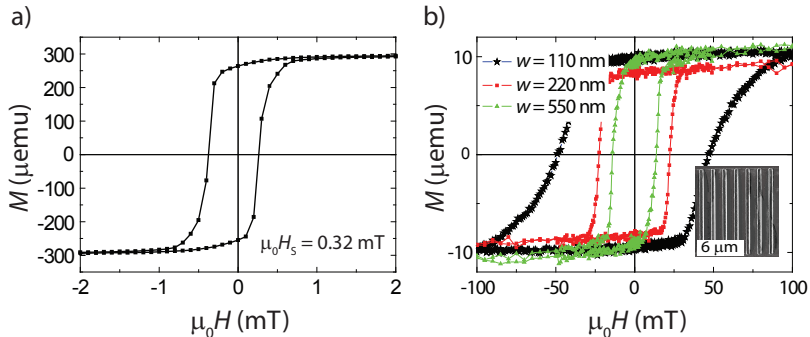
Figure 3.10: a) Step I: The magnetic moment M of a thin Py film measured in a VSM allows for a quick quality check of the FM material. **b) Step II:** The magnetization of several 100'000 Py strips in the shape of a single contact is investigated. Different switching fields can be seen for strips with different width.

Py film in an in-plane magnetic field is plotted in fig. 3.10a. The shape of the hysteresis curve is quite rectangular and the magnetization reversal takes place at $\sim 1\,\mathrm{mT}$. This indicates a well defined change in magnetization without stepwise domain rotation. The coercive field is very small ($< 0.5\,\mathrm{mT}$), making Py a widely spread material in the hard disk read head research, because it allows a switching of the magnetization state by only small external fields [127]. This test offers a quick and simple investigation of the material quality and can be done only with minimal preparation in the same evaporation step as the device fabrication.

step II: magnetic properties of contact strips

The VSM also offers a simple possibility to investigate the magnetization of the contacts. Because the magnetization of a single contact is too small to be detected by VSM, we investigate a grid containing several 100'000 strips, each with the geometry of a single contact (see above). We choose to keep the total deposited material the same for each test, which requires to adjust the number of strips in a grid for different strip widths w. This leads to similar total magnetizations. An SEM image of a part of such a sample is shown in the inset of fig. 3.10b. All contacts discussed here are 25 nm thick and between $10\,\mu\mathrm{m}$ and $17\,\mu\mathrm{m}$ long rectangles. Three magnetization curves with the external magnetic field H applied along the long strip axis are plotted in fig. 3.10b for strips of 110 nm, 220 nm and 550 nm width.

We find that narrow contacts result in a large coercive field. The de-

creasing coercive fields for wider strips are dictated by the shape anisotropy [128, 129, 130]. Except for the 110 nm strips, the magnetization reversal from 10 % to 90 % of the saturation values takes place on ~ 10 mT. We denote the field where the magnetization reaches 90 % as H_{90}. The different curve shapes and the wide transition found for the most narrow strip we tentatively attribute to stray-field interactions between the strips because the narrow strips are written closer nearby to reach the same area coverage as for the other devices. An additional effect leading to a broader range of magnetization reversal for the more narrow strips is the edge roughness with a magnitude of ~ 10 nm, due to the fabrication process or partial oxidation of the edges. This edge roughness becomes more important for decreasing strip widths and may serve as nucleation and pinning center for domains inside the strips, for example reducing the shape anisotropy [130]. The measured magnetization of the strips behaves bulk like, scaling with the material thickness (not shown). The saturation magnetization of ~ 740 emu/cm^3 is slightly lower than for the thin film, probably due to oxidation of the strips.

step III: magnetic properties of a single contact

We use the anisotropic magnetoresistance to investigate individual contact strips in a four-terminal geometry with normal metal contacts. The measurements are performed with an ac resistance bridge[6]. The resistivity of the strips at 4.2 K is 25 $\mu\Omega$cm (41 $\mu\Omega$cm at 300 K), which is higher than the bulk resistance value (16 $\mu\Omega$cm at 300 K [131]) but in good agreement with literature values for Py thin films (e.g. [132]).

In fig. 3.11a we plot the AMR of a single 25 nm thick and 100 nm wide strip as the normalized deviation from the zero-field value R_0 at a temperature of 4.2 K for an increasing magnetic field. The external magnetic field has been applied in the sample plane parallel (ip$_\parallel$) and perpendicular to the strip (ip$_\perp$), plotted in red and gray, respectively, and perpendicular to the strip orthogonal to the surface (oop$_\perp$) plotted in black.

While the AMR hardly changes for ip$_\parallel$, the curves recorded with the field perpendicular to the strip both show the characteristic shape of a continuous rotation of a magnetic moment with increasing field. The maximum signal change of $3\% - 4\%$ is consistent with bulk AMR measurements [48]. The data for the reversed sweep direction are omitted for clarity and coincide with the presented curves except for the small switching shown in the inset due to a small misalignment of the field with the strip axis. The switching occurs at the corresponding negative field in the downward sweep and is considerably smaller than the signal change due to the magnetization rotation. The
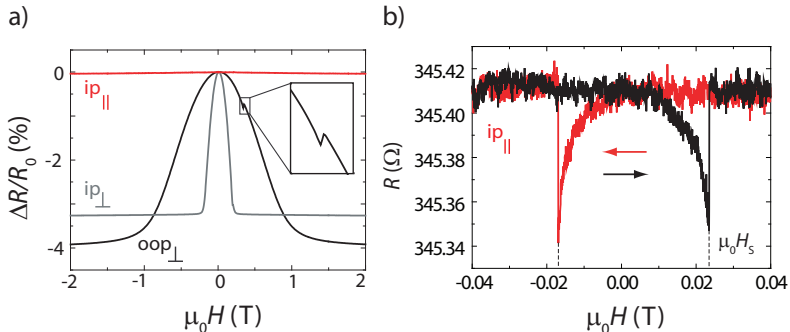
---

[6]Picowatt AVS-47

Figure 3.11: Step III: a) AMR of a 100 nm wide Py strip aligned parallel to an increasing external magnetic field (ip$_\parallel$), perpendicular to the field in the sample plane (ip$_\perp$) and perpendicular to it out-of the sample plane (oop$_\perp$). The structure on the perpendicular measurement (inset) is due to a small misalignment. **b)** AMR of a 500 nm wide Py strip at low magnetic fields. Sharp switching features are visible around 20 mT. The asymmetry is due to a small hysteresis of the superconducting magnet.

difference between ip$_\perp$ and oop$_\perp$ is probably due to the difference in the demagnetization factor and in the allowed domain structures in the two directions. A typical low-field AMR of a 500 nm wide strip in a parallel field can be seen in fig. 3.11b. The background signal is nearly flat, an evidence for a good alignment of the strip with the magnetic field. After a slight decrease of the resistance starting at zero magnetic field, sharp switching features around 20 mT can be seen. The asymmetry in switching is due to a small hysteresis in the superconducting magnet. The shape of the curve is simlar as expected for a single domain state.

The AMR of the Permalloy strips can be fitted with a Stoner-Wohlfarth based model (see above). The gray curves in fig. 3.12a-c show AMR curves for 25 nm thick and 100 nm wide Permalloy strips in an external magnetic field. The magnetization of the strip in fig. 3.12a is aligned nearly parallel to the current direction. The basic shape of the curve and the position of the switching feature are well fittet by an angle of $\alpha = 4°$ and an anisotropy constant $K = 5.5 \cdot 10^4 \, \text{J/m}^3$ (green curve). This also applies to a strip with a magnetization that forms roughly an angle of $45°$ with the current direction in the experiment. Its fit is shown in fig. 3.12b and the used fit parameters are $\alpha = 42.1°$ and $K = 6.3 \cdot 10^4 \, \text{J/m}^3$. For a magnetization perpendicular to the current direction (fig. 3.12c) we find the parameters $\alpha = 89.3°$ and $K = 7.8 \cdot 10^4 \, \text{J/m}^3$. That this model reproduces the data suggests that our Py strips contain a large single domain directed along the axis which

dominates the AMR signal. For increasing strip width w we find a decrease in the anisotropy constant K as expected (fig. 3.12d) [128, 130].

It should be noted that we expect K to be constant for a fixed w, independent of the angle α, between the strip and the external magnetic field. However, we find an increasing anisotropy constant for $\alpha \to 90°$. The underlying Stoner-Wohlfarth model assumes an ellipsoidal single domain and a magnetization that can coherently be rotated in the external field. In contrast our strips are block-shaped. One can expect that the model is adequate for small α, but inaccurate for larger angles. One also has to keep in mind that the edges of the strips have a certain roughness, probably leading to small multidomain states for perpendicular magnetizations which might
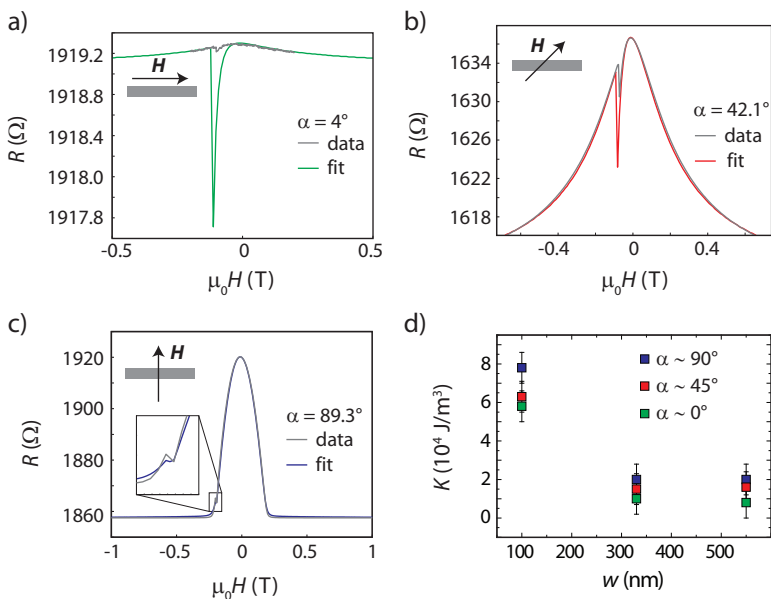
Figure 3.12: The AMR measurements can be fitted by a Stoner-Wohlfarth based model. The gray curves show the actual measurement, the fits are plotted colored. The three graphs correspond to AMR signals of 100 nm wide Py strips including an angle α with the external magnetic field. The parameters are: **a)** $\alpha = 4°$, $K = 5.5 \cdot 10^4$ J/m^3, **b)** $\alpha = 42.1°$, $K = 6.3 \cdot 10^4$ J/m^3 and **c)** $\alpha = 89.3°$, $K = 7.8 \cdot 10^4$ J/m^3. **d)** Plot of the anisotropy constant for strips with different width. K is decreasing for an increasing w. Higher anisotropy constants are found for increasing α, due to the rectangular geometry of the strip. The used model is only accurate for an elipsoidal geometry and a coherently rotating magnetization.

be less relevant for electron transport.

In fig. 3.13, we plot the switching fields H_S extracted from AMR measurements on Py strips parallel to the magnetic field as a function of the width w (black squares). A decreasing switching field due to shape anisotropy is found for increasing strip width in good agreement with [128, 129, 130]. In the range between $w = 80$ nm and $w = 300$ nm the switching field varies by a factor 5, or at least 80 times the width of a single AMR switching. The blue triangles represent VSM transition fields H_{90} of the Py strip grids for the strips with 110, 220 and 550 nm width. They match very well the data obtained from the single strips.

The anisotropy constants from the fits of the Stoner-Wohlfahrt model for $\alpha \sim 0°$ are indicated by the red dots in the figure. The anisotropy constant K is related to the switching field by $K = \frac{1}{2}\mu_0 H_S M_S$. The determined anisotropy constants are also in good agreement with switching fields of strips and the grids. The dashed line is a guide to the eye.

Theoretically, the switching field (or coercive field) of block-shaped strips can be calculated with the help of the demagnetization field (equation 1.17) introduced in chapter 1. The energy density of the strip is the sum of its energy per unit volume in the external magnetic field and in the demagnetization field

$$
\begin{aligned}
E =& E_{\text{ext}} + E_{\text{d}} \\
=& -\mu_0 \boldsymbol{M}\boldsymbol{H} + \frac{1}{2}\mu_0 \boldsymbol{M}\boldsymbol{H_d} \\
=& -\mu_0 M_S H \cos(\alpha - \theta) + \frac{1}{2}\mu_0 M_S^2 (\mathcal{N}_\perp \sin^2(\theta) - \mathcal{N}_\parallel \cos^2(\theta))
\end{aligned}
\tag{3.3}
$$

The angles α and θ are measured between the long easy axis of the strip and $\boldsymbol{H}$ and $\boldsymbol{M}$, respectively (as in the Stoner-Wohlfahrt model fig. 1.4). Due to the simple geometry and assuming a rotation of the magnetization in the strip plane, only demagnetization factors along the strip axis $\mathcal{N}_\parallel$ and perpendicular to the strip axis $\mathcal{N}_\perp$ in the strip plane have to be considered. The switching field $H_S = M_S(\mathcal{N}_\perp - \mathcal{N}_\parallel) = \frac{2K}{\mu_0 M_S}$ is found by minimizing the energy in eq. 3.3 [28]. K is the anisotropy constant. The demagnetization factors for block-shaped structures are

$$
\mathcal{N}_\perp = \frac{1}{\pi}\left[\frac{1 - \left(\frac{w}{t}\right)^2}{2\frac{w}{t}} \cdot \ln\left(1 + \left(\frac{w}{t}\right)^2\right) + \frac{w}{t} \cdot \ln\left(\frac{w}{t}\right) + 2\arctan\left(\frac{t}{w}\right)\right]
\tag{3.4}
$$

and $\mathcal{N}_\parallel \approx 0$ [133]. The full gray line in the plot is the theoretical prediction of this model for the dependence of the switching field on the width for
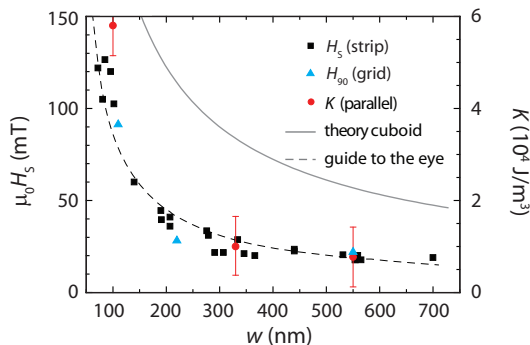
Figure 3.13: AMR switching fields of individual Py strips H_S (black squares) and VSM transition fields of the strip grids H_{90} (blue triangles) as a function of the contact width for H parallel to the strips. The switching fields of the strips can be tuned by a factor of 5 by the contact width. The gray line is the theoretically expected dependence for block shaped Permalloy strips ($t = 25\,\mathrm{nm}$, $M_S = 740\,\mathrm{kA/m}$) with no fit parameters. It shows an offset compared to the measured values probably due to the not ideal shape of the strips and to edge roughness effects. The dashed line is a guide to the eye.

block-shaped Permalloy strips with a thickness $t = 25\,\mathrm{nm}$ and a saturation magnetization $M_S = 740\,\mathrm{kA/m}$ as extracted from independent experiments discussed above. The prediction is offset from the measured data, probably due to the geometry of the strips. The underlying theory assumes perfectly shaped cuboids. This is not the case for our strips. Edge roughness and grains in the material can also lead to deviations in the coercive field as shown by Moon *et al.* [130]. They will lead to a switching earlier than predicted.

We conclude that our Py strips are showing mostly single domain behavior and that by controlling the width of the contacts we can reproducibly tune the switching field of the Py strips on technically and experimentally useful scales.

step IV: contact to nanotubes

To determine the contact properties of Permalloy to carbon nanotubes, we contacted a CNT with one Py contact and two Pd reference electrodes. The device is shown in fig. 3.14a. The Py electrode has a width of 500 nm and an edge to edge distances to the Pd electrodes 1 and 3 of 500 nm and 100 nm, respectively. The room temperature resistances measured between two electrodes are $R_{32} = 27\,\mathrm{k\Omega}$ and $R_{21} = 17\,\mathrm{k\Omega}$, respectively. These

resistances are in the same range as for our Pd-CNT-Pd devices. When the device is cooled to temperatures of a few Kelvin, two independent quantum dots form in the two segments of the tube. The black line in the conductance graph in fig. 3.14b represents the conductance of QD2 at a temperature 1.6 K for a small backgate voltage range. To measure the coupling of the Py contact to the CNT we apply a current to the CNT measuring the voltage drop over the two Pd contacts 1 and 3 and put the Py contact on ground. The conductance G_{31} (red line) is nearly identical to the conductance G_{32} of QD2 measured between the Pd contact 3 and the Py contact 2. The ratio of the two conductances $G_{31}\,/\,G_{32}$ (grey line) is plotted in the same figure and shows no strong deviations from unity. We conclude that we have a strongly coupled Py contact and that the conductance is dominated by QD2, as measured in G_{32}. Further studies on contact properties and quantum dot formation are presented in the next chapter.
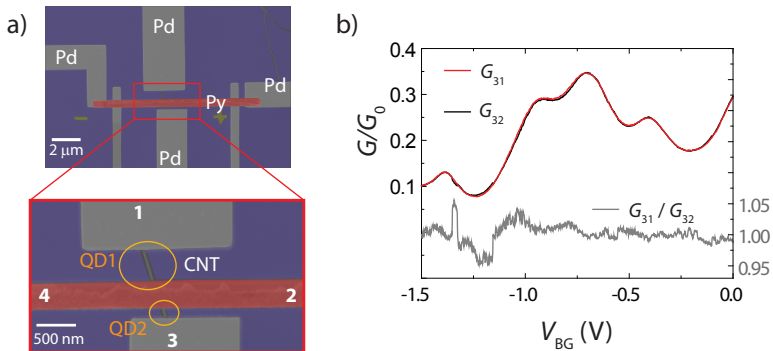
Figure 3.14: a) False-color SEM image of a CNT contacted by a 500 nm wide Py contact and two Pd reference electrodes. Two QDs are forming at low temperature. **b)** The conductance of QD2 is plotted in black. The red line is the conductance of both QDs in a row, when the Py strip is on ground. It shows nearly the same behavior as QD2. This means that the conductance is then strongly dominated by QD2. The ratio of the two measured curves is plotted in grey.

3.3 Conclusion

In this chapter we investigated ferromagnetic metals for their use as contact materials for CNT devices. The material has to fulfil the following requirements: 1) a large spin polarization, 2) a dominating shape anisotropy over the crystal anisotropy, 3) a single magnetic domain covering the contact

area, 4) in-plane magnetization and 5) reproducible electronic coupling to the CNT. The results of our studies are summarized in the table in fig. 3.15. Our material of choice is Permalloy which fulfils all the requirements. In the next chapter we present a CNT spin-valve fabricated with Py contacts.

	spin polarization	shape anisotropy	domain state	magnetization direction	coupling to CNTs	comment
Ni	33 % [c]	not dominant [b]			good [e]	
Fe	44 % [c]	not dominant [b]		component out-of-plane [b]		not explainable w. SW model [b]
Co	42 % [c]	dominating [b]		in-plane [b]	poor [d]	
PdNi		not dominant [d,f]	multiple [d,f]	component out-of-plane [d,f]	good [b]	
PdNi/Co		not dominant [b]		component out-of-plane [b]	good [b]	multilayer [b]
PdFe					good [b]	alloy evaporation problem [b]
Permalloy	48 % [c]	dominating [a]	single [a]	in-plane [a]	good [a]	

[a] H. Aurich *et al.*, APL **97**, 153116 (2010)

[b] H. Aurich, this thesis

[c] J.S. Moodera *et al.*, Annu Rev. Mater. Sci. **29**, 381 (1999)

[d] G. Gunnarsson, PhD thesis University of Basel (2007)

[e] J.R. Hauptmann *et al.*, Nature Physics **4**, 373 (2008)

[f] C. Feuillet-Palma *et al.*, Phys Rev. B **81**, 115414 (2010)

Figure 3.15: Summary of the material studies for the ferromagnetic contacts. The only material that fulfils all requirements is Permalloy ($Ni_{80}Fe_{20}$).

Chapter 4

Permalloy-based CNT Device

In this chapter we present measurements on a CNT contacted with two ferro-magnetic Py contacts and two Pd contacts. We first discuss the formation of quantum dots in the segments of the CNT between the different contacts and show that the inderdot coupling is relatively small. Then we present measurements on the spin-valve, defined by the two Py strips and the nanotube segment in between. We can directly relate the spin-valve characteristics to the magnetization reversal of our Py contacts found in AMR measurements of the single strips[1]. The TMR signal can be tuned with the backgate. In the last part of this chapter, we discuss magnetoresistance measurements in a non-local geometry and magnetoresistance effects that could influence or mimic spin-valve behavior.

4.1 Formation of quantum dots

Fig. 4.1 shows an SEM image of a CNT contacted in the center by two Py contacts (labelled 2 and 3) of width 400 nm and 140 nm, with an edge to edge distance of 370 nm. At the top and bottom two Pd contacts (4 and 1) are placed as reference. The Py strips are contacted in a four-terminal geometry for AMR characterization. The CNT diameter was found by AFM as 1.2 ± 0.3 nm, averaged along a segment of 100 nm. This is a typical diameter for an individual single wall CNT [12]. The resistances at room temperature between the contacts $1-2$, $2-3$ and $3-4$ are 38, 26 and 20 kΩ,

---

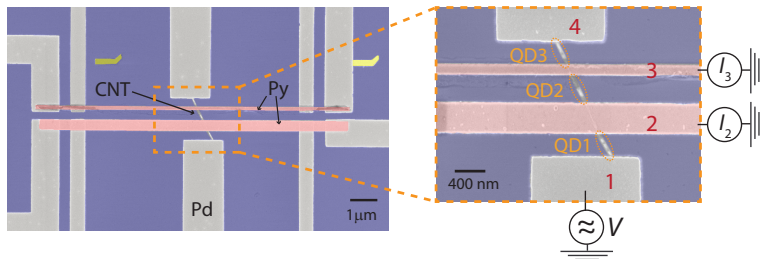[1]Parts of this work have been published in [108].

Figure 4.1: False-color SEM image of a CNT contacted by two Py electrodes and 2 Pd reference electrodes. The Py electrodes have a width of 400 nm and 140 nm, respectively and are contacted in a four-terminal geometry to measure the individual AMR signals of the strips. Their edge to edge distance is 370 nm. The zoom-in shows the CNT contacted by the two Pd electrodes 1 and 4 and the two Py electrodes 2 and 3. Quantum dots (labelled QD1, QD2 and QD3) are forming in between two electrode pairs, when the device is cooled to cryogenic temperatures. To measure the coupling of the Py electrodes to the CNT we apply a voltage to a Pd electrode and measure the currents I_2 and I_3 at the two Py electrodes simultaneously.

respectively. No band gap is observed and the CNT behaves like a metal or small bandgap semiconductor.

At 230 mK, all segments show Coulomb blockade oscillations as a function of V_{BG}, providing evidence for carrier confinement in these regions. The four contacts divide the CNT into three quantum dots labeled QD1, QD2 and QD3. The differential conductance $G = dI/dV$ for QD2 forming between the two Py contacts as a function of the backgate voltage V_{BG} is plotted in fig. 4.2a ($G_0 = 2e^2/h \approx 7.748 \cdot 10^{-5}\,\Omega^{-1}$). The peak values of the conductance reach $0.85\,G_0$, suggesting a strong and quite symmetric coupling of the two Py contacts to the CNT. The stability diagram for QD2 is shown in the lower part of the figure. The charging energy of the dot is ~ 1.5 meV, an orbital energy is too small to be detected. The lever arm of the backgate is $\eta = \frac{\Delta V_{SD}}{\Delta V_{BG}} \approx 0.02$. The FWHM ~ 1 meV. This is much larger than the broadening by temperature (~ 0.02 meV for $T = 230$ mK), which suggests that the QD level broadening is dominated by the coupling to the leads (lifetime broadening). Assuming symmetric tunnel coupling results in $\Gamma_1 \approx \Gamma_2 \approx 0.5$ meV.

Fig. 4.2b shows the differential conductance for QD1 forming between the Py contact 2 and the Pd reference electrode 1 as a function of the backgate voltage. The highest conductance values reach only $0.2\,G_0$ suggesting a more asymmetric coupling of the two contacts. The charging energy and lever arm extracted from the stability diagram are $U_C \approx 1.5$ meV and $\eta = \frac{\beta_+ |\beta_-|}{\beta_+ + |\beta_-|} \approx$
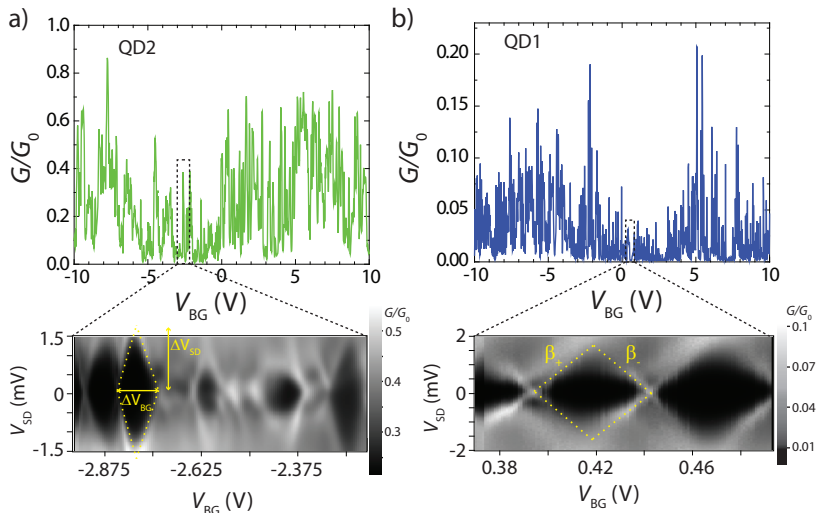
Figure 4.2: a) Conductance of the QD2 forming between the two Py contacs at low temperature ($T = 230\,\mathrm{mK}$) as a function of the backgate voltage. The peak values of $0.85\,G_0$ suggest a strong symmetric coupling of the contacts. The stability diagram of QD2 is shown below. **b)** Coulomb blockade and stability diagram for QD1 (Py-CNT-Pd) at $230\,\mathrm{mK}$.

0.03. For both diagrams the Coulomb diamonds are relatively symmetric suggesting a quite symmetric capacitive coupling to the leads.

We characterize the coupling of a single Py contact by applying a voltage to contact 1 and measuring simultaneously the two resulting currents in the Py terminals 2 and 3 (see schematic in fig. 4.1). Conductance curves for a small backgate voltage range of the two dots at low temperature are plotted in the upper part of fig. 4.3a. The green line shows the conductance of QD2 whereas the blue line represents the conductance of QD1 five times magnified. The differential conductance between contacts 1 and 3, essentially given by $G_{31} = I_3/V$, is shown in black in the lower part of the figure and exhibits peak maxima of $\sim 0.004\,G_0$, about 30 times smaller than $G_{21} = I_2/V$, indicating that most of the current flows into contact 2. The transmission $T_{31} = G_{31}/G_0$ is reproduced very well by the product of the transmissions $T_{\mathrm{QD1}} = \frac{G_{\mathrm{QD1}}}{G_0}$ and $T_{\mathrm{QD2}} = \frac{G_{\mathrm{QD2}}}{G_0}$ obtained from the two-terminal conductances of QD1 and QD2, respectively, and a factor $f \approx 0.075$: $T_{31} \approx f T_{\mathrm{QD1}} T_{\mathrm{QD2}}$. This function is plotted in red in the lower part of the figure.

These characteristics are not expected on the first sight. Two quantum dots in series are forming in the device between the contacts 1-2 and 2-3 at low temperatures as indicated in the schematic in fig. 4.3b. In a classical picture for diffusive transport one can consider the dots as two conductors with conductances G_{QD1} and G_{QD2} leading to a total conductance of the device $\frac{G_{\mathrm{QD1}}G_{\mathrm{QD2}}}{G_{\mathrm{QD1}}+G_{\mathrm{QD2}}}$. This already describes the basic shape of the measured conductance, but shows an overestimation of several features and a generally too large total conductance. A similar behavior is also obtained by assuming
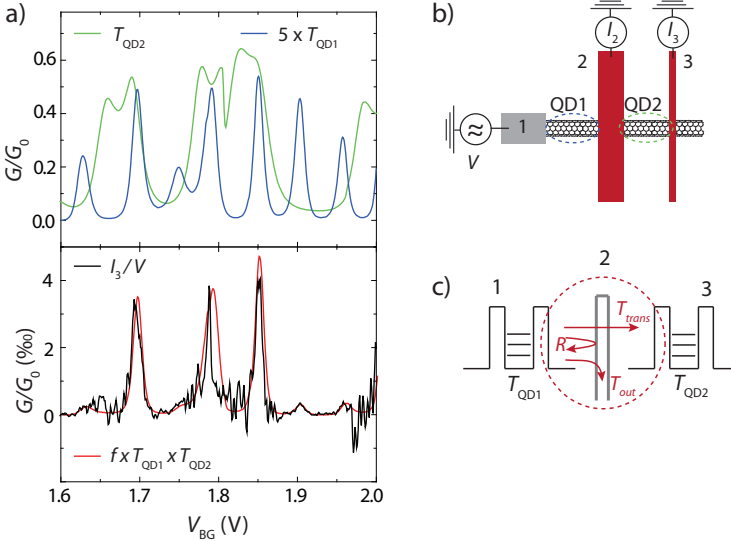
Figure 4.3: a) Upper graph: Coulomb blockade oscillations in the differential conductance as a function of V_{BG} for QD2 (with two Py contacts) plotted in green and QD1 plotted in blue (5x magnified) at $T = 230\,\mathrm{mK}$. The bottom part shows the conductance between contacts 1 and 3 when contact 2 is grounded (black curve). The measured signal can be fitted by multiplying the individual transmissions $T_{QD1(2)} = G_{QD1(2)}/G_0$ of the two dots and a factor $f \approx 0.075$: $T = fT_{\mathrm{QD1}}T_{\mathrm{QD2}}$ (red curve). **b)** Measurement scheme for the transparency of a contact. A voltage is applied at the Pd contact (gray). Simultaneously, the currents I_2 and I_3 are measured. Two QDs are forming between the contacts 1-2 and 2-3 respectively. **c)** The transmission through the individual QDs are T_{QD1} and T_{QD2}. The red dotted circle discribes the complex situation in the contact 2 for electrons comming from QD1. The same situation can be assumed for QD2. Electrons are taken out of the circuit with a transmission rate T_{out} or reflected in the dot with a reflectivity R. A part of the current is transmitted with transmission T_{trans} to QD2.

two coherent conductors in series with known transmissions T_{QD1} and T_{QD2} [134]: the transmission of two coherent conductors can be expressed by $T = \frac{T_{QD1}T_{QD2}}{1-2\sqrt{R_{QD1}R_{QD2}}\cdot\cos(\theta)+R_{QD1}R_{QD2}}$ with $R_{QD1(2)} = 1 - T_{QD1(2)}$ and θ the phase shift acquired between the reflection processes.

We find that both models are not applicable to describe the observed conductance. They both base upon the assumption of two conductors in series with known transmissions, measured in individual experiments. However, the situation cannot be described by a simple combination of the two individual systems. A possible explanation of the measured conductance can be given by considering the situation depicted in fig. 4.3c. The transmissions T_{QD1} and T_{QD2} of the individual dots are measured between the contacts 1-2 and 2-3, respectively. However, when the total transmission T_{31} between 1 and 3 is measured, one finds not only a combination of the two individual measurements, there is also a current path in the CNT below the contact 2 that has to be included. The schematic in the dotted circle describes the complex processes assumed to take place in contact 2 for electrons arriving from dot 1. Comparable processes are assumed for the electrons of dot 2. The current can be reflected with a probability R. This leads to the formation of the QD states. A part of the current is taken out of the system with transmission T_{out}. T_{trans} describes a small direct transmission of the current from dot 1 to dot 2 under the contact.

When the transmission between the two quantum dots is small, the total system can be described by a Hamiltonian $H_{tot} = H_{QD1} + H_{QD2} + H_t$ with $H_{QD1(QD2)}$ describing the individual dots in equilibrium (including R and T_{out}) and H_t is a hopping term evoked by the weak coupling. Assuming an effective density of states proportional to the measured transmission $N_1 = \nu_1 T_{QD1}$ and $N_2 = \nu_2 T_{QD2}$ (with $\nu_{1(2)}$ proportionality factors), describing the probability to find electrons with a certain energy on the dots, it is possible to construct the transmission between the dots by Fermi's golden rule [135]

$$T_{QD1 \rightarrow QD2} = \frac{2\pi}{\hbar} \left| \langle QD1 | H_t | QD2 \rangle \right|^2 N_1 N_2 = \frac{2\pi}{\hbar} T_{trans} N_1 N_2 \qquad (4.1)$$

with $|QD1\rangle$ and $|QD2\rangle$ the initial and final eigenstates of $H_{QD1} + H_{QD2}$ and $\langle QD1 | H_t | QD2 \rangle$ the hopping matrix element. Expressing the effective DOS in terms of the transmissions as assumed above leads to

$$T_{QD1 \rightarrow QD2} = \underbrace{\frac{2\pi}{\hbar} T_{trans} \frac{1}{\nu_1 \nu_2}}_{f} T_{QD1} T_{QD2} \equiv f T_{QD1} T_{QD2} \qquad (4.2)$$

with f defined as the proportionality factor observed above. The model shows that the observed transmission can be explained by two strongly de-

coupled coherent subsystems with a small transmission.

Applying the bias on contact 4 (not shown) through the more transparent QD3 and measuring the conductances G_{43} and G_{42} yields ~ 8 times smaller current in the second Py contact than in the first along the current direction. A possible explanation is a weaker coupling of the narrower Py contact to the CNT if one assumes a distributed contact with current transported in the CNT under the contact [136].

4.2 CNT spin-valve

The two Permalloy contacts 2 and 3 and the carbon nanotube segment form a lateral CNT spin-valve. We observed sharp TMR switchings that can directly be related to the AMR of the individual contacts [108]. The size and sign of the measured TMR can be tuned with the backgate voltage. All magnetoresistance measurements presented here were done at 230 mK.

4.2.1 Relation of the TMR to contact switching effects

An example of a TMR measurement is plotted in fig. 4.4. The differential conductance of QD2 between the Py contacts is shown as a function of the external magnetic field applied along the Py strips. The backgate voltage was fixed at 0.656 V, corresponding to a Coulomb oscillation maximum. We
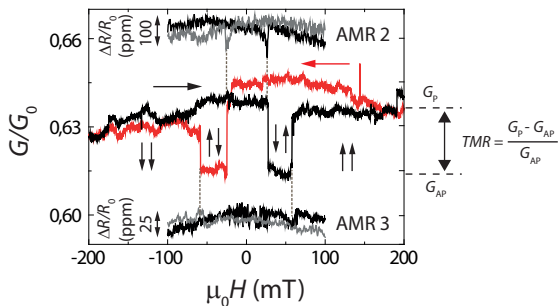
Figure 4.4: TMR signal between two Py contacts on a Coulomb oscillation maximum as a function of the external magnetic field applied parallel to the contacts. The relative magnetization directions of the contacts are indicated by arrows. The conductance shows sharp changes at the magnetic fields of ± 26 mT and ± 58 mT, respectively. These values correspond very well to the fields of magnetization reversal for the two Permalloy contacts. The top and bottom curves in the graph are the AMR signals of the individual Py contacts 2 (AMR 2) and 3 (AMR3).

find sharp switchings of $\mu_0 \Delta H < 1\,\mathrm{mT}$ (corresponding to the measurement step size) with an amplitude of $\sim 4.5\,\%$ at the magnetic fields $\pm 26\,\mathrm{mT}$ and $\pm 58\,\mathrm{mT}$. The switching fields determined from the TMR measurements correspond very well to the fields of magnetization reversal in the Py contacts found in the AMR measurement of the individual contacts, plotted above and below the conductance curves in fig. 4.4. The relative magnetization orientations of the electrodes are indicated in the figure. In addition to the sharp switching a gradual conductance change with the magnetic field is observed ($\sim 0.01 G_0/200\,\mathrm{mT}$), tentatively attributed to small domain rotations due to the magnetic field.

If the spin polarization of the Py contacts is calculated using Jullière's model with this TMR value assuming equally polarized contacts, we find $P \sim 15\,\%$, considerably smaller than expected from the bulk polarization. In the next section we show that Jullière's model is too simple to describe our device and that the nanostructure is crucial to the spin-valve.

4.2.2 Tunability of the TMR signal

The conductance traces presented above are measured at a fixed backgate voltage corresponding to a Coulomb blockade maximum. We find a strong dependence of the TMR on V_{BG}. Fig. 4.5a shows the conductance over V_{BG} of QD2 in a small backgate voltage range. The position where the TMR in fig. 4.4 has been measured is indicated by a blue square. Another TMR measurement is done on a Coulomb blockade peak at a backgate voltage of $0.745\,\mathrm{V}$ and the measured conductance over the magnetic field can be seen in fig. 4.5b. The position is labelled by a green square in the conductance graph. The shape of the measured conductance traces is similar to the signal measured on the other peak but the amplitude of the TMR is smaller ($TMR \sim 1.5\,\%$). The observed background is similar to the background observed in fig. 4.4 but with a smaller change in conductance with the magnetic field ($\sim 0.005 G_0/200\,\mathrm{mT}$). A TMR measurement between two Coulomb blockade peaks in a valley (yellow square, $V_{\mathrm{BG}} = 0.692\,\mathrm{V}$) shows an increase of conductance when the contacts switch from the parallel to the antiparallel state (fig. 4.5c). This leads to a negative TMR with an amplitude of $\sim -2.7\,\%$. The background of this measurement is quite unstable. It is not possible to determine its exact shape due to sample instabilities. However, the switching features are still visible very well. The black line in fig. 4.5d is the conductance in the parallel configuration. Due to problems with the device instability it was not possible to measure the corresponding conductance trace for the antiparallel configuration. (Device instabilities are discussed in chapter 2 and appendix B.) We find an oscillating behavior of the TMR between $+5.5\,\%$ and $-2.7\,\%$ with the backgate
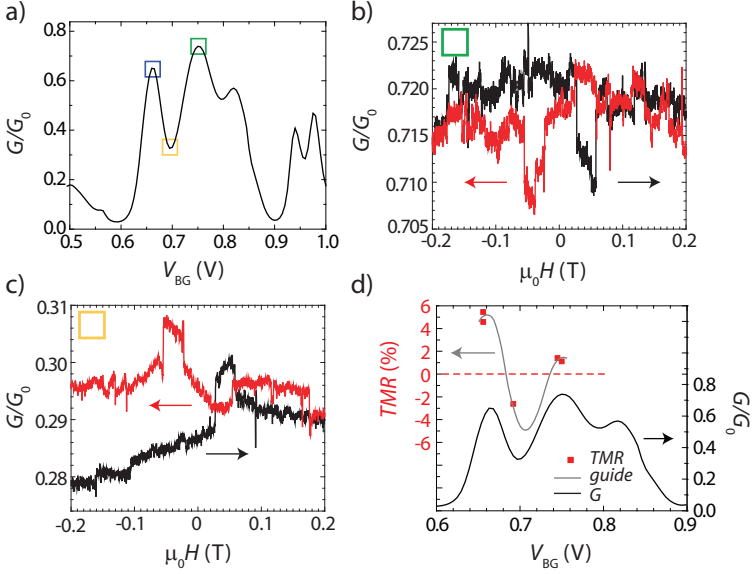
Figure 4.5: a) Coulomb oscillations of the conductance G of QD2 with V_{BG}. The blue square indicates the position where the signal in fig. 4.4 has been measured. Measurements on the green and yellow marked positions can be seen in b) and c). **b)** The conductance depending on the magnetic field on the Coulomb blockade maximum has a similar shape to the signal in fig. 4.4. **c)** In a Coulomb blockade valley the conductance increases in the antiparallel configuration and the TMR signal changes sign. **d)** The size of the TMR is plotted for different V_{BG} in one graph together with the conductance of the device (black line). The grey line is a guide to the eye.

voltage. We obtain positive values for the TMR when the QD is tuned to a Coulomb blockade maximum and negative values for measurements between two Coulomb peaks. The gray line is a guide to the eye interpolating the oscillatory behavior of the TMR.

Oscillations of the TMR with V_{BG} in multi wall and single wall CNT devices have been observed for the first time by Sahoo *et al.* [19]. However, the results presented in this thesis are in contradiction to their observations, where $TMR < 0$ on Coulomb blockade peaks and $TMR > 0$ in the valleys in-between are documented.

4.2.3 Modelling of TMR in a QD spin-valve

An oscillating TMR signal cannot be explained with the simple Jullière model introduced in the first chapter of this thesis, because the tunneling process and the polarization in the FM leads are independent of V_{BG}. The TMR only depends on the polarization of the FM contacts and does not include spin-dependent effects at the interfaces to the barrier and in the barrier itself nor any other structure between the FM contacts. A first explanation of the backgate voltage dependent TMR was given by E.Y. Tsymbal *et al.* for magnetic tunnel junctions [49] and has been refined and generalized to different systems by A. Cottet *et al.* [137]. The transmission function of non-interacting electrons through a ballistic wire, capacitively coupled to a backgate, forms resonances because of multiple reflections of electrons between the two leads (standing waves). In addition, the coupling of the wave functions of the two spin species ($\sigma = \uparrow, \downarrow$) to the FM leads are different due to the spin-dependent DOS of the electrodes. This leads to reflections of the electron wave functions with different phases, making the resonant energy levels of the wire E_0^σ spin-dependent. Close to a resonance the transmission can be modeled by a spin-dependent Breit-Wigner formula [138, 19]

$$T^\sigma(E) = \frac{\Gamma_L^\sigma \Gamma_R^\sigma}{(E - E_0^\sigma)^2 + \frac{1}{4}(\Gamma_L^\sigma + \Gamma_R^\sigma)^2} \tag{4.3}$$

The spin-dependent coupling $\Gamma_{L(R)}^\sigma = \gamma_{L(R)}(1 \pm P_{L(R)})$ is composed of the spin-independent coupling $\gamma_{L(R)}$ to the left (right) lead and the polarization $P_{L(R)}$ of the contact. It describes the increase (decrease) of the probability of an electron to couple to a contact when it has the same spin as the electrons with the higher (lower) DOS at the Fermi level in the contact. We assume the polarization to be the same in the two contacts $P_L = P_R = P$. The resonant energy levels are given by $E_0^\sigma = \epsilon_0 - \epsilon^\sigma - e\eta V_{BG}$ with ϵ_0 the spin-independent part of the energy level and $\epsilon^\sigma = \pm\kappa(P_L + P_R) = \pm 2\kappa P$ the spin-dependent part, with κ a fitting parameter [19]. The last term describes the tunability of the resonant level with the backgate. Assuming two non-interacting spin channels, the total conductance is given by the sum of the contributions of the two spin channels [24]

$$G(E) = \sum_{\sigma=\uparrow,\downarrow} G^\sigma(E) = \frac{e^2}{h} \sum_{\sigma=\uparrow,\downarrow} T^\sigma(E) \tag{4.4}$$

and when we plug in equation 4.3 the conductance for parallel and antiparallel configuration of the electrode magnetizations can be expressed as

$$G_{\rm P} = \frac{e^2}{h} \left[\frac{\Gamma_{\rm L}^{\uparrow}\Gamma_{\rm R}^{\uparrow}}{(E - E_0^{\uparrow})^2 + \frac{1}{4}(\Gamma_{\rm L}^{\uparrow} + \Gamma_{\rm R}^{\uparrow})^2} + \frac{\Gamma_{\rm L}^{\downarrow}\Gamma_{\rm R}^{\downarrow}}{(E - E_0^{\downarrow})^2 + \frac{1}{4}(\Gamma_{\rm L}^{\downarrow} + \Gamma_{\rm R}^{\downarrow})^2} \right] \quad (4.5)$$

$$G_{\rm AP} = \frac{e^2}{h} \left[\frac{\Gamma_{\rm L}^{\uparrow}\Gamma_{\rm R}^{\downarrow}}{(E - E_0^{\uparrow})^2 + \frac{1}{4}(\Gamma_{\rm L}^{\uparrow} + \Gamma_{\rm R}^{\downarrow})^2} + \frac{\Gamma_{\rm L}^{\downarrow}\Gamma_{\rm R}^{\uparrow}}{(E - E_0^{\downarrow})^2 + \frac{1}{4}(\Gamma_{\rm L}^{\downarrow} + \Gamma_{\rm R}^{\uparrow})^2} \right]. \quad (4.6)$$

The first (second) term in the case of parallel conductance describes the transmission for electrons coming from a state with a high (low) DOS at the Fermi level and entering a state with a high (low) DOS at the Fermi level in the second electrode. The resonant energies are different for the two spin channels. In the case of antiparallel orientation of the contact magnetization the first term describes electrons with the spin-dependent resonant energy $E_0^{\uparrow}$ coming from a state with a high DOS at the Fermi level entering a state with a low DOS in the second electrode and vice versa for the second term.

To study the behavior of the conductances in the parallel and antiparallel electrode configuration, different cases can be considered:

Spin-independent resonant energy level

In the first case we assume the resonant energy level to be spin-independent $(E_0^{\uparrow} = E_0^{\downarrow} = E_0)$. The conductances far away from the resonant level $E - E_0 >> (\Gamma_{\rm L}^{\sigma} + \Gamma_{\rm R}^{\sigma})$ can be written as

$$G_{\rm P} \sim \left(\Gamma_{\rm L}^{\uparrow}\Gamma_{\rm R}^{\uparrow} + \Gamma_{\rm L}^{\downarrow}\Gamma_{\rm R}^{\downarrow} \right) \propto 1 + P^2 \quad (4.7)$$

and

$$G_{\rm AP} \sim \left(\Gamma_{\rm L}^{\uparrow}\Gamma_{\rm R}^{\downarrow} + \Gamma_{\rm L}^{\downarrow}\Gamma_{\rm R}^{\uparrow} \right) \propto 1 - P^2 \quad (4.8)$$

for the parallel and the antiparallel configuration, respectively. The $TMR = \frac{G_{\rm P} - G_{\rm AP}}{G_{\rm AP}} = \frac{2P^2}{1 - P^2}$ obtained in this case is always positive independent of the coupling asymmetry.

In the resonant case $E - E_0 \approx 0$, one has to distinguish between symmetric and asymmetric coupling of the contacts. Sahoo *et al.* [19] assumed very asymmetric coupling ($\gamma_{\rm R} >> \gamma_{\rm L}$), resulting in a negative $TMR = -\frac{2P^2}{1 + P^2} < 0$. This behavior is plotted in red in the upper graph of fig. 4.6a for

$\gamma_{\text{L}} = 0.1\,\text{meV}$ and $\gamma_{\text{R}} = 0.9\,\text{meV}$ (the other parameters are $\epsilon_0 = 0$, $\kappa = 0$)[2]. The conductances in the parallel and antiparallel configuration are plotted in black and gray, respectively. The assumption of an asymmetric coupling is proper to decribe the observation by Sahoo *et al.*. More symmetric coupling can result in a positive TMR in the resonant case as shown in the upper graph in fig. 4.6b. The model uses $\gamma_{\text{L}} = \gamma_{\text{R}} = 0.5\,\text{meV}$ as found experimentally.

The TMR on the Coulomb blockade maximum is plotted for increasing asymmetry $\gamma_{\text{R}}/\gamma_{\text{L}}$ with $\gamma_{\text{L}} = 0.5\,\text{meV}$ in fig. 4.6c (red line). It turns negative for an asymmetry of ~ 4. Therefore, a coupling with a small enough asymmetry could indeed explain our observation of $TMR > 0$ in the resonant case. However, the TMR measured off-resonance at the position $V_{\text{BG}} = 0.2\,\text{V}$ (plotted in green) is always positive in this model not in agreement with our experiment. Arrow 1 indicates the region where a signal as in ref. [19] can be observed but a measurement as indicated by arrow 2 is not observed for our device.

The two color scale plots in fig. 4.6c on the right show again the TMR for different combinations of coupling constants off and on a resonance. The TMR in the off-resonance case (at $V_{\text{BG}} = 0.2\,\text{V}$) is positive also for high asymmetries. For even higher asymmetries than plotted in the graph it is not reasonable still to talk about off-resonance because of the increased peak width. For the on-resonance situation regions with positive and negative TMR can be seen. The white dotted lines correspond to the situations plotted in the left graph.

Spin-dependent resonant energy level

A strong splitting of the resonant energy levels $\Delta E_0 = E_0^\uparrow - E_0^\downarrow$ can lead to an oscillating TMR with V_{BG}. One can imagine the level splitting ΔE_0 to be induced by *spin-dependent interfacial phase shifts* (SDIPS) [137]. The spin-dependent phase shifts can be due to a different scattering of electrons with spin orientation parallel and antiparallel to the contact magnetization at the interface between the wire and the FM contact. In the asymmetric case the level splitting can lead to the behavior plotted in the lower graph of fig. 4.6a ($\kappa = 0.5\,\text{meV}$). The conductance peaks for the parallel and the antiparallel alignment of the electrodes are deformed and slightly shifted with respect to each other. As a result, the TMR oscillates between positive and negative values on and off the resonances. In the case of symmetric coupling a similar behavior is observed as can be seen in the lower graph of fig. 4.6b. Oscillations in the conductance close to a resonance are possible.

---

[2]We use here the experimental result that the sum of the coupling constants is $\sim 1\,\text{meV}$ and assume an asymmetry of 1:9.
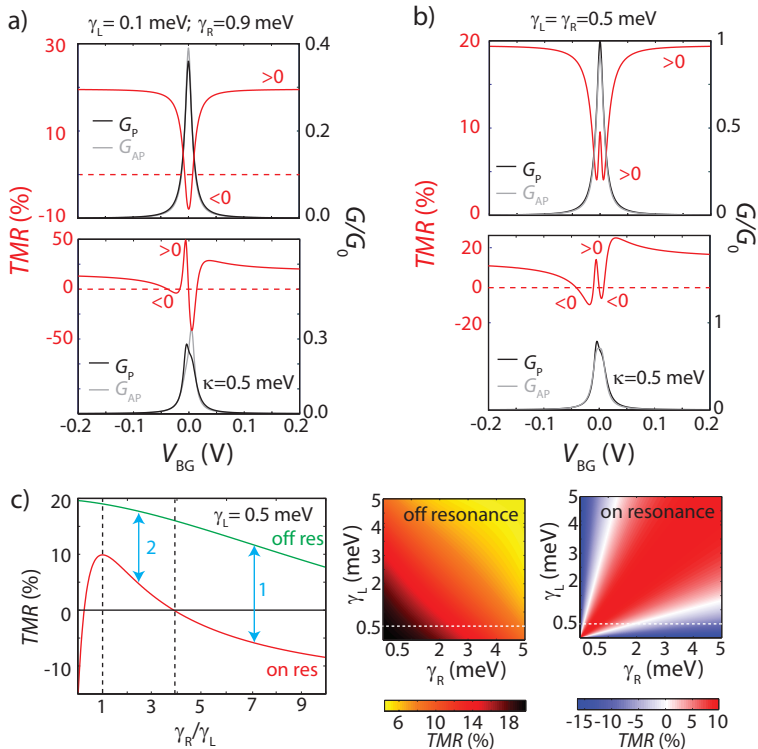
Figure 4.6: Calculated conductances G_P (black line), G_{AP} (gray line) and TMR (red line) for: **a)** the asymmetric case $\gamma_L = 0.1$ meV and $\gamma_R = 0.9$ meV. The upper graph shows the result for $\epsilon_0 = 0$ and $\kappa = 0$. A negative TMR on the peak is found. In the lower graph $\epsilon_0 = 0$ and $\kappa = 0.5$ meV. The TMR can be positive or negative in the resonant case. **b)** the symmetric case $\gamma_L = \gamma_R = 0.5$ meV. For $\epsilon_0 = 0$ and $\kappa = 0$, the TMR is always positive in the resonant case (upper graph). It is also positive on the resonance for $\kappa = 0.5$ meV, but can be negative close to it. **c)** Plot of the TMR on (red) and off (green) a Coulomb peak as a function of the coupling asymmetry. Ref. [19] assumes asymmetric coupling measuring a TMR signal as proposed by arrow 1. We assume more symmetric coupling, however the predicted result indicated by arrow 2 is not observed. The graphs on the right show a colorscale plot for the TMR in dependence of the coupling asymmetry. In the off-resonance case the TMR is always positive whereas in the on-resonance case it changes sign. The white dotted line marks the situation plotted on the left.

With the help of this simple model it is possible to understand the origin of magnetoresistance oscillations with the backgate voltage and the obser-

vation of positive or negative TMR on Coulomb blockade peaks, but it is not possible to reproduce the guide to the eye in fig. 4.5d) in our experiment. Additionally, it should be noted that the number of data point in our graph is very low, probably preventing the observation of substructures in the magnetoresistance signal that could be modelled with the assumptions made above.

In the model described above electron-electron interactions were neglected. In the Coulomb blockade regime they can have a considerable influence as shown by Cottet *et al.* [137, 139], who studied a quantum dot coupled to two FM leads in an Anderson model and calculated the conductance using an equation of motion technique. In their model they assumed a two-orbital QD with $K - K'$ orbital degeneracy. SDIPS were taken into account as
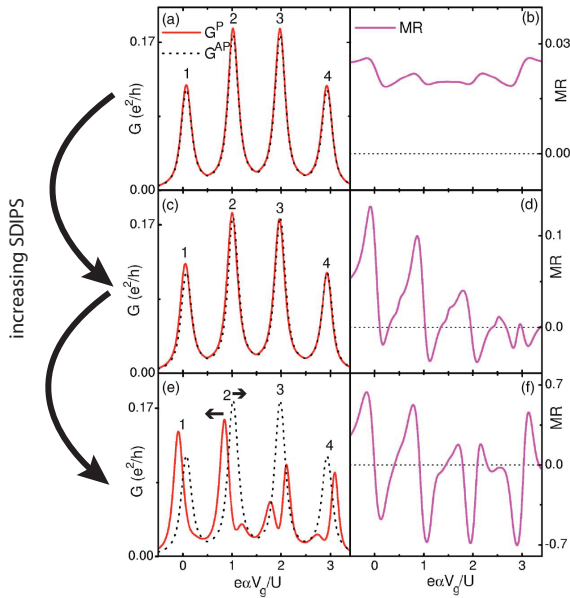
Figure 4.7: Figure taken from [139]. Calculated conductances G_P (red line) and G_{AP} (black dotted line) of a two-orbital quantum dot. The tunnel rates are $\Gamma_L = 0.0043U$ and $\Gamma_R = 0.0725U$ with $U = 30kT$. The contact polarization is 0.4 for both contacts, α is here the lever arm of the backgate. The energy splittings of the resonances are increasing from top ($\Delta E = 0.00U$) to bottom ($\Delta E = 0.3U$) as indicated in the figure. The pink lines represent the tunnel magnetoresistance corresponding to the conductances in the left figures.

parameters and are manifested in an effective spin-splitting of the dot energy levels, describable by an effective Zeeman splitting. Fig. 4.7 shows a plot taken from [139] for a symmetrically coupled CNT quantum dot with a doubly degenerate level. In the graphs on the left side the conductance in the parallel (red lines) and antiparallel (black dotted lines) configuration are plotted. The first two peaks correspond to the single occupation of K and K', the other two to double occupation. In fig. 4.7a no SDIPS are assumed. The TMR signal (fig. 4.7b, plotted in pink) is positive everywhere. The SDIPS parameter is added in fig. 4.7c and strongly increased in fig. 4.7e. Increasing the SDIPS leads to a strong shift of the conductance in the parallel and antiparallel case manifesting itself in strong TMR oscillations. The TMR signals plotted in fig. 4.7d and fig. 4.7f bear significant similarities to our experiments.

However, the origin of such SDIPS is not entirely clear. In addition to boundary scattering effects it is also possible that ferromagnetic impurities at the interfaces or ferromagnetic exchange coupling of the dot electrons to the leads [140] can influence the resonance conditions of the different spin channels.

4.3 Non-local geometry - preliminary results

The TMR signals discussed so far have been measured in a local or 2-terminal spin-valve geometry with two FM electrodes used to inject a spin polarized current into the CNT and to measure simultaneously the voltage drop on the same electrodes. However, magnetoresistance effects due to the FM contacts like anisotropic magnetoresistance effects [35], magneto Coulomb effects [141] or stray field effects in the CNT can distort or mimic the spin transport signal. Non-local measurement techniques offer the possibility to separate the spin current from the charge current and can help to distinguish those additional MR effects from spin accumulation.

In 1985 Johnson and Silsbee proposed a measurement set-up by which the charge current in a metal structure in the diffusive limit can be separated from the spin signal [30]. The basic measurement scheme is illustrated in fig. 4.8. In the *non-local* or *4-terminal geometry* a spin polarized current is injected into the metal by an FM electrode (3). Contact 4 is grounded, whereas the contacts 2 and 1 are floating. Therefore, a charge current only flows between 3 and 4. The injection of spin-polarized charges leads to a spin accumulation below 3. The different electrochemical potential $\mu_\uparrow$ and $\mu_\downarrow$ for the majority spins ($\uparrow$) and minority spins ($\downarrow$) are shown in the lower part of the figure. The spin accumulation, i.e. the difference in the electrochemical potentials for up- and down-spins, diffuses to both sides of the contact,
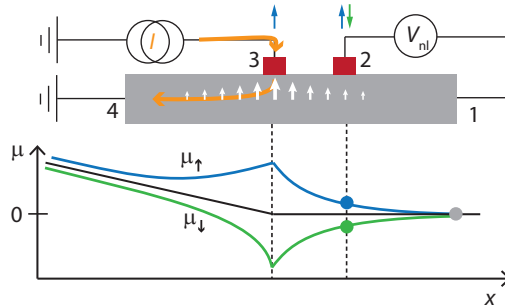
Figure 4.8: Non-local measurement set-up following Johnson and Silsbee [30]: A spin polarized current is driven from an FM (contact 3) through a non-magnetic material. Contact 4 is on ground. The charge current between contacts 2 and 1 is zero, however due to spin accumulation a spin current can be found. The lower part of the figure shows the electrochemical potentials $\mu_{\uparrow(\downarrow)}$ of the up- and down-spins. The different electrochemical potentials for the two spin species at the position of the FM electrode 2 are indicated by the blue and green dots, respectively.

independently of the charge current, as indicated by the white arrows. If 2 is made from an FM material it should be sensitive to the electrochemical potential of the majority or minority spins depending on its magnetization state (indicated by the blue and green dot in the scheme). It is then possible to measure a potential difference to 1 (gray dot) without a net charge flow between 1 and 2.

Non-local signals in CNTs depending on the magnetization orientation of the ferromagnetic contacts have first been demonstrated by Tombros *et al.* [54]. This publication analyzes MR signals with CNTs in the non-local geometry and compares them to the MR signals measured in the two-terminal geometry. The authors argue that the observed non-local magnetoresistance signals are due to spin transport only. The non-local MR signal is smaller than the two-terminal signal, possibly due to additional magnetoresistance effects from the contacts (see also discussion below). As a condition to observe non-local MR signals the authors claim that the contact resistance to the CNT must be low ohmic, but transport below the contacts has to be possible. In ref. [54] no gate voltage dependence of the conductance and the MR is provided. It is therefore not clear in which regime the MR signal is measured and if it depends on the backgate voltage. Their interpretation of the MR signal with a bipartite resistor network consisting of two branches for the two spin channels is valid as long as a delocalization of the carrier wave function can be neglected.

A spin-signal in the non-local voltage of a CNT in the coherent non-interacting regime contacted with FM and non-magnetic metal electrodes has been investigated by Feuillet-Palma *et al.* [104]. A non-local MR tunable by a gate voltage due to quantum interference was observed, as predicted theoretically [142]. The non-interacting scattering model assumes conservation of spin and orbital degree of freedom during transport. The dependence of the signal on the magnetization orientations of the contacts is induced by spin-dependent resonant effects due to SDIPS. In transport experiments in the non-interacting coherent regime, the wave functions extend over the whole length of the CNT, therefore charge transport is not separated from the spin transport and the MR signal is non-local with respect to the position of the FM and non-magnetic electrodes [104].

A schematic of our 'non-local set-up' with a CNT is shown in fig. 4.9a. The current is injected at the narrow Py contact 3 and contact 4 is grounded. The voltage is probed between the contacts 1 and 2 (input impedance 1 GΩ). A non-local measurement at $V_{\mathrm{BG}} = 0\,\mathrm{V}$ obtained by injecting a current of $I \approx 1\,\mathrm{nA}$ between 3 and 4 is shown in fig. 4.9b. We measure a non-local voltage V_{nl} between 1 and 2 and define the non-local conductance as $G_{\mathrm{nl}} = I/V_{\mathrm{nl}} \approx 230\,\mu\mathrm{S}$. At the magnetic fields where the FM contacts reverse their magnetization, known from AMR measurements, steplike changes in the conduction are observed. The regions with an antiparallel alignment of the contact magnetizations are shaded in gray in the figure. This non-local MR has a size of $MR_{\mathrm{nl}} = (G_{\mathrm{nl,P}} - G_{\mathrm{nl,AP}})/G_{\mathrm{nl,AP}} \approx -4.7\,\%$. An increase in
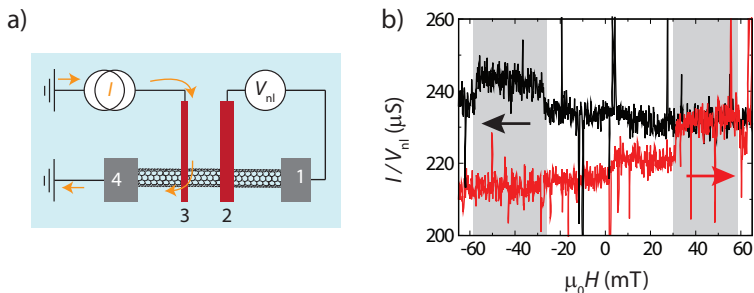
Figure 4.9: a) Schematic of a non-local measurement geometry. A spin polarized current is driven from the FM contact 3 through the nanotube and extracted at contact 4. The charge current between contacts 2 and 1 is zero, however due to spin accumulation a spin current can be found. **b)** Non-local MR signal of the device. Switching features at the expected positions can be seen. The shaded areas mark the regions where the contacts are aligned antiparallel.

the conductance in the antiparallel situation is consistent with the injection of majority spin electrons into the CNT from contact 3 in a diffusive picture. The majority spins in contact 2, aligned antiparallel to contact 3, have an opposite orientation to the accumulated electron spins and this causes a reduction in V_{nl} and thereby an increase in $G_{nl} = I/V_{nl}$ as also observed in experiments with diffusive Si nanowires [52]. The noise level is $\sim 8\,\mu S$, the same order of magnitude as the observed switching features (signal-to-noise ratio ~ 1.3). The observed background is rather flat but suffers from a drift and several small jumps due to device instabilities.

The measurement shows a resistance in the non-local geometry with switching features at the magnetic fields where the contacts change their magnetization. However, it is not straightforward to draw a conclusion from the magnetoresistance measurements in the non-local geometry in the two publications presented above for our device. We observe three quantum dots that are weakly but coherently coupled to each other. The regime where the experiments in the first publication has been performed is not known and the interpretation corresponds to a diffusive picture of spin accumulation. The second publication studies transport in a non-interacting coherent regime and cannot be compared to our measurements. Unfortunately, it was not possible to measure the non-local MR as a function of the backgate voltage due to electrical instabilities of the device. This would have allowed a direct comparison of local and non-local signals in the Coulomb blockade regime.

4.4 Discussion of other magnetoresistance effects

As shown above, magnetoresistance effects can be induced in CNTs with FM contacts due to spin-polarized transport. However, miscellaneous MR effects in the contacts can also be responsible for resistance change in a two-terminal transport experiment. We now provide a general discussion of such effects in relation to our experiment.

Anisotropic magnetoresistance effects

The electrical resistance of an FM electrode is not constant when an external magnetic field is applied. The AMR leads to gradually or step-like changes in resistance that can also be important in spin-transport measurements. This has e.g. been shown in all-metal spin-valve devices where the device resistance is dominated by the electrode resistances [143]. However, this small effect can be neglected for spin-valves dominated by a high tunnel resistance.

For very thin FM films ($<$ a few nanometers) it is shown that the magnetoresistance is dominated by electron tunneling between different islands

with different magnetization. At a certain thickness, when the islands coalesce, the resistance gets dominated by the AMR effect [144]. A comparable effect could also be imagined for multi-domain contacts consisting of grains with different magnetizations. It can be possible to have a TMR-like switching in the AMR signal that might also show in the spin-valve signal. The current in the FM electrode is then described by tunneling from one FM island in the material to the next. However, it is not clear how this will change the tunneling MR signal between two electrodes because it will depend on the location of the grains.

Another effect that can be considered is the tunneling AMR or TAMR effect. It can cause the switching characteristics of the injection contact to modulate the TMR. TAMR originates from spin-orbit coupling in an FM electrode with crystalline anisotropy and is most important for FM materials with a large SOI like FM semiconductors [145] but is also observed in FM metals [146]. Changes of the magnetization vector of the contact can be translated into a change in DOS by the spin-orbit coupling. This leads to a change in TMR.

The previous two arguments could in principle also lead to a spin-valve like signal in the device if only one FM contact is used, due to multiple switchings in one contact. However, it is very unlikely that one of those effects is important in our experiments because they would also show in AMR measurements. The AMR is well understood for our devices. We measure the AMR in our contacts and can explain their behavior in an external magnetic field by a Stoner-Wohlfarth like model for a single magnetic domain particle. The AMR signals show no additional features and coincide exactly with the observed spin-valve signal.

Magneto Coulomb effect

The magneto Coulomb effect (MCE) demonstrated by Ono *et al.* [141] in metallic structures could in principle also be relevant in CNT spin transport devices with FM contacts, as predicted by van der Molen *et al.* [147]. It has been demonstrated in InP nanowire devices that a magnetoresistance signal, controlled in sign and magnitude by an electric field, can be due to the MCE even if the device is contacted by only one FM and one non-magnetic contact [148].

The origin of MCE can be explained as follows: An external magnetic field leads to a Zeeman shift of the spin-up and spin-down bands in an FM contact. An FM material has a different DOS at the Fermi level for the two spin species. Therefore, the chemical potential of the FM is adjusted due to the repopulation of the empty states. When the FM is in contact with a non-magnetic lead, the electrochemical potential at the interface has to stay

constant. This leads to a rise of the electrical potential of the FM. Because of the weak coupling of the FM to the QD, the change in the electrical potential acts on the energy levels of the dot like an electrical gate. An increasing (or decreasing) magnetic field will therefore lead to a tuning of the dot energy levels. When the coercive field of one contact is reached, its magnetization direction changes, leading to a discontinuous change in conductance. This effect is relevant for a single contact already and the contributions of a second FM can simply by added. The conductance change due to a switching of both electrodes is written as [147]

$$\Delta G = \frac{dG}{dV_{\mathrm{BG}}} \cdot \frac{g\mu_{\mathrm{B}}P\left(C_1\mu_0 H_{S1} + C_2\mu_0 H_{S2}\right)}{eC_{\mathrm{G}}} \tag{4.9}$$

The first factor describes the slope of a Coulomb blockade peak. We estimate the maximal slope in our measurements to $\frac{dG}{dV_{\mathrm{BG}}} \approx \pm 20\frac{G_0}{V_{\mathrm{BG}}}$ However, it should be noted that this value depends on the set-up and temperature. The total capacitance of the device is estimated from the charging energy $U_{\mathrm{C}} = \frac{e^2}{C_\Sigma} \approx 1.5\,\mathrm{meV}$ to $C_\Sigma \approx 0.11\,\mathrm{fF}$. Assuming a symmetric capacitive coupling we estimate from the lever arm $\eta = e\frac{C_{\mathrm{G}}}{C_\Sigma} \approx 0.02$ the gate capacitance $C_{\mathrm{G}} \approx 2.2\,\mathrm{aF}$ and the source and drain capacitances $C_{\mathrm{S}} \approx C_{\mathrm{D}} \approx 54\,\mathrm{aF}$. $\mu_0 H_{S1} = 26\,\mathrm{mT}$ and $\mu_0 H_{S2} = 60\,\mathrm{mT}$ are the switching fields of the two contacts, $P = 0.4$ is the polarization.
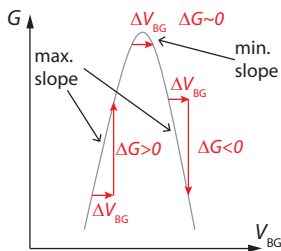

Figure 4.10: Schematic of the conductance change ΔG due to the magneto Coulomb effect. A change in the electrochemical potential of the FM contact acts on the QD like a backgate. The conductance change is maximal on the slopes of the peak and can be positive or negative there. It vanishes close to a peak maximum.

Fig. 4.10 shows a schematic of the conductance changes ΔG due to the magneto Coulomb effect, acting like a changing backgate with ΔV_{BG}. The slope of a Coulomb blockade peak gets minimal close to the maximum of the peaks and in the valleys between two peaks. Therefore, an MCE induced magnetoresistance should vanish there. This is not in agreement with our observation. We measure large MR signals close to peak maxima. The biggest contribution is expected for measurements on the side of a peak. The sign of the change depends on the sign of the slope. The MCE induces a gradually change in conductance until the contacts change their magnetization direction (consecutively). This produces a non-continuous step in

conductance of $\sim 0.002\,G_0$ which is to small to detect in our experiment (noise level $\sim 0.002\,G_0$).

The above described situation gives a small contribution to the MR signal in the spin-valve. However, a spin-valve like signal has different characteristics and can easily be discriminated[3].

Stray field effects

In addition to the applied external magnetic field, a stray field produced by an FM contact can act on the magnetic moments of the electrons in a QD. According to the analytical model provided in [149], the stray field of a 300 nm wide rectangular Permalloy contact, magnetized along its long axis, is around $30\,\mu$T close to the edge of the contact and similar in a distance of ~ 200 nm where the QD probably forms. This stray field leads to a Zeeman energy of $1/2g\mu_\mathrm{B}B \approx 1.7 \cdot 10^{-9}$eV (with $g = 2$). This energy shift of the Coulomb blockade peak leads to a change in conductance $\Delta G = \frac{\partial G}{\partial V_\mathrm{BG}} \cdot \frac{\partial V_\mathrm{BG}}{\partial E} \cdot \Delta E$. The first factor describes the maximal slope on the side of a Coulomb peak. We estimate $\frac{\partial G}{\partial V_\mathrm{BG}} < 20\frac{G_0}{V_\mathrm{BG}}$ for our device, however the slope depends on the set-up and the temperature. The second factor is the inverse lever arm.

For a stray field of $30\,\mu$T the maximal energy shift is $\sim 1.7 \cdot 10^{-6}\,G_0$ and is therefore difficult to observe. An observable effect would be obtained by magnetizing the contacts along their width or their height. The calculated stray field due to a magnetization in one of these directions can be as high as 1 T close to the contact. The Zeeman energy is then calculated to $\approx 5.8 \cdot 10^{-5}$ eV leading to non-negligible conductance changes of $\sim 0.06\,G_0$.

4.5 Conclusion

In this chapter we discussed a Permalloy-based CNT device with two Py and two Pd contacts. We showed that Py contacts couple strongly the the CNT, thereby forming quantum dots at low temperatures. The QDs are weakly coupled and the transmission through two dots can be modelled by $fT_\mathrm{QD1}T_\mathrm{QD2}$ with f a small transmission between the two dots. We found a spin-valve behavior with sharp switching features for the CNT contacted with two Py electrodes. The switching features of the MR device can directly be related to the magnetization reversal of the individual contacts. A back-gate tunable magnetoresistance was studied in a two terminal measurement.

---

[3]It should be noted that a spin-valve like signal in a device with only one FM and one non-magnetic contact was also observed in ref. [148]. This can be possible if the FM contact shows two magnetization switchings. However, this switchings should also be visible in AMR measurements and are very unlikely in our device.

The magnetoresistance was found to be modulated by the backgate voltage between $+4.5\,\%$ and $-2.7\,\%$. The observed TMR is positive on Coulomb blockade peaks and negative off the peak in contrast to literature report and can probably be explained by spin-dependent resonant states. A MR effect is also observed in a non-local geometry. However, due to instabilities of the quantum dots it was not possible to compare non-local with local TMR signals.

Chapter 5

Summary and Outlook

In this thesis different ferromagnetic materials were studied for their suitability as contact material for carbon nanotube spintronic devices. The requirements that have to be met by the FM contacts are 1) a large spin polarization, 2) the shape anisotropy dominates the crystal anisotropy, 3) a single magnetic domain covering the contact area, 4) in-plane magnetization and 5) reproducible electronic coupling to the CNT. We find that Permalloy (Py, $Ni_{80}Fe_{20}$) fulfils all our requirements [108]. The investigated Py contacts show an in-plane magnetization well aligned with the long axis of the strip. The switching of the magnetization in external magnetic fields can be modelled by a Stoner-Wohlfarth model for single-domain particles and the switching fields of the contacts can be reproducibly tuned by the width of the strips on technically and experimentally useful scales. Py provides a strong coupling and good electrical contact to CNTs comparable to the nonmagnetic Pd which is known as the best contact material to contact CNTs [90]. For this purpose, the formation of quantum dots is demonstrated at low temperatures. A CNT device with two Py electrodes shows spin-valve behavior with sharp switching features, directly related to the magnetization reversal of the individual contacts. The magnetoresistance of the spin-valve is electrically tunable in size and sign by an external gate.

A possible experiment in the near future can be a Hanle spin precession measurement in a CNT QD coupled to two Py contacts. It is suggested that in transport experiments through an individual single-level QD it is possible to measure directly the spin-decoherence time T_2 of the individual spins, whereas in optical realizations of Hanle experiments the spin-dephasing time T_2^*, averaged over a spin ensemble, is measured [10]. Another experiment

can make use of the strong coupling of Py to CNTs to study the magnetoresistance of a spin-valve in the Kondo regime or investigate the exchange interaction of a CNT state and the leads [150].

The aim in future experiments is to use the Py contacts on CNTs for spin projection measurements in electron entanglement experiments. Hofstetter *et al.* [73] recently realized a Cooper pair splitter in a semiconducting nanowire. A Cooper pair is injected from a superconducting lead into a semiconducting nanowire and split by Coulomb interactions. The splitting of Cooper pairs was succesfully shown, but to determine the degree of entanglement between the electrons, an analyzing tool e.g. ferromagnetic contacts are needed. Here comes the advantage of CNTs into play. Due to their small diameter it is easier to contact CNTs with FM contacts. The typical diameter of a semiconducting nanowire is a few ten nanometers, larger than the thickness of the Py contacts studied in this thesis. When the contact has to follow the shape of the nanowire this will lead to large stray fields and multi-domains states in the contact (see e.g. [143]). The spin states of the individual electrons are projected to the magnetization direction of the contacts. Two FM contacts with different switching fields can be used to measure the current correlations in the device in the parallel and antiparallel aligned configuration. However, this simple geometry is not sufficient to distinguish between an entangled state and a two-particle product state [151]. Spin-projection measurements in different directions are needed to prove the entanglement [152]. A possible realization of this idea is to replace one of the FM contacts with a synthetic antiferromagnetic (SAF) [153] disk con-
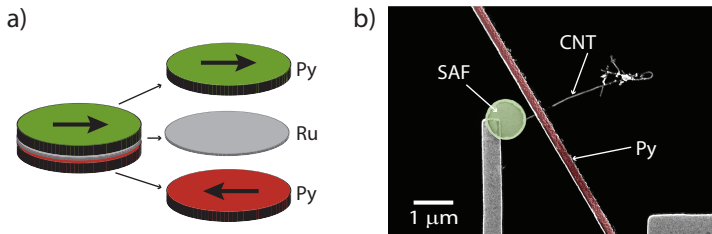
Figure 5.1: a) Schematic of a (simple) SAF disk. Two ferromagnetic Py layers are separated by a non-magnetic Ru layer. The magnetization of the Py layers align antiparallel and can be controlled by an external magnetic field. **b)** False-color SEM image of a CNT contacted with a Py strip and a Py/Ru multilayer SAF disk. The selectable magnetization direction of the disk allows spin projection measurements with different angles between the magnetization direction of the disk and the strip. The SEM image is kindly provided by Julia Samm.

sisting of a Py/Ru multilayer structure as shown schematically in fig. 5.1a. The magnetization direction of the disk can be set by an external magnetic field in any desired direction. For the right choice of the thickness of the Ru interlayer the magnetizations of the FM layers will show anti-parallel alignment leading to a minimization of the stray field of the disk[1]. An SEM image of a device can be seen in fig. 5.1b.

---

[1]This work is done in collaboration with Prof. B. Hickey from the University of Leeds.

Bibliography

[1] R. Keyes, IBM J. Res. Develop. **32**, 24 (1988).

[2] I. Žutić, J. Fabian, and S. D. Sarma, Rev. Mod. Phys. **76**, 323 (2004).

[3] S. D. Sarma, American Scientist **89**, 516 (2001).

[4] D. DiVincenzo, Science **270**, 255 (1995).

[5] G. Binasch, P. Grünberg, F. Saurenbach, and W. Zinn, Phys. Rev. B **39**, 4828 (1989).

[6] M. Baibich et al., Phys. Rev. Lett. **61**, 2472 (1988).

[7] M. Takagishi et al., IEEE Trans. Magn. **38**, 2277 (2002).

[8] A. Fert, Rev. Mod. Phys. **80**, 1517 (2007).

[9] M. Jullière, Phys. Lett. **A 54**, 225 (1975).

[10] M. Braun, J. König, and J. Martinek, Europhysics Letters **72**, 294 (2005).

[11] J. Hauptmann, J. Paaske, and P. Lindelof, Nature Physics **4**, 373 (2008).

[12] M. Dresselhaus, *Carbon Nanotubes - Synthesis, Structure, Properties, and Applications*, Springer (2001).

[13] S. Iijima, Nature **354**, 56 (1991).

[14] J.-C. Charlier, Rev. Mod. Phys. **79**, 677 (2007).

[15] S. Ilani and P. McEuen, Annu. Rev. Condens. Matter Phys. **1**, 1 (2010).

[16] M. Braun, J. König, and J. Martinek, Phys. Rev. B **70**, 195345 (2004).

[17] K. Dempsey, D. Ciudad, and C. Marrows, Phil. Trans. Roy. Soc. **369**, 3150 (2011).

[18] K. Tsukagoshi, B. Alphenaar, and H. Ago, Nature **401**, 572 (1999).

[19] S. Sahoo et al., Nature Physics **1**, 99 (2005).

[20] J. Stör and H. Siegmann, *Magnetism - From Fundamentals to Nanoscale Dynamics*, Springer (2006).

[21] L. Bergmann and C. Schaefer, *Lehrbuch der Experimentalphysik - Band 6: Festkörper*, de Gruyter 2nd edt. (1992).

[22] M. Getzlaff, *Fundamentals of Magnetism*, Springer Berlin (2007).

[23] S. Blundell, *Magnetism in Condensed Matter*, Oxford University Press (2007).

[24] S. Sahoo, *An experimental investigation of spin polarized transport in carbon nanotubes*, PhD Thesis University of Basel (2005).

[25] C. Tannous and J. Gieraltowski, Eur. J. Phys. **29**, 475 (2008).

[26] L. Néel, Compt. Rend. **224**, 1488 (1947).

[27] E. Stoner and E. Wohlfarth, Phil. Trans. R. Soc. A **240**, 599 (1948).

[28] E. Furlani, *Permanent Magnet and Electromechanical Devices: Materials, Analysis and Applications*, Academic Press (2001) .

[29] C. Chappert, A. Fert, and F. N. van Dau, Nature Materials **6**, 813 (2007).

[30] M. Johnson and R. Silsbee, Phys. Rev. Lett. **55**, 1790 (1985).

[31] R. Meservey, P. Tedrow, and P. Fulde, Phys. Rev. Lett. **25**, 1270 (1970).

[32] B. Jonker, Y. Park, and B. Bennett, Phys. Rev. B **62**, 8180 (2000).

[33] P. van Son, H. van Kempen, and P. Wyder, Phys. Rev. Lett. **58**, 2271 (1987).

[34] T. Valet and A. Fert, Phys. Rev. B **48**, 7099 (1993).

[35] F. Jedema, A. Filip, and B. van Wees, Nature **410**, 345 (2001).

[36] G. Schmidt, D. Ferrand, L. Molenkamp, A. Filip, and B. van Wees, Phys. Rev. B **62**, 4790 (2000).

[37] D. Smith and R. Silver, Phys. Rev. B **64**, 045323 (2001).

[38] R. de Groot and F. Mueller, Phys. Rev. Lett. **50**, 2024 (1983).

[39] E. Rashba, Phys. Rev. B **62**, 16267 (2000).

[40] S. Parkin et al., Nature Materials **3**, 862 (2004).

[41] B. Dlubak et al., Appl. Phys. Lett. **97**, 092502 (2010).

[42] A. Fert and H. Jaffrès, Phys. Rev. B **64**, 184420 (2001).

[43] G. Kirczenow, Phys. Rev. B **63**, 054422 (2001).

[44] M. Johnson and R. Silsbee, Phys. Rev. B **37**, 5312 (1988).

[45] N. Mott, Proc. R. Soc. Lond. **153**, 699 (1936).

[46] F. Jedema, M. Nijboer, A. Filip, and B. van Wees, Phys. Rev. B **67**, 085319 (2003).

[47] P. Wenk and S. Kettemann, *Handbook on Nanophysics: Spin Relaxation in Quantum Wires*, Francis and Taylor (2010) .

[48] T. McGuire and R. Potter, IEEE Trans. Magn. **11**, 1018 (1975).

[49] E. Tsymbal, A. Sokolov, I. Sabirianov, and B. Doudin, Phys. Rev. Lett. **90**, 186602 (2003).

[50] J. Katine, F. Albert, R. Buhrmann, E. Myers, and D. Ralph, Phys. Rev. Lett **84**, 3149 (2000).

[51] F. Jedema, H. Heersche, A. Filip, J. Baselmans, and B. van Wees, Nature **416**, 713 (2002).

[52] J. Tarun et al., J. Appl. Phys. **109**, 07C508 (2011).

[53] E. Hill, A. Geim, K. Novoselov, F. Schedin, and P. Blake, IEEE Trans. Magn. **42**, 2694 (2006).

[54] N. Tombros, S. van der Molen, and B. van Wees, Phys. Rev. B **73**, 233403 (2006).

[55] S. Koller, L. Mayrhofer, and M. Grifoni, New Journal of Physics **9**, 348 (2007).

[56] S. Ikeda et al., Appl. Phys. Lett. **93**, 082508 (2008).

[57] R. Meservey and P. Tedrow, Phys. Rep. **238**, 173 (1994).

[58] S. Datta and B. Das, Appl. Phys. Lett. **56**, 665 (1990).

[59] S. D. Sarma, J. Fabian, X. Hu, and I. Zutic, IEEE Trans. Magn. **36**, 2821 (2000).

[60] S. Iijima and T. Ichihashi, Nature **363**, 603 (1993).

[61] S. Tans et al., Nature **386**, 474 (1997).

[62] J.-R. Kim, H. So, J. Kim, and J.-J. Kim, Physica E **18**, 210 (2003).

[63] C. Schönenberger, *Bandstructure of graphene and carbon nanotubes*, solid state physics lecture (2000).

[64] S. Reich, J. Maultzsch, C. Thomsen, and P. Ordejon, Phys. Rev. B **66**, 035412 (2002).

[65] P. Jarillo-Herrero, *Quantum transport in carbon nanotubes*, PhD Thesis Technical University Delft (2005).

[66] C.-J. Park, Y.-H. Kim, and K. Chang, Phy. Rev. B **60**, 10656 (1999).

[67] M. Kastner, Physics today **46**, 24 (1993).

[68] L. Kouwenhoven, D. Austing, and S. Tarucha, Rep. Prog. Phys. **64**, 701 (2001).

[69] J. Petta and D. Ralph, Phys. Rev. Lett. **87**, 266801 (2001).

[70] J. Park et al., Nature **417**, 722 (2002).

[71] M. Skolnick and D. Mowbray, Annu. Rev. Mater. Res. **34**, 181 (2004).

[72] L. Kouwenhoven et al., *Electron transport in quantum dots*, proceedings of the Anvanced Study Institute on Mesoscopic Electron Transport, Kluwer Series E345 (1997).

[73] L. Hofstetter, S. Csonka, J. Nygard, and C. Schönenberger, Nature **461**, 960 (2009).

[74] J. Güttinger, T. Frey, C. Stampfer, T. Ihn, and K. Ensslin, Phys. Rev. Lett. **105**, 116801 (2010).

[75] R. Hanson, L. Kouwenhoven, J. Petta, S. Tarucha, and L. Vandersypen, Rev. Mod. Phys. **79**, 1217 (2007).

[76] S. Moriyama, T. Fuse, and K. Ishibashi, Phys. Stat. Sol. **7**, 2371 (2007).

[77] T. Ihn, *Semiconductor Nanostructures*, Oxford University Press (2010).

[78] S. Rossnagel, J. Cuomo, and W. Westwood, *Handbook of Plasma Processing Technology*, Noyes Publications (New Jersey) (1990).

[79] W. Kern, *Handbook of Semiconductor Cleaning Technology*, Noyes Publications (New Jersey) (1993).

[80] H. Dai, Acc. Chem. Res. **35**, 1035 (2003).

[81] J. Fuhrer, *Growth of single-wall carbon nanotubes by chemical vapor deposition for electrical devices*, PhD Thesis University of Basel (2006).

[82] B. Babic, J. Fuhrer, M. Iqbal, and C. Schönenberger, AIP Conf. Proc. **723**, 574 (2004).

[83] J. Cao, Q. Wang, and H. Dai, Nature Materials **4**, 745 (2005).

[84] T. Brintlinger, Y.-F. Chen, T. Dürkop, E. Cobas, and M. Fuhrer, Appl. Phys. Lett. **81**, 2454 (2002).

[85] J. Lefebvre, D. Austing, J. Bond, and P. Finnie, Nano Letters **6**, 1603 (2006).

[86] W. Kim et al., Nano Letters **3**, 193 (2003).

[87] S. Heinze et al., Phys. Rev. Lett. **89**, 106801 (2002).

[88] V. Vitale, A. Curioni, and W. Andreoni, J. Am. Chem. Soc. **130**, 5848 (2008).

[89] W. Kim et al., Appl. Phys. Lett. **87**, 173101 (2005).

[90] D. Mann, A. Javey, J. Kong, Q. Wang, and H. Dai, Nano Lett. **11**, 1541 (2003).

[91] D. Preusche et al., J. of Appl. Phys. **106**, 084314 (2009).

[92] M. Salou et al., Surf. Science **602**, 2901 (2008).

[93] D. Macintyre, O. Ignatova, S. Thoms, and I. Thayne, J. Vac. Sci. Technol. **B27**, 2597 (2009).

[94] I. Maximov, T. Holmqvist, L. Montelius, and I. Lindau, J. Vac. Sci. Technol. **B20**, 1139 (2002).

[95] J. Wi, H. Lee, and K. Kim, Electr. Mat. Lett. **3**, 1 (2007).

[96] S. Yasin, D. Hasko, and H. Ahmed, Microelectr. Engin. **61-62**, 745 (2002).

[97] M. Fuhrer, B. Kim, T. Durkop, and T. Brintlinger, Nano Letters **2**, 755 (2002).

[98] G. Steele, G. Gotz, and L. Kouwenhoven, Nature Nanotechnol. **4**, 363 (2009).

[99] K. Biswas and S. Kal, Microelectr. Journ. **37**, 519 (2006).

[100] A. Kleine, *Experiments on nonlocal processes in NS devices*, PhD Thesis University of Basel (2009).

[101] S. Oberholzer, *Fluctuation phenomena in low-dimensional conductors*, PhD Thesis University of Basel (2001).

[102] H. Preston-Thomas, Metrologia **27**, 3 (1990).

[103] K. Tsukagoshi, B. Alphenaar, and M. Wagner, Mat. Sci. and Engin. B **84**, 26 (2001).

[104] C. Feuillet-Palma et al., Phys. Rev. B **81**, 115414 (2010).

[105] A. Jensen, J. Hauptmann, J. Nygård, and P. Lindelof, Phys. Rev. B **72**, 035419 (2005).

[106] R. Thamankar et al., Appl. Phys. Lett. **89**, 033119 (2006).

[107] G. Gunnarsson, J. Trbovic, and C. Schönenberger, Phys. Rev. B **77**, 201405 (2008).

[108] H. Aurich et al., Appl. Phys. Lett. **97**, 153116 (2010).

[109] T.-Y. Yang et al., Phys. Rev. Lett. **107**, 047206 (2011).

[110] S. Foner, J. of Appl. Phys. **79**, 4740 (1996).

[111] B. Nagabhirava, T. Bansal, G. Sumanasekara, and B. Alphenaar, Appl. Phys. Lett. **88**, 023503 (2006).

[112] A. Fert and L. Piraux, J. Magn. Magn. Mat. **200**, 338 (1999).

[113] C. Hsieh, J. Liu, and J. Lue, Appl. Surf. Science **252**, 1899 (2005).

[114] A. Radulescu et al., IEEE Trans. Magn. **36**, 3062 (2000).

[115] T. Maassen, F. Dejene, M. G. aes, C. Josza, and B. van Wees, Phys. Rev. B **83**, 115410 (2011).

[116] G. Gunnarsson, *Transport measurement of single wall carbon nanotube multiterminal devices with normal and ferromagnetic contacts*, PhD Thesis University of Basel (2008).

[117] T. de los Arcos et al., J. Phys. Chem B **180**, 7728 (2004).

[118] J. Inoue and S. Maekawa, Phys. Rev. B **53**, 927 (1996).

[119] H. Man, I. Wever, and A. Morpurgo, Phys. Rev. B **73**, 241401 (2006).

[120] J.-Y. Chauleau et al., Phys. Rev. B **84**, 094416 (2011).

[121] L. Bocklage, J. Scholtyssek, U. Merkt, and G. Meier, J. Appl. Phys. **101**, 09J512 (2007).

[122] J. Moodera and J. Nassar, Annu. Rev. Mater. Sci. **29**, 381 (1999).

[123] R. Pickard, J. Turner, J. Birtwistle, and G. Hoffman, Brit. J. Appl. Phys. **1**, 1685 (1968).

[124] J.-G. Zhu, Materials today **6**, 22 (2003).

[125] S. Parkin, M. Hayashi, and L. Thomas, Science **320**, 190 (2008).

[126] K.-W. Moon, J.-C. Lee, M.-H. Jung, K.-H. Shin, and S.-B. Choe, IEEE Trans. Magn. **45**, 2485 (2009).

[127] H. Li, G. Yu, J. Teng, and F. Zhu, J. Phys. D: Appl. Phys. **39**, 4915 (2006).

[128] M. Kryder, K. Ahn, N. Mazzeo, S. Schwarzl, and S. Kane, IEEE Trans. Magn. **1**, 99 (1980).

[129] S.-B. Choe, Appl. Phys. Lett. **92**, 062506 (2008).

[130] K.-W. Moon, J.-C. Lee, S.-B. Choe, and K.-H. Shin, Curr. Appl. Phys. **9**, 1293 (2009).

[131] *Handbook of Chemistry and Physics*, http://www.hbcpnetbase.com/ .

[132] S. Hacia, T. Last, S. Fischer, and U. Kunze, J. Phys. D: Appl. Phys. **37**, 1310 (2004).

[133] A. Aharoni, J. of Appl. Phys. **83**, 6 (1998).

[134] S. Datta, *Electronic Transport in Mesoscopic Systems*, Cambridge University Press, 6th printing (2005) .

[135] R. Shankar, *Principles of Quantum Mechanics*, Kluwer Academics Plenum Publishers (New York), 2nd edition (1994).

[136] P. Solomon, IEEE Electr. Dev. Lett. **32**, 246 (2011).

[137] A. Cottet et al., Semicond. Sci. Technol. **21**, S78 (2006).

[138] D. Coon and K. Bandara, Appl. Phys. Lett. **55**, 2453 (1989).

[139] A. Cottet and M.-S. Choi, Phys. Rev. B **74**, 235316 (2006).

[140] Y. Utsumi, J. Martinek, G. Schön, H. Imamura, and S. Maekawa, Phys. Rev. B **71**, 245116 (2005).

[141] K. Ono, H. Shimada, and Y. Ootuka, J. Phys. Soc. Jap. **67**, 2852 (1998).

[142] A. Cottet, C. Feuillet-Palma, and T. Kontos, Phys. Rev. B **79**, 125422 (2009).

[143] A. van Staa, C. Johnas, U. Merkt, and G. Meier, Superlatt. and Microstr. **37**, 349 (2005).

[144] S. Krzyk, A. Schmidsfeld, M. Kläui, and U. Rüdiger, New Journ. Phys. **12**, 013001 (2010).

[145] C. Gould et al., Phys. Rev. Lett. **93**, 117203 (2004).

[146] J. Moser et al., Phys. Rev. Lett. **99**, 056601 (2007).

[147] S. van der Molen, N. Tombros, and B. van Wees, Phys. Rev. B **73**, 220406 (2006).

[148] F. Zwanenburg, D. van der Mast, H. Heersche, and L. Kouwenhoven, Nano Letters **9**, 2704 (2009).

[149] R. Engel-Herbert and T. Hesjedal, J. of Appl. Phys. **97**, 074504 (2005).

[150] J. Martinek et al., Phys. Rev. Lett. **91**, 127203 (2003).

[151] G. Burkard, J. Phys.: Condens. Mat. **19**, 233202 (2007).

[152] S. Kawabata, J. Phys. Soc. Jap. **70**, 1210 (2001).

[153] S. Parkin and D. Mauri, Phys. Rev. B **44**, 7131 (1991).

[154] X. Wang, S. Tabakman, and H. Dai, J. Am. Chem. Soc. **130**, 8152 (2008).

Additional Fabrication Information and Processing Recipies

A.1 Wafer properties

- highly p-doped Si wafer (boron doped)

- resistivity $10\mu\Omega$cm

- 400 nm SiO_2 layer

A.2 Wafer cleaning

- 1 hour sonication in acetone

- 30 minutes sonication in 2-propanol

- plasma cleaning in the reactive ion etching (RIE) system

    - pressure p $= 5{\cdot}10^{-5}$mTorr

    - gas O_2, flow rate 16 %

    - RF power P $= 200$ W

    - time t $= 30$ sec

- alternatively: 30 minutes UVO cleaning

A.3 Catalyst

- stock solutions sonicated for 12 h in bath-type sonicator

    - 30 mg Al_2O_3 in 20 ml 2-propanol

    - 93 mg $Fe(NO_3)_3 \cdot 9H_2O$ in 20 ml 2-propanol

    - 27 mg MoO_2Cl_2 in 20 ml 2-propanol

- 0.5 ml of each stock solution + 18.5 ml 2-propanol sonicated for 12 h

A.4 Chemical vapor deposition

- wafer cleaning (see above)

- catalyst sonication 1 hour in high-power sonicator (pulse duration: 0.5 s, pause: 0.5 s, power: 100 %)

- 1-2 droplets of catalyst on wafer, spinning 40 sec with 4000 rpm

- growth parameters

    - heating in Ar atmosphere (104 l/h)

    - growth for 10 minutes at T = 950 °C in CH_4 (44 l/h) and H_2 (8 l/h)

    - cool down to T = 530 °C in Ar + H_2

    - cool down to T = 330 °C in Ar

A.5 E-beam resist

- 100 nm resist layer: spinning of PMMA/MA 33 % (AR-P 617, Allresist). Parameters: speed = 4000 rpm, ramp = 4 s, time = 40 s

- baking on hot plate at 200° C for 3 minutes

- 200 nm resist layer: spinning of PMMA (AR-P 671.09 950K, Allresist, diluted in chlorobenzene). Parameters: speed = 4000 rpm, ramp = 4 s, time = 40 s

- baking on hot plate at 200° C for 3 minutes

A.6 E-beam lithography

- double layer resist (see above)

- parameters on Zeiss Supra 40

acceleration voltage	20 kV
fine working distance	9 mm
fine writefield	100 μm
fine aperture	10 μm
fine area dose	200 μAs/cm^2
fine area step size	0.0050 μm
fine line dose	1300 pAs/cm (2 times)
fine line step size	0.0050 μm
coarse working distance	16.9 mm
coarse writefield	2000 μm
coarse aperture	120 μm
coarse area dose	240 μAs/cm^2
coarse area step size	0.0622 μm

- developement in methyl isobutyl ketone (MIBK) dissolved in 2-propanol (1:3)

A.7 Ar plasma etching

- parameters are for etching in the Bestec evaporation system load lock

- plasma power 20 mA

- extraction voltage 0.6 kV

- anode voltage (ion energy) 1 kV

- anode current 0.15 mA

- chamber pressure $5 \cdot 10^{-5}$ mbar

- etching time $1 - 2$ min

Improving the Contact Properties of Permalloy - Additional Information

B.1 Polymer residues on the CNT contact area

Several devices showed that Permalloy can make good and reliable electrical contact to carbon nanotubes with room temperature device resistances between $20\,k\Omega$ and $50\,k\Omega$ (chapter 2, chapter 3). However, it was not possible in later devices to reproduce these results. The FM properties of the single Py strips were still very good, but contact resistances to CNTs were found to be very high ($> 100\,M\Omega$). By studying the Permalloy contacts we found residues close to the contacts and could show that polymer residues that cannot be resolved remain after development as presented in chapter 2. This is consistent with experimental findings of different research groups [93, 94, 95, 96].

In figure B.1 SEM images of Permalloy strips are shown. The strip in fig. B.1a has been structured with a $10\,\%$ higher exposure dose than used in general. Residues close to and on top of or below the contact are clearly visible. A residuing layer can also be seen when the exposure dose is lowered. In fig. B.1b the metalized structure is not continuous anymore because the used exposure dose was too low to expose the resist completely, but a continuous layer below is also visible there.

Systematic studies of the residues close to the contacts for different baking times, baking temperatures and additional treatments of the PMMA layer have been done. A summary of the experiments is given in the table B.1. The corresponding SEM images can be seen in in fig. B.2. Each strip has a
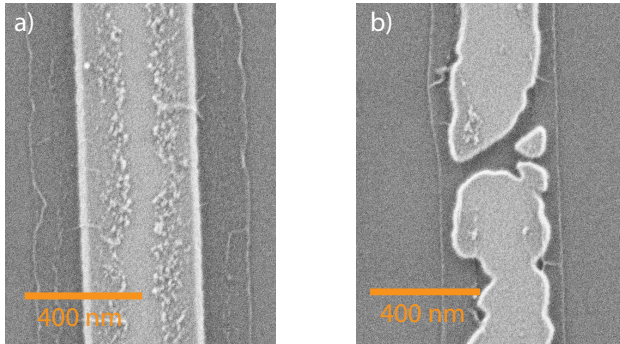
Figure B.1: SEM images of Permalloy strips structured with different dose factors in the lithography system. **a)** Strip written with a higher dose. Residues close to the contact and on top of the contact are visible. **b)** The dose to structure this strip was so low that it has only a desultory structure. A continuous residue layer can still be seen.

width of roughly 400 nm.

The strips shown in fig. B.2.01-03+06 have been fabricated using a PMMA /MA-PMMA double layer with varying baking time and temperature. It can be seen in the figures that neither the baking temperature nor the baking time can lead to Permalloy contacts without residues close to the contact.

	polymer	**T (°C)**	**t (min)**	**d (nm)**	**comment**
01	MA+PMMA	200/180	7/7	100/200	
02	MA+PMMA	180/180	1/3	100/200	
03	MA+PMMA	160/170	1/3	100/200	
04	PMMA	180	3	200	no MA layer
05	MA+PMMA	180/180	2/2	100/200	2'30" dev. time
06	MA+PMMA	90/90	10/10	100/200	
07	MA+PMMA	200/180	10/10	100/200	RIE after dev.
08	PMMA	180	2	200	30 kV
					dev. in IPA/H$_2$O
09	ZEP520A	180	3	300	dev. in
					MIBK/IPA 75"

Table B.1: Experiments with different baking times t, baking temperatures T and additional treatment of the polymer layers with thickness d have been done to remove the residues close to the Permalloy contacts. The corresponding SEM images can be seen in fig. B.2.
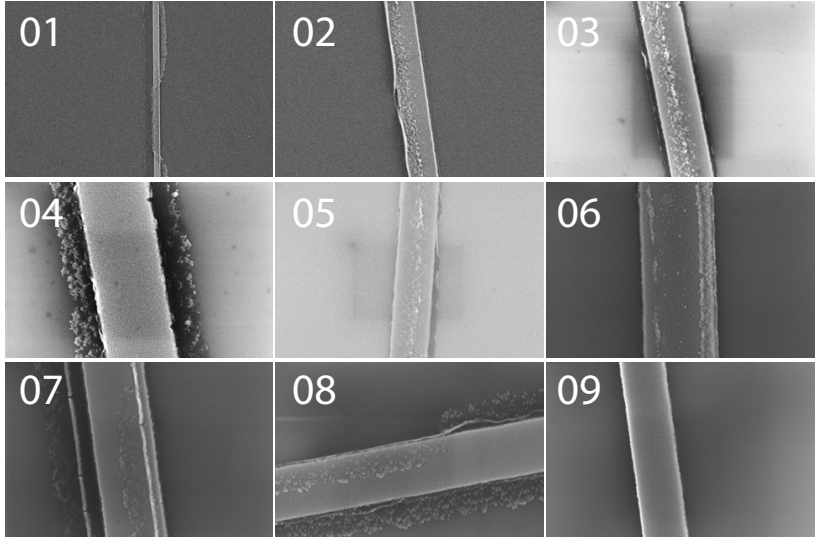
Figure B.2: Images of 400 nm wide Py strips produced with different resist baking times and temperatures (see table).

Fig. B.2.04 shows a strip fabricated only using PMMA as a resist. The surface of this strip looks cleaner but close to the strips much more resisues are visible. For the strip presented in fig. B.2.05 the development time after e-beam structuring was increased from 90 seconds to 150 seconds but residues are not removed by the longer development. For the contact in fig. B.2.07 we cleaned the developed area in a RIE process (30 sec., standard process). Residues are still left. The structure in fig. B.2.08 has been written with a high voltage of 30 kV and developed in IPA as proposed by [95] but also here the result is not very promising. Fig. B.2.09 shows a strip structured with ZEP520A resist[1]. Nearly no residues close to the contact can be seen. However, in device tests the lowest measured contact resistances to CNTs were found to be over $1\,M\Omega$ and for the most devices lie in the range of $50 - 100\,M\Omega$.

---

[1] composed of $11\,\%$ methyl styrene and chloromethyl acrylate copolymer (solid) and $89\,\%$ anisole (solvent) by ZEON CORPORATION

B.2 Aluminum oxide interlayer - preliminary results

Another approach to contact CNTs without a polymer interlayer can be to deposit a protection layer on the device that can be removed later. We evaporate a homogeneous 5 nm thick Al_2O_3 layer in an atomic layer deposition process. Then, the normal PMMA structuring process is done. Before the metal contacts are evaporated the Al_2O_3 layer on the contact area is removed in a 25 % *tetramethylammonium hydroxide* (TMAH) solution as introduced in chapter 2. The TMAH is not attacking PMMA and CNTs.

We also use aluminum oxide interlayers for graphene-based devices. Due to the hydrophobicity of graphene (and CNTs) atomic layer deposition is nontrivial [154]. Therefore, we tested to evaporate 5 nm of Al on the device in an evaporation system and let it oxidize in air. However, we found that the oxidation is not complete and unoxidized Al can lead to short circuits. Thinner layers are not homogeneous.

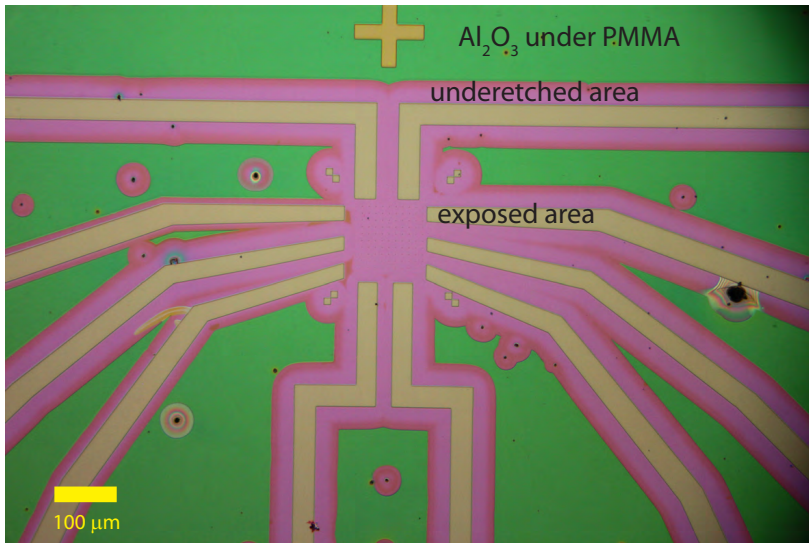For a device structured with a PMMA-MA/PMMA double layer we find

Figure B.3: Optical image of a device that has been structured and TMAH etched. The structures that have been developed and etched (yellow) are surrounded by a large underetched region (pink). Underetching to this exted leads to massive lift-off problems. These underetching effect can be avoided by using PMMA without the additional PMMA-MA layer below.

strong underetching effects going back to the PMMA-MA undercut. The width of the underetched areas is around 30 μm for the etching process described above. An optical image of the result is shown in fig. B.3. The yellow region is the structured mask, the pink area is the underetched region and the aluminum oxide under the PMMA looks green. We found that the metal lift-off gets problematic when the underetched region is to big. This is probably due to a lack of thermal coupling to the wafer of the freestanding PMMA parts. The underetching can be avoided by using only PMMA without the PMMA-MA layer below.

B.3 Electrical instabilities

A big problem of the most devices is the electrical instability during the measurements. Charge rearangements in the electrical device due to trapped charges in the SiO_2 layer, at the SiO_2/Si interface [97] or in water molecules bound to the nanotube [86] can lead to jumps or drifts in energy.

In figure B.4a the conductance of a single Couplomb peak of the device presented in chapter 4 as a function of backgate voltage is shown for sequence of 40 backgate voltage sweeps ($\sim 1\,\mathrm{min/sweep}$). The position of the peak is stable for several sweeps before it jumps to a different position. These gate jumps lead to a large change in conductance for a certain backgate voltage making it difficult to measure MR signals. Figure B.4b shows 300 backgate sweeps over two Coulomb peaks in a different device ($\sim 1\,\mathrm{min/sweep}$). Additionally to the gate jumps strong gate drifts are visible. A solution to this problem has not been found yet.
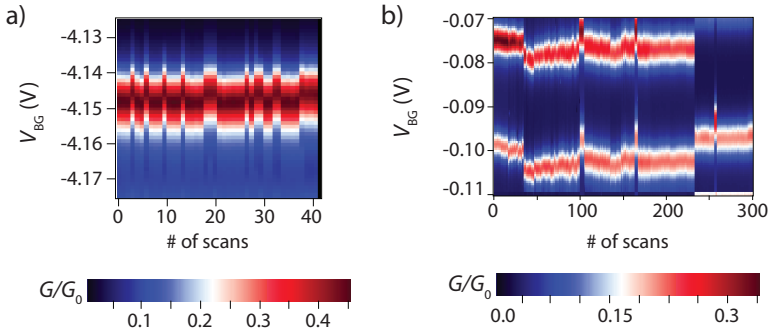

Figure B.4: Coulomb peak instabilities with time. **a)** 40 backgate voltage sweeps (~ 1 minute per sweep) have been performed to observe the position of a Coulomb peak with time. Jumps between two positions are observed. **b)** Stability of two peaks over 300 backgate voltage sweeps (~ 1 minute per sweep). The peaks are drifting with time and additionally the position changes between two (or more) different positions.

List of symbols and abbreviations

a_0	C-C bond length
$\boldsymbol{a}$	lattice vectors
$\boldsymbol{B}$	magnetic induction
C	Coulomb integral
$C_{\mathrm{S(D)}}$	source (drain) capacitance
$C_{\mathrm{G(BG)}}$	gate (backgate) capacitance
C_{Σ}	total capacitance
d	diameter
D	spin diffusion constant
δE	orbital energy
e	electron charge
E	energy
E_0	atomic energy
E_{A}	anisotropy energy (density)
E_{ex}	exchange energy
E_{F}	Fermi energy
E_{kin}	kinetic energy
E_{pot}	potential energy
$E^{\mathrm{S(T)}}$	singlet (triplet) configuration energy
E_{SW}	Stoner-Wohlfarth energy (density)
E_{Z}	Zeeman energy (per unit volume)
$f(E)$	Fermi function
g	g-factor
G	conductance, differential conductance
$G_{\mathrm{P(AP)}}$	parallel (antiparallel) conductance
h	height
$\boldsymbol{H}$	magnetic field
$\boldsymbol{H}_{\mathrm{d}}$	demagnetizing field
$\boldsymbol{H}_{\mathrm{C}}$	coercive field
$\boldsymbol{H}_{\mathrm{S}}$	switching field
$\boldsymbol{H}_{\mathrm{Sat}}$	saturation field

$\mathcal{H}_{\mathrm{atom}}$	central field Hamiltonian
$\mathcal{H}_{\mathrm{eff}}$	effective Hamiltonian
$\mathcal{H}'$	interaction Hamiltonian
$\boldsymbol{I}$	electrical current
J	exchange constant
$J_{i,j}$	exchange integral
$\boldsymbol{k}, \boldsymbol{\kappa}$	(electron) wave vector
K	anisotropy constant
l, L	length
m_{e}	electron mass
$\boldsymbol{M}$	magnetization
$\boldsymbol{M}_{\mathrm{R}}$	remanent magnetization
$\boldsymbol{M}_{\mathrm{S}}$	saturation magnetization
$\mathcal{M}$	tunnel matrix element
n	number of electrons
N	density of states
$\mathcal{N}$	demagnetization tensor
O	double overlap integral
P	polarization
$\boldsymbol{r}, \boldsymbol{R}$	spacial coordinate
R	resistance
$R_{\parallel(\perp)}$	longitudinal (perpendicular) resistance
$R_{\mathrm{P(AP)}}$	parallel (antiparallel) resistance
$\boldsymbol{s}, \boldsymbol{S}$	spin
U_{C}	charging energy
$\mathcal{U}$	Coulomb energy in mean field theory
v_{F}	Fermi velocity
V	voltage
$V_{\mathrm{G(BG)}}$	gate (backgate) voltage
V_{SD}	source-drain voltage
w	width
$\boldsymbol{W}$	wrapping vector
X	exchange integral

α	angle
$\Gamma_{S(D)}$	source (drain) contact coupling strength
ΔE_{ex}	exchange splitting
η	lever arm
λ	molecular field factor
λ_{sf}	spin relaxation length
μ	electrochemical potential
μ_B	Bohr magneton
μ_r	relative magnetic permeability
ϕ	spacial wave function
ψ	total wave function
θ	angle
σ	conductivity
τ_{sf}	spin relaxation time
χ	magnetic susceptibility
χ^P	Pauli susceptibiliy
$\chi^{S(T)}$	singlet (triplet) spin wave function
Ω	spin precession frequency
AMR	anisotropic magnetoresistance
CNT	carbon nanotube
CI	constant interaction
CVD	chemical vapor deposition
DOS	density of states
EDX	energy dispersive X-ray spectroscopy
FET	field effect transistor
FM	ferromagnet
GMR	giant magnetoresistance
NM	non-magnetic metal
MFT	mean field theory
MR	magnetoresistance
QD	quantum dot
SC	semiconductor
$SWCNT$	single wall carbon nanotube
$TAMR$	tunnelling anisotropic magnetoresistance
TMR	tunnelling magnetoresistance
VSM	vibrating sample magnetometer
XPS	X-ray photoelectron spectroscopy

Publication List

Publications

- *Permalloy-based carbon nanotube spin-valve*

  H. Aurich, A. Baumgartner, F. Freitag, A. Eichler, J. Trbovic and C. Schönenberger, APL **97**, 153116 (2010)

Oral presentations

- *Ferromagnetic contacts for carbon nanotube spintronic devices*

  QSIT seminar talk at the ETH Zürich (CH), March 2011

Poster contributions

- *Spin transport in graphene strongly coupled to ferromagnetic leads*

  J. Trbovic, H. Aurich, G. Gunnarsson, and C. Schönenberger, poster at the Frontiers in Nanoscale Science and Technology in Basel (CH), January 2008

- *Spin physics in SWCNT quantum dots with ferromagnetic and superconducting leads*

  G. Gunnarsson, A. Eichler, H. Aurich, M. Weiss, J. Trbovic, and C. Schönenberger, poster for the NCCR review panel in Basel (CH), April 2008

- *Spin physics in SWCNT quantum dots with ferromagnetic and superconducting leads*

  G. Gunnarsson, A. Eichler, H. Aurich, M. Weiss, J. Trbovic, and C. Schönenberger, poster for the Swiss Workshop on Basic Research in Nanoscience in Davos (CH), June 2008

- *Characterization of nanometer scaled Permalloy contacts for carbon-based spin-valve devices*

  H. Aurich, F. Freitag, A. Baumgartner, J. Trbovic, and C. Schönenberger, poster for the International Winterschool on Electronic Properties of Novel Materials (IWEPNM) in Kirchberg in Tirol (AT), March 2010

- *Characterization of nanometer scaled Permalloy contacts for carbon-based spin-valve devices*

  H. Aurich, F. Freitag, A. Baumgartner, J. Trbovic, and C. Schönenberger, poster for the NCCR review panel in Basel (CH), April 2010

- *Characterization of nanometer scaled Permalloy contacts for carbon-based spin-valve devices*

  H. Aurich, F. Freitag, A. Baumgartner, J. Trbovic, and C. Schönenberger, poster for the SPS annual meeting in Basel (CH), June 2010

- *Permalloy-based carbon nanotube spin-valve*

  H. Aurich, A. Baumgartner, F. Freitag, J. Trbovic, and C. Schönenberger, poster for the Topological Meeting on Spins in Organic Semiconductors SPINOS III in Amsterdam (NL), August 2010

- *Quantum transport in carbon nanotube and nanowire hybrid devices*

  H. Aurich, A. Baumgartner, L. Hofstetter, S. D'Hollosy, S. Nau, J. Samm, J. Schindele, M. Weiss, and C. Schönenberger, poster for the First General Meeting of the NCCR-QSIT in Arosa (CH), January 2011

- *Permalloy-based carbon nanotube spin-valve*

  H. Aurich, A. Baumgartner, F. Freitag, J. Trbovic, and C. Schönenberger, poster for the Quantum Mesoscopic Conference Les Rencontres de Moriond in La Thuile (IT), March 2011

Curriculum Vitae

Hagen Matthias Aurich
Born May 29th 1982 in Stuttgart (D)

Education

- October 2007 - October 2011
  PhD in experimental physics at the University of Basel
  Supervision: Prof. Dr. C. Schönenberger
  "Carbon nanotube spin-valve with optimized ferromagnetic contacts"

- October 2005 - October 2007
  Master of Science in Physics at the University of Basel
  Supervision: Prof. Dr. C. Schönenberger
  "Fabrication and electrical characterization of graphene"

- October 2002 - October 2005
  Bachelor of Science in Physics at the University of Basel

- 1992 - 2001
  Kant Gymnasium Weil am Rhein (D)
  Abitur
  Latinum

Professional positions

- 2007 - 2011
  Research assistant at the University of Basel
  Group Prof. Dr. C. Schönenberger

- 2007 - 2011
  Teaching assistant for Physics 1 and 2 exercises at the University of Basel

- 2004 - 2007
  Research assistant at the Fraunhofer Institute for High-Speed Dynamics in Efringen-Kirchen (D)

Lecures

For valuable lectures during my studies I am indebted to:
B. Binggeli, C. Bruder, G. Burkard, H. Burkhart, R. Buser, M. Calame, S. Goedecker, M. Grote, H. J. Güntherodt, M. Hegner, K. Hencken, H. J. Hug, H.-C. Im Hof, B. Krusche, D. Loss, D. Masser, E. Meier, T. Rauscher, C. Schönenberger, I. Sick, F.-K. Thielemann, D. Trautmann, T. Vetter

Acknowledgements

Now the time has come to thank those people I was lucky to work with in the last four years:

Firstly, I would like to thank Christian Schönenberger for giving me the opportunity to do a PhD in his research group. I appreciate his enthusiasm for nanoscale science and his huge knowledge and experience in the field of mesoscopic physics he offers the PhD students. I also appreciate his ability to form and lead a homogeneous research group with a pleasant work environment and to organize great scientific and non-scientific workshops and excursions.

Secondly, I would like to thank Andreas Baumgartner. Andreas is an exceptional scientist and I was lucky to be mentored by him while working on my PhD. He is always passionate about new experiments and it seems like there is no question he cannot answer. I have learned a lot from him. His ability to motivate people and his always-present sense of humor were really encouraging, especially when experiments were not working as expected.

I also would like to take the opportunity to thank Brian Hickey for reading my thesis and refereeing my defense.

I am grateful for all the good colleagues in my team: Thanks to Frank Freitag who worked with me on the ferromagnetic contacts. Thank you to the rest of the carbon nanotube team, Jens Schindele and Julia Samm and also to the rest of our office 1.25: Matthias Bräuninger, Lukas Hofstetter, Samuel D'Hollosy and Stefan Nau. I have always enjoyed the atmosphere in our office. Furthermore, I want to thank Laurent Marot for his help regarding the XPS and EDX measurements.

During my PhD I worked with a lot of great scientists and I made many friends from all over the world. Thank you to all current and former group workers: Jon Agustsson, Claire Barrett, Jan Brunner, Michel Calame, Szabolcs Csonka, Alex Eichler, Toni Fröhlich, Wangyang Fu, Teresa Gonzalez, Gunnar Gunnarsson, Haichao Huang, Roman Huber, Dino Keller, Andreas Kleine, Oren Knopfmacher, Jianhui Liao, Sense Jan van der Molen, Cornelia